ISAR IMAGING AND MOTION COMPENSATION

A THESIS SUBMITTED TO
THE GRADUATE SCHOOL OF NATURAL AND APPLIED SCIENCES
OF
MIDDLE EAST TECHNICAL UNIVERSITY

BY

TALİP KÜÇÜKKILIÇ

IN PARTIAL FULFILLMENT OF THE REQUIREMENTS
FOR
THE DEGREE OF MASTER OF SCIENCE
IN
ELECTRICAL AND ELECTRONICS ENGINEERING

DECEMBER 2006

Approval of the Graduate School of Natural and Applied Sciences

Prof. Dr. Canan ÖZGEN
Director

I certify that this thesis satisfies all the requirements as a thesis for the degree of Master of Science.

Prof. Dr. İsmet ERKMEN
Head of Department

This is to certify that we have read this thesis and that in our opinion it is fully adequate, in scope and quality, as a thesis for the degree of Master of Science.

Prof. Dr. Gülbin DURAL
Supervisor

Examining Committee Members

Prof. Dr. Gönül T. SAYAN	(METU,EE)	
Prof. Dr. Gülbin DURAL	(METU,EE)	
Prof. Dr. Kemal LEBLEBİCİOĞLU	(METU,EE)	
Assoc. Prof. Dr. Sencer KOÇ	(METU,EE)	
Caner TEZEL (M.Sc.)	(ASELSAN)	

I hereby declare that all information in this document has been obtained and presented in accordance with academic rules and ethical conduct. I also declare that, as required by these rules and conduct, I have fully cited and referenced all material and results that are not original to this work.

Name, Last Name : Talip KÜÇÜKKILIÇ

Signature :

ABSTRACT

ISAR IMAGING AND MOTION COMPENSATION

Küçükkılıç, Talip

M.S., Department of Electrical and Electronics Engineering

Supervisor: Prof. Dr. Gülbin Dural

December 2006, 167 pages

In Inverse Synthetic Aperture Radar (ISAR) systems the motion of the target can be classified in two main categories: Translational Motion and Rotational Motion. A small degree of rotational motion is required in order to generate the synthetic aperture of the ISAR systems. On the other hand, the remaining part of the target's motion, that is any degree of translational motion and the large degree of rotational motion, degrades ISAR image quality. Motion compensation techniques focus on eliminating the effect of the targets' motion on the ISAR images.

In this thesis, ISAR image generation is discussed using both Conventional Fourier Based and Time-Frequency Based techniques. Standard translational motion compensation steps, Range and Doppler Tracking, are examined. Cross-correlation method and Dominant Scatterer Algorithm are employed for Range and Doppler tracking purposes, respectively. Finally, Time-Frequency based motion compensation is studied and compared with the conventional techniques.

All of the motion compensation steps are examined using the simulated data. Stepped frequency waveforms are used in order to generate the required data of the simulations. Not only successful results, but also worst case examinations and lack of algorithms are also discussed with the examples.

Keywords: Inverse Synthetic Aperture Radar, ISAR Image Generation, Motion Compensation, Range and Doppler Tracking, Time-Frequency Based Motion Compensation.

ÖZ

ISAR GÖRÜNTÜLEME VE HIZ ETKİSİNİN YOK EDİLMESİ

Küçükkılıç, Talip

Yüksek Lisans, Elektrik Elektronik Mühendisliği Bölümü

Tez Yöneticisi: Prof. Dr. Gülbin Dural

Aralık 2006, 167 sayfa

Ters Yapay Ağız Açıklıklı Radar (ISAR) görüntüleme sistemleri göz önünde bulundurulduğunda, hedeflerin sergilemiş oldukları hareketler Öteleme Hareketi ve Dönüş Hareketi şeklinde iki ana sınıf altında toplanabilmektedirler. Az miktarda bir dönüş hareketi, ISAR sistemlerindeki yapay ağız açıklığının elde edilebilmesi bakımından gereklidir. Öte yandan, bütün öteleme hareketleri ve büyük miktarlarda gerçekleşen dönüş hareketleri ISAR görüntülerindeki kaliteyi olumsuz yönde etkilemektedir. Hareket telafisi teknikleri, hedefin hareketinden kaynaklanan ISAR görüntüsü bozulmalarını ortadan kaldırmayı amaçlamaktadırlar.

Bu tezde ilk olarak, hem alışılagelmiş Fourier tabanlı, hem de Zaman-Frekans tabanlı teknikler kullanılarak ISAR görüntülerinin ne şekilde elde edileceği ile ilgili olarak yapılan çalışmalara yer verilmiştir. Öteleme hareketinin ISAR görüntüleri üzerindeki etkilerinin yok edilmesi ile ilgili olarak ortaya koyulan standart adımlar, Menzil İzleme ve Doppler İzleme, irdelenmiştir. Menzil İzleme amacına yönelik olarak

Çapraz-İlinti metodu kullanılarak bir takım çalışmalar yapılmıştır. Doppler İzleme amacına yönelik olarak da Baskın Yansıtıcı Mantık Düzeni (Algoritması) ele alınarak bazı çalışmalar yapılmıştır. Son olarak da Zaman-Frekans tabanlı olarak hareket etkisinin yok edilmesine yönelik olarak ortaya konulan yöntem ile ilgili bazı çalışmalar yapılmış ve elde edilen sonuçlar alışılagelmiş hareket telafisi yöntemlerin sonuçları ile kıyaslanmıştır.

Hareket etkisinin yok edilmesi ile ilgili adımlar, oluşturulan benzeşim verilerilerine uygulanarak irdelenmiştir. Kullanılan benzeşim verilerinin üretilmesinde frekans-adımlı dalga tipleri kullanılmıştır. Hareket etkisinin yok edilmesi anlamında sadece başarılı sonuçlara değil, aynı zamanda kötü durum incelemelerini ve seçilen yöntemlerin eksikliklerini, zayıflıklarını vurgulayan örneklere de yer verilmiştir.

Anahtar Kelimeler: Ters Yapay Ağız Açıklıklı Radar, ISAR ile Görüntü Oluşturma, Hareket Etkisinin Yok Edilmesi, Menzil ve Doppler İzleme, Zaman-Frekans Tabanlı Yöntemle Hareket Etkisinin Yok Edilmesi.

This thesis is dedicated to

my Parents, Alime and Recep

and

the memory of my uncle,

Şehit Hv. Plt. Üt̆m. Nusret Küskü

ACKNOWLEDGMENTS

I would like to thank to,

Prof. Dr. Gülbin Dural, my supervisor, for her steady support, encouragements and guidance along my education. Without her guidance and support, this thesis would not be possible,

Dr. Anthony Zyweck, for his interest and for his excellent PhD Thesis, and **Dr. Brett Haywood**, for his inspirational response to my e-mail,

Dr. Victor C. Chen, for his important simulation data about the work. I also wish to express my gratitude to his guidance about the time-frequency based motion compensation concept,

Assoc. Prof. Dr. Tolga Çiloğlu, Assoc. Prof. Dr. Yakup Özkazanç and Asst. Prof. Dr. Müjdat Çetin, for their valuable criticisms and advices,

Demet Uluşen, my dear friend, not only for the papers and books, but also for her encouragements,

My parents, for their unlimited patience and for their constant supports,

Hare Küçükkılıç, my sister, for her support in the preparation of this page,

Caner Tezel, my dear friend, for his valuable ideas, criticisms, encouragements and for serving on my committee.

TABLE OF CONTENTS

LIST OF TABLES

LIST OF FIGURES

CHAPTER 1

INTRODUCTION

1.1 ISAR and ISAR Target Imaging Concept Overview

Synthetic Aperture Systems

ISAR (Inverse Synthetic Aperture Radar) Imaging Systems are employed to construct the two dimensional images of the targets such as ships on the sea surface or planes on the air, by way of using Radio Frequency signals, especially between the wavelengths of one to thirty centimeters.

The reason of using RF signals for imaging purpose is the atmospheric absorption of significant fraction of the radiation, at visible and infrared wavelengths, which are used for optical and thermal imaging. In some cases, optical sight could not be possible even in the clear environment. That is to say, the born of the idea of using RF signals for imaging is almost an obligation.

Radar Systems provide their own source of illumination by transmission of electromagnetic energy. The atmospheric absorption of transmitted energy is minimal at wavelengths of one to thirty centimeters. Thus, radar imaging systems can essentially provide an all-weather operation [1].

Synthetic Aperture Radar (SAR) Imaging systems are airborne systems and provide the images of the objects on the ground or the images of the ground itself, while ISAR systems are generally space borne systems and they are used for imaging of

moving targets. However, there are some airborne ISAR systems which are used for imaging of moving targets such as ships on the sea surfaces.

The ISAR systems are the dual of the SAR systems if the similarities between the principles of the operations are taken into consideration, while ISAR systems are the ***Inverse*** of the SAR systems according to the imaged objects and the location of the radar equipments.

ISAR Imaging

ISAR imaging systems are used to project the **electromagnetic reflectivity properties** of the targets' reflective components such as wings, tail, nose, fuselage, engine and the weapons, on to a two **dimensional** plane. Two topics have to be emphasized at this point:

- the dimensions of the ISAR image,
- the conversion of the targets electromagnetic reflectivity properties on to planar points.

The first image dimension becomes ***Slant Range*** (terms ***Range*** or ***Down-Range*** are sometimes used interchangeably) to be question of imaging with ISAR systems. Range axis is the straight line which connects the target with the radar. In other words, ***Range*** refers to range measured along the radar line of sight (LOS). Equidistance range lines are fall over spherical curves. But if the distances between the radar and the targets (typically tens of kilometers) are considered, these spherical curves could be thought as parallel straight lines as a good approximation (Figure 1.1).

As is well known, the clarity of a two dimensional image depends on the resolution obtained in each dimension. **Range Resolution** could be controlled by the transmitted signals properties (signal type, repetition frequency, processing methods) and it could vary between the tens of meters and a few centimeters. Hence, targets reflective points such as nose, tail and left-right wings as well could be able to map

into different **Range Cells** (term ***Range Bin*** is sometimes used interchangeably), as shown in Figure 1.1.

The second image dimension is the ***Cross-Range***. Cross-Range axis and equidistance Cross-Range lines lie perpendicular to the Range axis. Certainly, there could be infinite number of perpendicular axes to the Range axis. But which of them will serve as the second dimension of the ISAR image? The answer of this question hides oneself in the motion of the targets own: The Cross-Range axis is also perpendicular to the axis of the targets rotational motion. So, the Cross-Range axis is perpendicular to both of the range axis and the targets rotational motion axis.

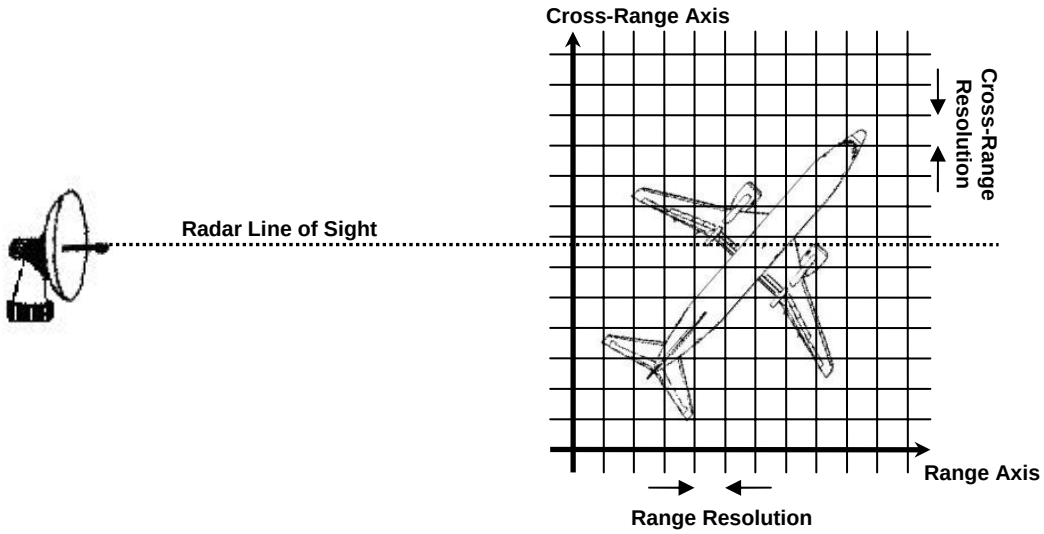

Figure 1.1 Target image dimensions

As it could be understood from the previous paragraph, in order to resolve the target points on the Cross-Range axis, the target has to put a relative rotational motion (aspect rotation) with respect to the radar. This rotation's axis has to have at least significant amount of perpendicular component to the range axis. Because during this rotation, target's reflective points would rotate with relatively different velocities to the radar and they reradiate the radar signal with different **Doppler Shifts**. Thus, this

different Doppler Shifts could be evaluated with some kind of signal processing methods and virtual Cross-Range dimension could be obtained ***Synthetically***.

Synthetically generation of the Cross-Range resolution requires *Coherent Processing* of radar signals in specific time duration. This required time is called ***Coherent Integration Time***, ***Image Frame Time*** or ***Dwell Time*** [4,11].

Because of the direct relation between the Cross-Range dimension and the Doppler information, the term *Range-Doppler Imaging* is also called instead of the term ISAR Imaging in some sources [2,3].

1.2 A short comparison of Real Aperture Radar and Synthetic Aperture Radar

Imaging with RF signals is not originated with the ***Synthetic Aperture*** applications like SAR and ISAR. ***Real Aperture*** *Imaging Radar*s (***Real Array*** Imaging Radars, as in the former usage of the term [1]) were being used especially for geographical imaging applications, before the invention of the Synthetic Aperture Imaging methods.

Commons

Imaging radars, both real and synthetic aperture, obtain the range resolution by the same principle; controlling the transmitted pulses properties.

Differences

The main and principal difference between the Real and Synthetic Aperture Radars is the construction method of the Cross-Range Resolution. Real array radars obtain the cross-range resolution by the antenna beamwidth, which is a fact of the physical properties of the antennas (Figure 1.2).

Since the antenna beamwidth in each direction is inversely proportional to its length in that direction, the cross-range resolution of real aperture imaging radars is

obtained through the use of long antennas (narrow beamwidth). As a natural result, the desire to use regular size airborne antennas for ground mapping has led to the invention of SAR.

Since the resolution in Cross-Range is related to the radar-target range for Real Aperture Radar, points closer to the radar become resolvable while points farther away are not.

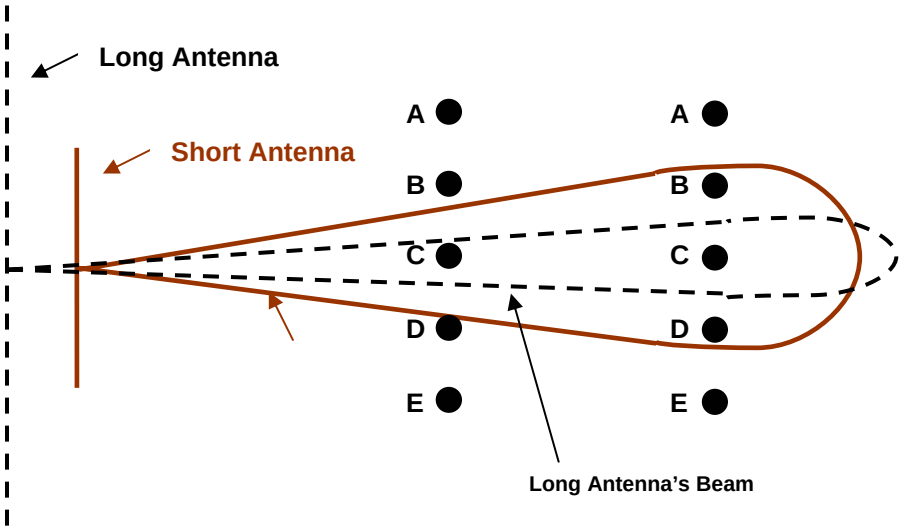

Figure 1.2 Effect of the antenna length on the cross-range resolution

At this point it has to be stated that, this kind of real array imaging radars can only be used as the terrestrial imaging purposes, since it is impossible to find such kind of flying objects which has such kind of big and separate points on its body.

The reduction of antenna size in going from real to synthetic aperture radars has been replaced by the increased amount of Doppler signal processing required for Cross-Range Resolution [1].

1.3 Brief History of SAR Researches

The development of synthetic aperture radar originated in 1951 with Carl Wiley, who postulated the use of Doppler or frequency information in obtaining Cross-Range resolution. Based on this idea and succeeding developments, the first SAR image was produced by researchers at the University of Michigan in 1958 using an optical processing method [2].

Precision optical processors and hologram radars were developed and fine resolution strip maps obtained by the mid 1960's. In the early 1970's, SAR imagery using digital signal processing methods were obtained off-line and non-real time [2].

In the beginning of the 1980's, fundamentals of the ISAR imaging and the effect of the targets motions' on the ISAR-SAR images were well represented and some of the techniques were suggested for the ***motion compensation***.

In the 1990's, all of these previous researches were followed by much more complex analysis of the radar signals, motion compensation methods, target identification and classification processes and development of different imaging methods such as Joint Time-Frequency Transformation.

ISAR systems and imaging techniques, with its own problematics such as motion compensation, are widely researched by the laboratories, institutes and universities which are the owners of high-technologies. ISAR related subjects are dealt with in the scope of research and development activities with all of its aspects.

1.4 A Few Introductive Words About Motion and Motion Compensation

As it is mentioned in the previous subsections, *Synthetic Aperture* could be developed if and only if the target exhibits a rotational motion (aspect rotation) with respect to the radar. Moreover, generation of the ISAR images need some data collection time, which is called Coherent Integration Time.

Although the targets rotation is an obligation of the image generation, in many cases, targets rotational and translational motion affects the quality of the ISAR image and problems such as blurring or smearing are to come out because of the relatively long coherent processing intervals.

If the fast maneuvering targets are taken into consideration, effect of the motion becomes much more important and imaging becomes impossible without compensation of the effects of these motions.

The maneuvers of targets could be gathered into two main titles as,

- Translational Motion – is the motion along the Range axis, which is also called Radar Line of Sight (RLOS),
- Rotational Motion – is the motion, causes aspect change of the target from the view of the radar.

Scope of the ***Motion Compensation***, is the elimination of the effects of these two kinds of motions. There are several kind of Motion Compensation methods, which were proposed from the beginning of the 1980's. Some of them are examined in the scope of this thesis.

1.5 Thesis Overview and Organization

In this thesis, ISAR Imaging systems and Motion Compensation Concept is introduced. In order to do that, some preliminary features of transmitted and received high resolution waveforms and generation of range profiles are investigated first of all. Conventional and Time-Frequency based ISAR imaging systems are discussed and explained. Then, Motion Compensation stages are examined in details.

Chapter 2 gives brief information about the basic concepts of ISAR Imaging systems. High resolution radar concept, in both slant-range and cross-range, is introduced. Then, high resolution radar waveforms are described. Section 2.4 describes the

processing method of received signals. Range Profile concept, which is the basic concept of the ISAR Image generation, is also included and explained in this chapter.

Chapter 3 introduces classical method of ISAR image generation; Range-Doppler Imaging. Section 3.3 describes image generation method step-by-step. But before that, in section 3.2, image dimensions; range and cross-range are examined by the way of detailed resolution analysis and examples. Motion compensation is not the topic of this chapter, but some of the examples are illustrated, in order to show the effect of the motion on the ISAR images.

Chapter 4 introduces an alternative way of ISAR Image generation: Time-Frequency Analysis Method. In order to do that, one of the simplest method of Joint Time-Frequency Transformations, Short Time Fourier Transformation is introduced in details. Then, Time-Frequency-based ISAR Image generation method is discussed and Time-Range-Doppler cube concept is introduced. A short comparison of Conventional Imaging (Fourier-based Range-Doppler Imaging) and Time-Frequency Based ISAR imaging also included. At the end of this chapter, four simulation example is given about the Time-Frequency-based ISAR image generation.

Chapter 5 introduces Motion Compensation concept. Effect of the target's motion and need of the motion compensation are explained in Chapter 5.2 with some mathematical derivations. Chapter 5.3 describes translational motion compensation concept in details. After this explanation, Chapter 5.4 gives detailed description of the first step of motion compensation; Range Tracking. Method is introduced with detailed mathematical derivations. Chapter 5.5 introduces Doppler Tracking; the second step of the standard motion compensation. At last, detailed simulation examples and results are presented at the end of the chapter.

Chapter 6 introduces application of the Time-Frequency Transformations in the motion compensation. Chapter 6.2 explains mathematical background of the application. Chapter 6.3 gives some examples of this method.

Finally, Chapter 7 summarizes the important results of the thesis and also outlines the suggested future researches.

CHAPTER 2

BASIC CONCEPTS of ISAR IMAGING

2.1 Introduction

In this chapter, some of the basic concepts associated with high resolution radar is introduced. These basic concepts provide a background for the further materials and simulations, presented in following chapters of this thesis.

2.2 Introduction to High Resolution Radar

In order to achieve the complete understanding of the term *High Resolution*, some of the questions are going to be examined.

What makes the Resolution to become High?

High resolution is a generic term which is not linked to any particular absolute resolution [6]. High resolution is typically used to denote the ability to resolve *individual scattering centers* on a single target, beyond the ability to resolve the separate targets. Thus, not only the target detection but also the target identification, classification and some other imaging applications are becoming possible by the use of High Resolution Radars.

How do we obtain High Resolution?

High resolution is possible for both of the slant-range and the cross-range dimensions and implies the use of *large bandwidth* (*wideband*) radar signals for high slant-range resolution and use of very narrow beam antenna (RAR case) or *synthetic aperture processing* (SAR case) for high cross-range resolution.

2.2.1 High Resolution in Slant-Range

Resolution in the range domain corresponds to the resolution in the time (range-delay) domain [4]. High resolution in time could be achieved with large bandwidth radar signal waveforms. Slant range resolution Δr_s is related to the radar waveform bandwidth by

$$\Delta r_s \approx \frac{c}{2\beta} \tag{2.1}$$

where c is the speed of propagation and β is the bandwidth of the waveform. Further information and examination about this fundamental relationship is available in [5].

Some common types of radar waveforms, to achieve High Range Resolution (HRR) are:

- Short-Pulse Waveforms,
- Pulse-Compression (Chirp) Waveforms
- Stepped Frequency Waveforms

The bandwidth of a radar waveform is real in the case of a pulse-compression or a short-pulse waveforms and it is synthesized from a number of discrete frequencies in the case of a stepped frequency waveform.

Certainly, there are many other waveforms and methods that could be used to achieve a high bandwidth [4] but only these three common types of waveforms are briefly described in the following subsections.

2.2.2 High Resolution in Cross-Range

Real Aperture Radar Case

As it was introduced in the Chapter 1, cross-range resolution depends upon the beamwidth of the antenna being used, in the case of Real Aperture Radar.

In order to put a convenient criterion for the cross-range resolution, it could be helpful to examine the 3 dB beamwidth, which is directly proportional to the cross-range resolution and determined by,

$$\phi_{3dB} \approx \frac{\lambda}{d} \tag{2.2}$$

where λ is the wavelength and d is the antenna size. It can be seen from the Equation (2.2) that there are two ways to increase the cross-range resolution:

1. Reducing the wavelength being used,
2. Increasing the size of the antenna aperture.

But there are some upper bounds (limitations) on both of these two alternatives, because of the atmospheric propagation losses (and the radar system size and cost) on the wavelength and the physical limitations on the antenna aperture size.

(Inverse) Synthetic Aperture Radar Case

Although the formulations and detailed examinations about the cross-range resolution concept of synthetic aperture processing are left to the following sections, some basic logical ideas and approaches related to the cross-range resolution will be putting forward at this stage.

The basic idea of the synthetic aperture, as it was introduced in Chapter 1, comes from the relative motion of the target with respect to the radar. This relative rotational motion (aspect change) exposes the different Doppler shifts of the scatterer points on the target, during the Coherent Integration Time (observation duration of the target required for the image generation), which is the source of the cross-range resolution. So, it could be stated that the degree of the cross-range resolution depends to the;

1. Coherent integration time and
2. The degree of the rotational motion.

The latter factor is only depending to the targets motion and it could not be controlled by the imaging system, since the ISAR processing is a *blind process*. This is also the main reason of the unavailability of ISAR image construction at some cases, in which the target does not exhibit a relative rotational motion relative to the radar. If this factor is put aside, only the Coherent Integration Time could be controlled, and increased, in order to achieve a better cross-range resolution. On the other hand, as a trade off, this kind of increment in Coherent Integration Time would also results with some corruption (blurring, smearing) in the image especially in the case of fast maneuvering targets. So the Coherent Integration Time appears as one of the basic design criteria for the ISAR systems. More of the words about the cross-range resolution are kept for the following sections.

2.3 High Resolution Radar Waveforms

2.3.1 Short Pulse Waveforms

High resolution in the time domain corresponds directly to high resolution in slant-range. A resolution of Δt in the time domain corresponds to a slant-range resolution of $\Delta r_S = \frac{c\Delta t}{2}$ where the factor of two appears because of the travel of energy to and

from the target (round-trip time). Decreasing the pulse width was the first approach which was used by radar designers to increase range resolution. This approach worked to an extent but as the pulse width was decreased certain practical problems which limited the usefulness of the technique were encountered. The two main problems with very short pulse widths are:

High sampling rates

A very short pulse width or more correctly the corresponding high bandwidth means that a very high Analog to Digital Converter (ADC) sampling rate is required. A 1 μs pulse means that a minimum sampling rate of 2 MHz is required to satisfy the Nyquist criterion. It is difficult and costly to simultaneously achieve a high sampling rate and a large number of digitized bits in an ADC [6].

Low average power

A very short duration pulse has a very small average power. A large average power is desired since it is this waveform characteristic that determines the detectable range of a target [7]. The ratio of peak power to average power is very large for a short pulse waveform. A high peak power requirement imposes high stresses on the radar system components and it makes a short pulse system very expensive to build.

To achieve a high slant-range resolution without using short pulses, it is necessary to spread the radar waveform energy over time whilst still maintaining a high bandwidth. Two different techniques which achieve this are discussed in the following subsections [6].

2.3.2 Pulse-Compression Waveforms

A block diagram of a pulse-compression system is shown in Figure 2.1. The key to a pulse-compression system is the transmission of an expanded (the waveform energy is spread over time) high bandwidth waveform. On reception, this waveform is compressed to give a high resolution in time [6].

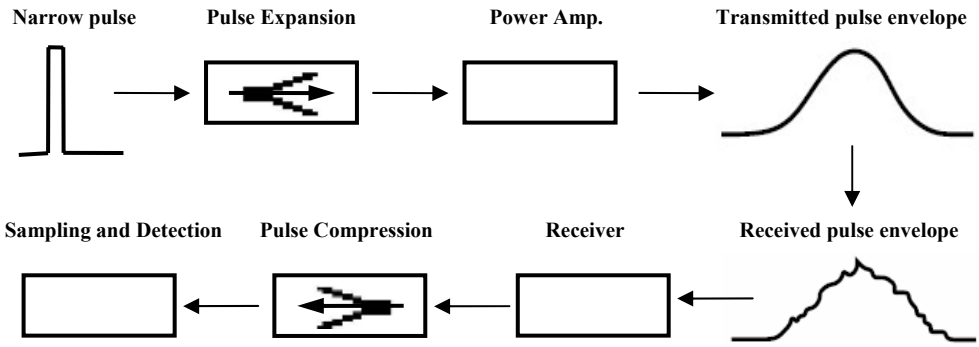

Figure 2.1 An illustration of pulse compression

The expansion of a narrow pulse is not necessary if a suitable expanded waveform is produced by another means. The ***chirp*** waveform shown in Figure 2.2 [4], is an example of such an expanded waveform. For HRR applications, only the chirp (analog frequency coding) has been used to any significant extent. The more general term, pulse-compression radar, is therefore often used to refer to the chirp-pulse type of pulse compression.

Chirp-pulse compression is produced by linearly increasing the frequency of an oscillator. With fast inexpensive digital synthesizers now available this is becoming a common and economical way to produce a high bandwidth waveform. The increasing use of digital components is bringing down the cost of radar systems and it is also increasing radar system flexibility.

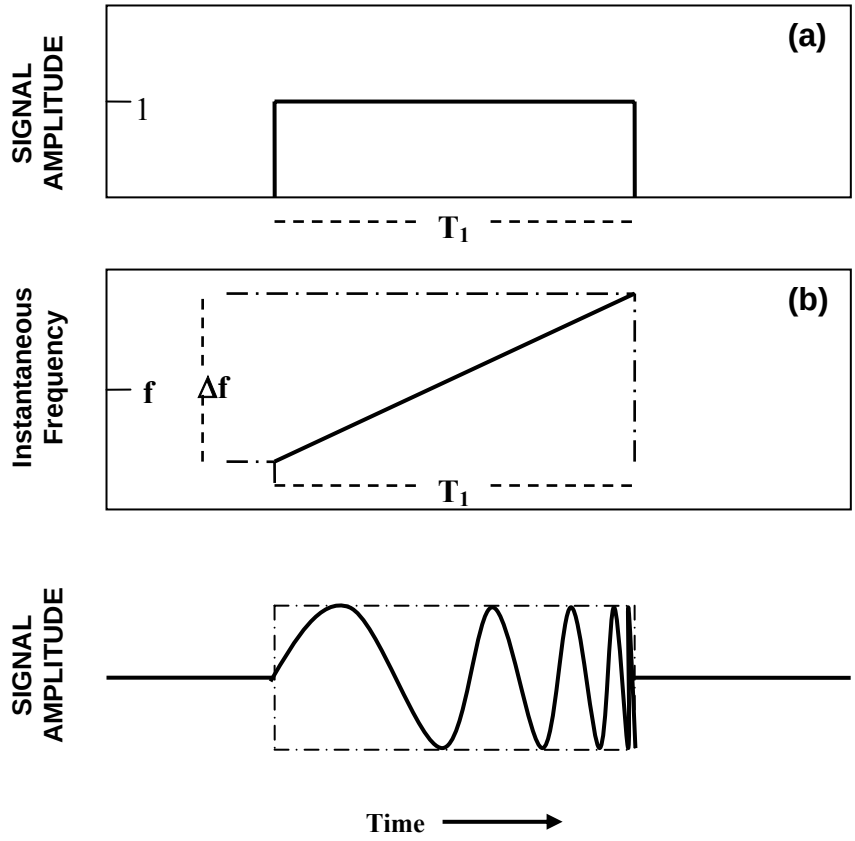

Figure 2.2 Chirp radar transmitted waveform: (a) transmitter pulse envelope; (b) transmitted pulse frequency versus pulse duration; (c) transmitted pulse RF waveform

2.3.3 Stepped Frequency Waveforms

All of the simulations are based on the stepped frequency type of radar signals in this thesis. Stepped frequency concept is going to be examined with all possible aspects throughout this report, as well as possible.

Instead of collecting the target scattering information in the time domain, a stepped frequency waveform collects the information in the frequency domain. Once the information has been collected in the frequency domain it is transformed into an equivalent representation in the time domain. This transformation is normally achieved using the inverse discrete Fourier transform (IDFT). This process is going

to be examined in the following sections. Only the main characteristics are going to be summarized in this section.

Figure 2.3 illustrates a stepped frequency waveform. A burst (or sweep) of n pulses is transmitted, where the frequency of each pulse differs from the previous pulse by Δf. The *effective* bandwidth of the burst is $\beta = n\,\Delta f$. As it was explained in the previous sections, the bandwidth is called effective because it is synthesized from a number of discrete frequencies [4].

The time between pulses, Pulse Repetition Interval (PRI), is T_{PRI} and each pulse has a length of T_P.

In an imaging scenario, which will be discussed later, the radar transmits N bursts to achieve an appropriate synthetic aperture for cross-range processing.

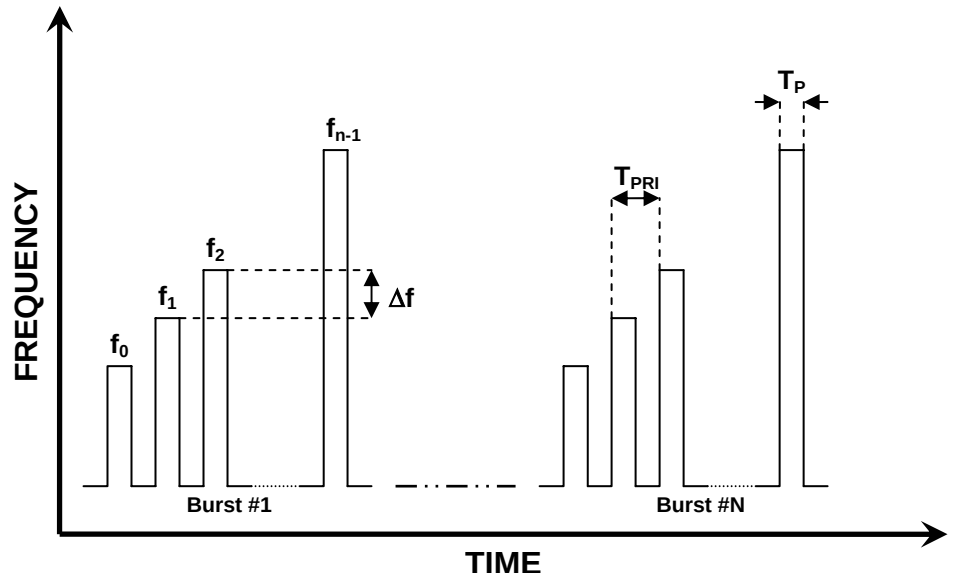

Figure 2.3 The stepped frequency waveform

Using a stepped frequency waveform to achieve a high resolution in range requires a careful choice of the radar waveform parameters. The parameters to be decided upon and the significance of each are listed in Table 2.1.

Table 2.1 The parameters of a stepped frequency waveform

Waveform Parameter	***Meaning and Significance***
Δf	The frequency increment between successive pulses in a Burst.
n	The number of discrete pulses per burst.
N	The number of sweeps coherently processed to form an ISAR image.
β	The effective bandwidth of a burst $\beta = n\,\Delta f$, determines the slant-range resolution according to Equation (2.1).
T_P	The pulse width. This must be large enough to envelop the entire target.
T_{PRI}	The pulse repetition interval (PRI). This must be large enough to prevent Doppler ambiguities and also be small enough to prevent range ambiguities.

2.3.4 Pulse-Compression Versus Stepped Frequency

Operational radars normally employ pulse-compression waveforms. Stepped frequency waveforms are used by research radars and RCS instrumentation radars. The major limitation of a stepped frequency waveform is that it takes too long to collect the data from the target. This limitation is a consequence of having to transmit n pulses to get a single High Resolution Range Profile. For a radar that is required to operate with a high PRF, a stepped frequency waveform is not feasible.

2.4 Received Signal Processing: Mixing and Quadrature Detection

Another important background concept of radar imaging applications is the received signal processing. The main blocks of received signal processing are the mixing and the quadrature detection. Of course there are many other special and necessary signal processing step such as clutter rejection; detector error compensation etc, but they are all out of the scope of this thesis.

Mixers

Mixers are used for frequency translation of RF input signals. Received RF echo signals are translated to some lower IF by the use of mixers.

Figure 2.4(a) illustrates a standard mixing operation and mixer outputs, [4]. Two RF input signals produce a mixer product, s(t), which contain frequencies equal to the sum and difference of the two input signal frequencies.

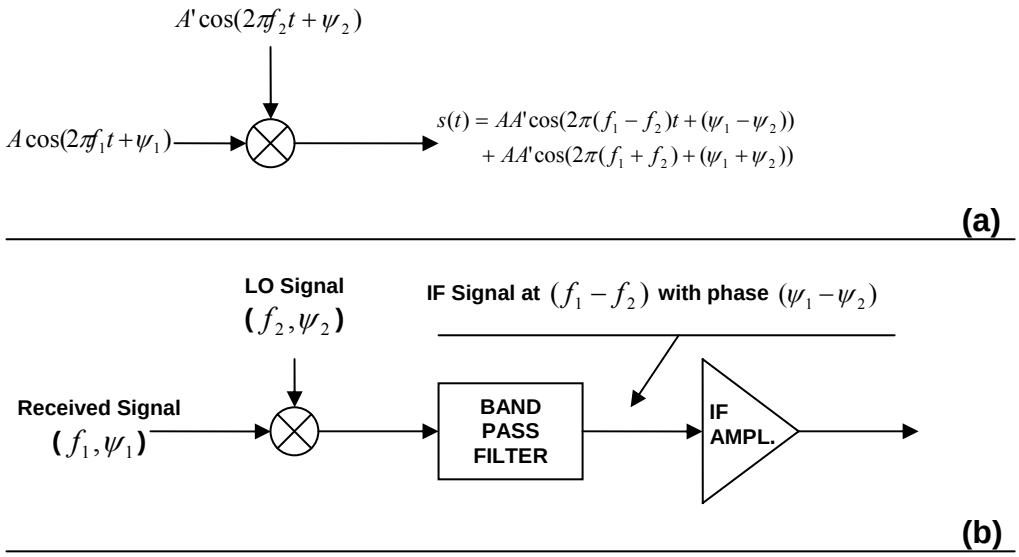

Figure 2.4 Mixing (a) mixer products of two sinusoidal input signals; (b) superhet mixer

Typically, a fixed-frequency local oscillator (LO) signal is mixed with relatively lower level received signal (reflected by the observed target) to produce a difference frequency output called the IF signal. A receiver that uses a mixer in this manner to translate a frequency band of signals down in frequency to a convenient IF band is called a *superheterodyne (superhet) receiver* [4].

The required IF signal could be obtained by using a Band-Pass Filter, as shown in the Figure 2.4(b), such that only the difference frequency signal appears at the output of the filter. In practical designs, received target response is one of the inputs and the other is the fixed-frequency local oscillator (LO) signal.

Quadrature Detection

Quadrature detection is used to recover received signals phase relative to the transmitter carrier. As it was discussed in the previous chapter, received signal's phase information, which includes the target's Doppler shifts, relative to the fixed-frequency carrier of the transmitted pulse, has a critical importance and necessity for ISAR imaging.

Quadrature detection can be thought of as a mixing operation that translates the received signal to baseband to recover amplitude and phase in the form of quadrature components [4].

Figure 2.5 illustrates a standard quadrature detector [4]. For *quadrature mixing* operation, both the LO signal and received signal carrier are at the same frequency, different than the Figure 2.4. The only difference is the *embedded* Doppler shift information, $(\psi_1 - \psi_2)$, in the received signal.

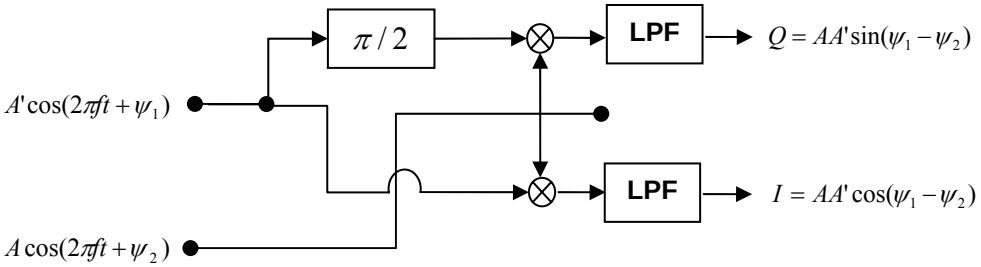

Figure 2.5 Quadrature detector

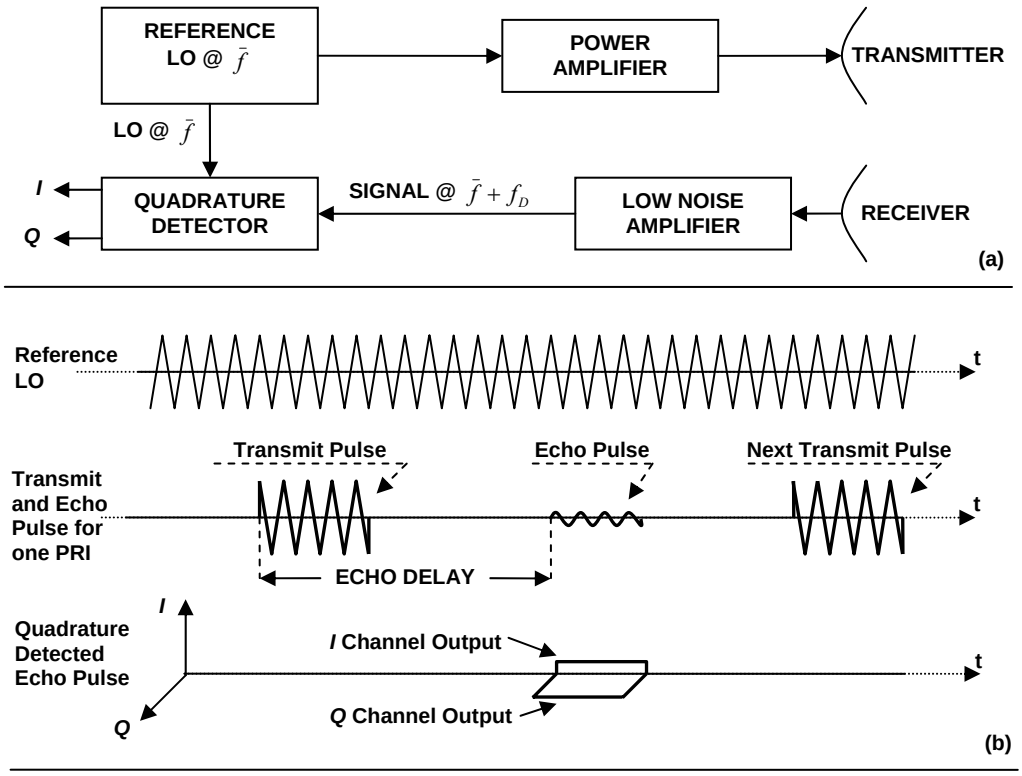

Figure 2.6 (a,b) Quadrature detection; (a) idealized coherent radar; (b) waveforms for quadrature detection

The output of the lower mixer is called *inphase (I)* output. A second mixer with the reference signal delayed by $\pi/2$ rad of phase produces a *quadrature (Q)* output. *I* and *Q* output video pair is called the *baseband signal*. A Doppler-shifted echo signal will produce a baseband signal at the Doppler frequency.

Figure 2.6(a,b) illustrates the quadrature detection. Practical systems are likely to operate as shown in Figure 2.6(c), so that filtering and amplification can be done more conveniently at lower frequencies [4].

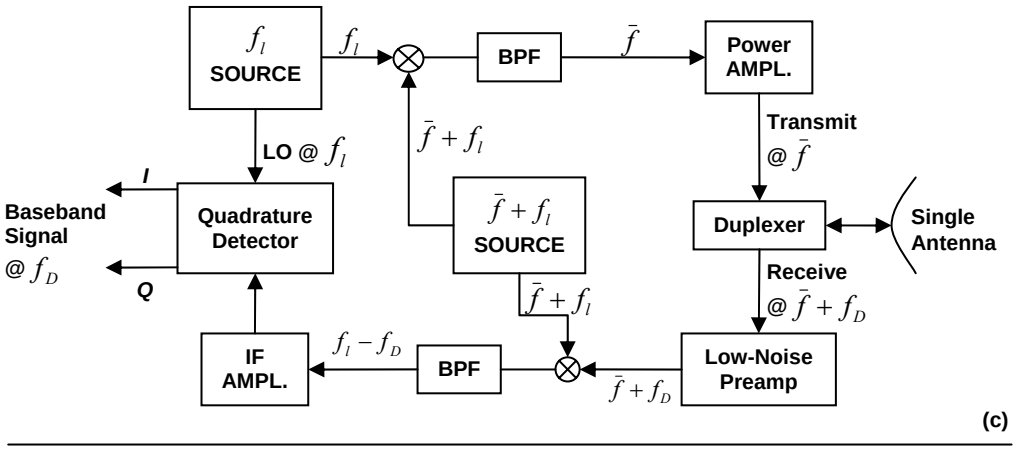

Figure 2.6 (c) Practical Design

2.5 Range Profile Concept

A ***Range Profile*** (RP) represents a one-dimensional range projection of a target's complex electromagnetic response onto the RLOS. The term ***High Resolution Range Profile*** (HRRP) is also used instead of the term Range Profile, in many of the references.

Figure 2.7 illustrates the main and basic idea of the RP generation. The scatterer positions on the target are projected onto the RLOS in the range dimension.

$d_1,.....,d_6$ represent the distances from the radar to the individual scatterers. $a_1,.....,a_6$ represent the amplitudes of the backscatter from the discrete scattering centers.

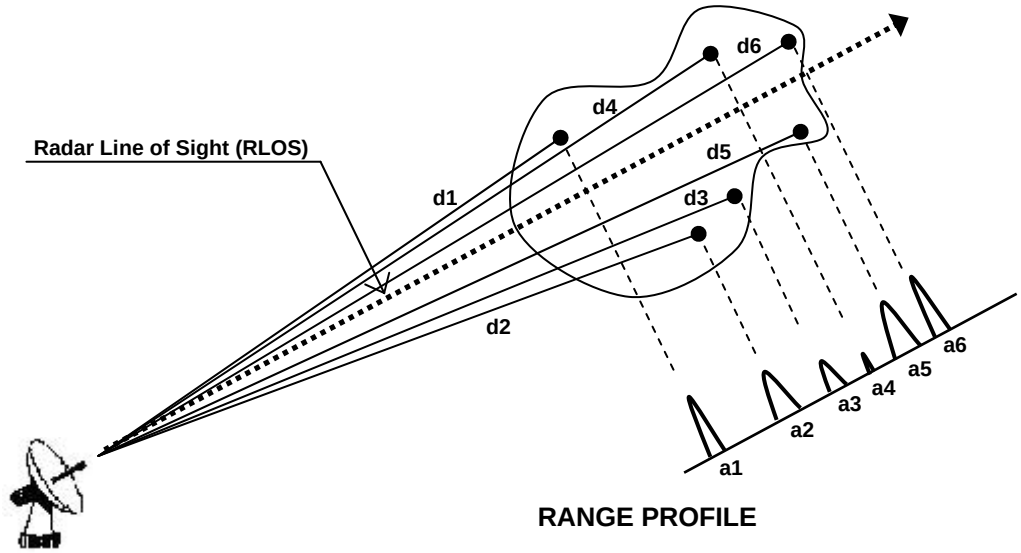

Figure 2.7 The relationship between a RP, the radar and the target

Examples of RPs generated from simulated targets are shown in Figure 2.8. Figure 2.8(a,c,e) represent the simulation models by the way of their ISAR images. Figure 2.8(b,d,f) are the related RPs. The basics of these simulations are going to be examined in the following sections.

A RP separates the scatterers on a target in slant-range only. If a number of target scatterers exist in a particular range cell (bin), then their backscatter returns are combined coherently at the radar receiver and it becomes impossible to identify the individual scatterer returns from the range profile. An example of this situation could be very well observed in Figure 2.8 (c,d). 3rd and 8th; 4th and 9th; 6th and 10th and 7th and 11th point scatterers fall in to the same range cell on the related range profile.

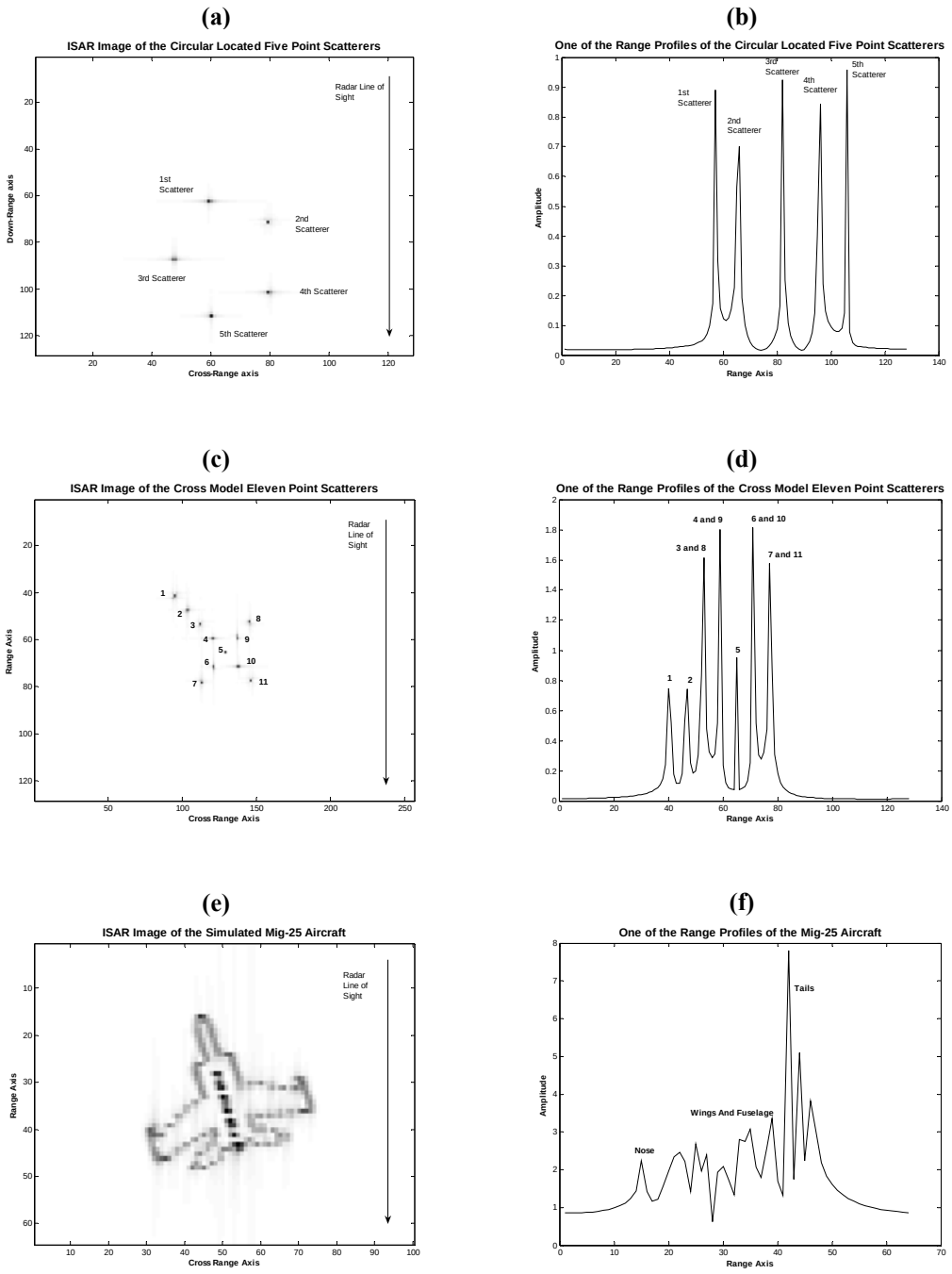

Figure 2.8 Some simulation examples to the range profile concept

Although Figure 2.8(b,d,f) represents the ***magnitude of the Range Profiles***; a Range Profile is a complex signal and it also includes the phase information of the targets' echo response, which are not shown in Figure 2.8. This phase information makes the ISAR imaging possible.

2.6 Range Profile Generation Methods

Range profile generation methods could be divided in to two categories depending to the transmitted radar waveforms.

1. Real (Time) Range Profile Generation
2. Synthetic Range Profile Generation

Actually, the term *Real (Time) Range Profile Generation* is not used in the formal literature but it has to be used in this part of the thesis, as a fake term, in order to distinguish these two types of RP generation methods. Formal literature uses the term *Range Profile Generation*, by default, in order to refer to this fake term.

Real (Time) Range Profile Generation method is applicable for short-pulse and pulse-compression waveforms. In this method, a single RP could be generated for each transmitted pulse. Targets' electromagnetic responses (echoes) are sampled in *time domain*, in order to produce range profiles.

Synthetic Range Profile Generation method is applicable for only stepped frequency waveform types. These waveforms produces enough data for a single RP in every n pulses (one burst), where n is the number of discrete frequency steps used in the waveform. Only one inphase and quadrature pair of -*frequency domain*- sample is taken from each transmitted pulse, which corresponds to the frequency domain response of the target in that frequency. An IDFT transforms the discrete frequency samples (responses) into a *synthetic RP*. This process is called *synthetic,* because the target's range profile is not measured directly, but reconstructed from its frequency response. In order to prevent any misunderstanding, it has to be mentioned that the

word *Synthetic* in the term *Synthetic Range Profile Generation*, refers only to the generation method of the RP. It does have no relation with the *Synthetic* Aperture Generation and Inverse *Synthetic* Aperture terms.

As it could be understood from the previous paragraphs, Range Profile Generation is directly related to the data sampling concept and it is another basic concept of radar imaging applications. Type of the sampling and the level of the quantization depends on the type of the selected waveform and of course its bandwidth.

There are two sampling types, *time sampling* and *frequency sampling*. Short pulse and chirp waveforms are sampled by time sampling, where stepped frequency type radar signals are sampled by using frequency sampling.

2.6.1 Real (Time) Range Profile Generation and Time-Domain Sampling

Echo signals produced by a short-pulse radar, without introducing ambiguity, requires that the sampling rate meet the Nyquist criteria. Nyquist's sampling theorem states that if a radar signal has no frequency component above some frequency f, then the signal is completely determined by sample values of the signal separated in time by $1/2f$, extending over the signal duration. It is not feasible to sample the RF form of radar echo signal at this rate. To reduce the required sampling rate, the signal is usually mixed down to baseband [4].

A target response produced by a single short transmitted pulse which has a bandwidth of β, and its spectrum is illustrated in Figure 2.9(a) and Figure 2.9(b) respectively [4]. Maximum frequency components of the down-converted baseband version of the echo signal are then reduced to $\beta/2$, as shown in Figure 2.9(c). When converted to the baseband, the echo signal is composed of inphase (*I*) and quadrature (*Q*) components, each having a spectrum as shown in Figure 2.9(c). If the LPF's bandwidth is equal to the $\beta/2$, sample spacing in time must be equal to or less than $1/\beta$ sec for both *I* and *Q* outputs, according to the Nyquist's sampling criteria. One

sampled *I-Q* pair of real samples taken simultaneously is called *complex sample*. The echo signal is unambiguously determined by β complex samples per second. Actually, total number of the required complex samples, to produce a RP, is related to the target's physical properties (target's extent in the direction of the RLOS) and most probably it is much less than β. Thus, β gives an idea about the sampling rate only. Baseband samples of the echo signal of Figure 2.9(a) are indicated in Figure 2.9(d).

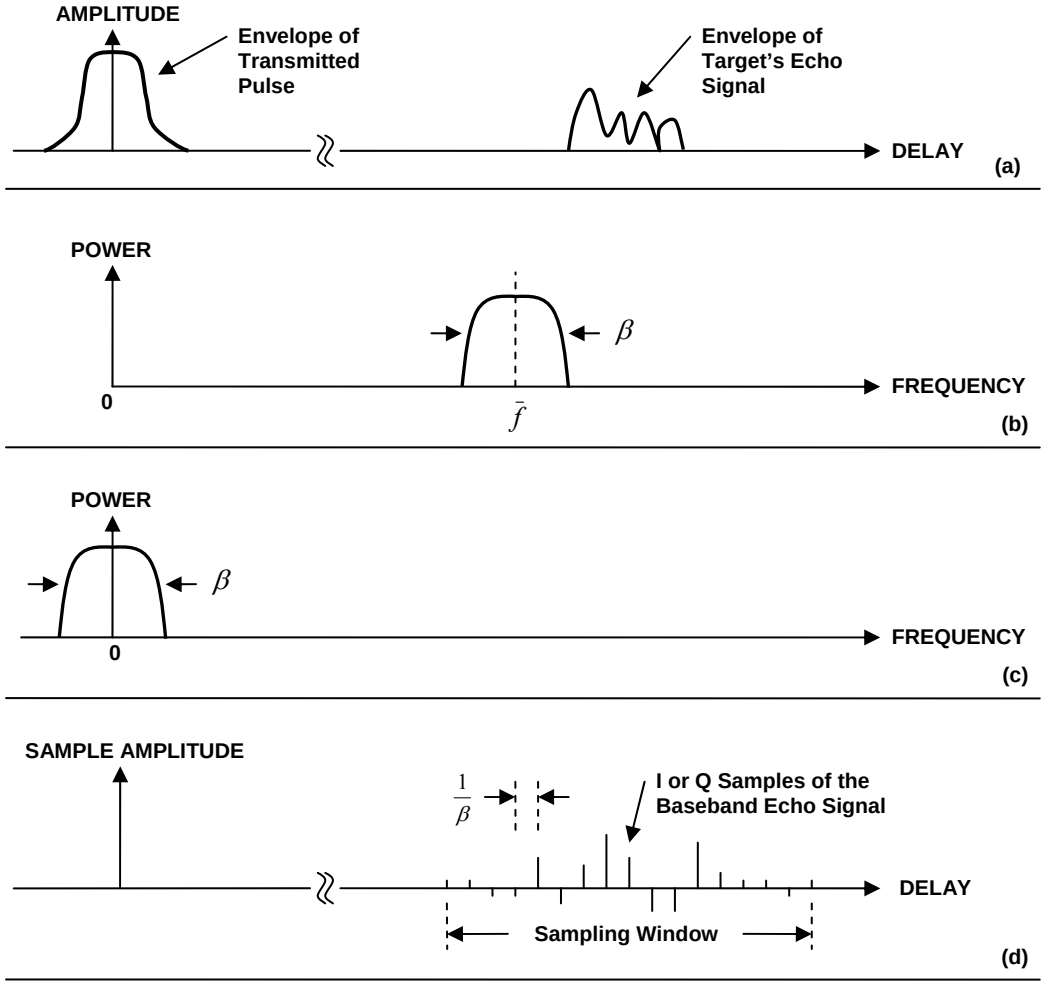

Figure 2.9 **(a) Echo signal;(b) signal spectrum (c) baseband signal spectrum, (d) sampling**

Complex RP's could be generated simply by the summation of these inphase and quadrature components:

$$RP_k = \sum_{i=1}^{N} (I_i + jQ_i) \tag{2.3}$$

where, N is the number of samples and k refers to the kth RP.

Even at baseband, the required sampling rate for high resolution radar is high. As an example, to achieve 0.25m resolution, the received signal bandwidth from Equation (2.1) is,

$$\beta \approx \frac{c}{2\Delta r_s} = \frac{3 \times 10^8}{2 \times 0.25} = 600\ MHz \tag{2.4}$$

which means 600 x 10^6 complex samples per second.

2.6.2 Synthetic Range Profile Generation and Frequency-Domain Sampling

Any signal could be represented as either a time or frequency function. The echo signal from a range-extended target (the term range-extended is used to clarify that the target is not point shaped; it has an extension in range) illuminated by a typical radar RF pulse is usually observed in the time domain [4]. Its amplitude and phase variation with respect to the frequency is called the *echo signal spectrum*, which is a *frequency-domain description* of the signal.

Since the descriptions of a signal, as functions of time and frequency are equivalent, the signal spectrum can be obtained from time-domain response and time domain response can be obtained from signal's spectrum. Thus, measurements of target's echo signal in the time and frequency domains provide equivalent data for determining the target range profiles [4].

If a series of RF pulses were transmitted *stepped in frequency* from pulse to over a bandwidth β, the set of sampled echo amplitude and phase measurements made relative to each transmitted pulse can be transformed by the IDFT process into the range-profile equivalent of echo amplitude and phase measurements obtained relative to a transmitted short RF pulse of bandwidth β [4].

Stepped frequency type of radar signals, synthetic range resolution and synthetic range profiles take an important role in this thesis since all of the simulations are generated by the way of this kind of radar signals.

Frequency domain sampling can be carried out by collecting an *I* and *Q* sample pair, at a *selected range-delay position of the response* for each pulse of the step frequency modulated burst. Complex samples, collected at a target's range-delay position along the received responses from such a pulse sequence, can be thought of as discrete frequency-domain samples (responses) of the target's reflectivity, if the target reflectivity can be assumed to remain constant during the burst.

Frequency Step Size and Bandwidth

The most important issue in the frequency sampling and Synthetic Range Profile Generation is the determination of the required frequency spacing (*Frequency Step-Size*), Δf, which is an important design criteria for step-frequency radars. In order to determine the required frequency step-size for unambiguous sampling in the frequency domain, we must consider Nyquist's theorem for sampling in the frequency domain. This theorem states that the spectrum of a signal is exactly determined by samples of spectrum separated by $1/(2\delta t)$ Hz when the signal is zero everywhere, except during the delay interval δt. The delay interval δt is associated with the targets range extent, on the direction of propagation (or RLOS, in other word) with,

$$2l = c\,\delta t$$

$$\delta t = 2l / c \tag{2.5}$$

In Equation (2.5), the factor two (2) comes from the round-trip time delay. Thus, for unambiguous sampling of a target's reflectivity in the frequency domain, real frequency samples are required to be taken at intervals of,

$$\Delta f \le \frac{1}{2\delta t} = \frac{c}{4l} \tag{2.6}$$

complex samples (*I*-*Q* pair) may be taken at $\Delta f = c/(2l)$.

As an example, the frequency steps required for unambiguous frequency-domain sampling of a 300 m target must be spaced by a maximum of

$$\Delta f = \frac{c}{2l} = \frac{3\times 10^8}{2\times 300} = 0.5\ MHz \tag{2.7}$$

If the range resolution has to be 0.25 m, 1200 complex frequency samples are required for a total bandwidth of 1200 x 0.5 MHz = 600 MHz.

Pulse Duration

Another important issue is the duration of the transmitted pulse. What will be the criteria for pulse duration? The aim is to sample the target's echo response only once a time in a pulse which does mean only one I-Q sample pair is required for each pulse. At the sampling time, all of the scatterers' electromagnetic responses has to be included in the echo pulse. Hence, the duration of each transmitted stepped-frequency pulse need only be sufficient to produce an approximation of the steady-state echo response. This is achieved for a pulse duration that is somewhat greater than the target range-delay extent.

As an example, required minimum duration of the transmitted pulse for a target of 300 m length is,

$$T_P\big|_{\min} = \frac{2l}{c} = \frac{2\times 300\,m}{3\times 10^8\ m/\sec} = 2\mu\sec \tag{2.8}$$

2.7 Synthetic Range Profile Generation Algorithm

In this section, a technique is going to be described for obtaining target range-profile signatures synthetically by processing echoes resulting from narrowband transmitted pulses stepped in frequency.

Synthetic range profile generation process is illustrated in Figure2.10 with a block diagram representation.

Each stored burst of target signal data, G, approaches the equivalent of the instantaneous discrete spectral signature of the target seen at the same bandwidth and center frequency if the following conditions are met [4]:

a) burst times are short relative to time associated with significant target aspect change,
b) the duration of the baseband response exceeds the target range-delay extent,
c) the frequency step size is less than reciprocal of the target range-delay extent.

The process is going to be described analytically by considering a single point target with radial motion (motion in the direction of the radar LOS) relative to the radar. N-element stepped frequency pulses (one burst) with resulting echoes from a moving target are shown in Figure 2.11 [4]. The point target is assumed to have velocity v_t toward the radar and is at an initial range R when time is zero.

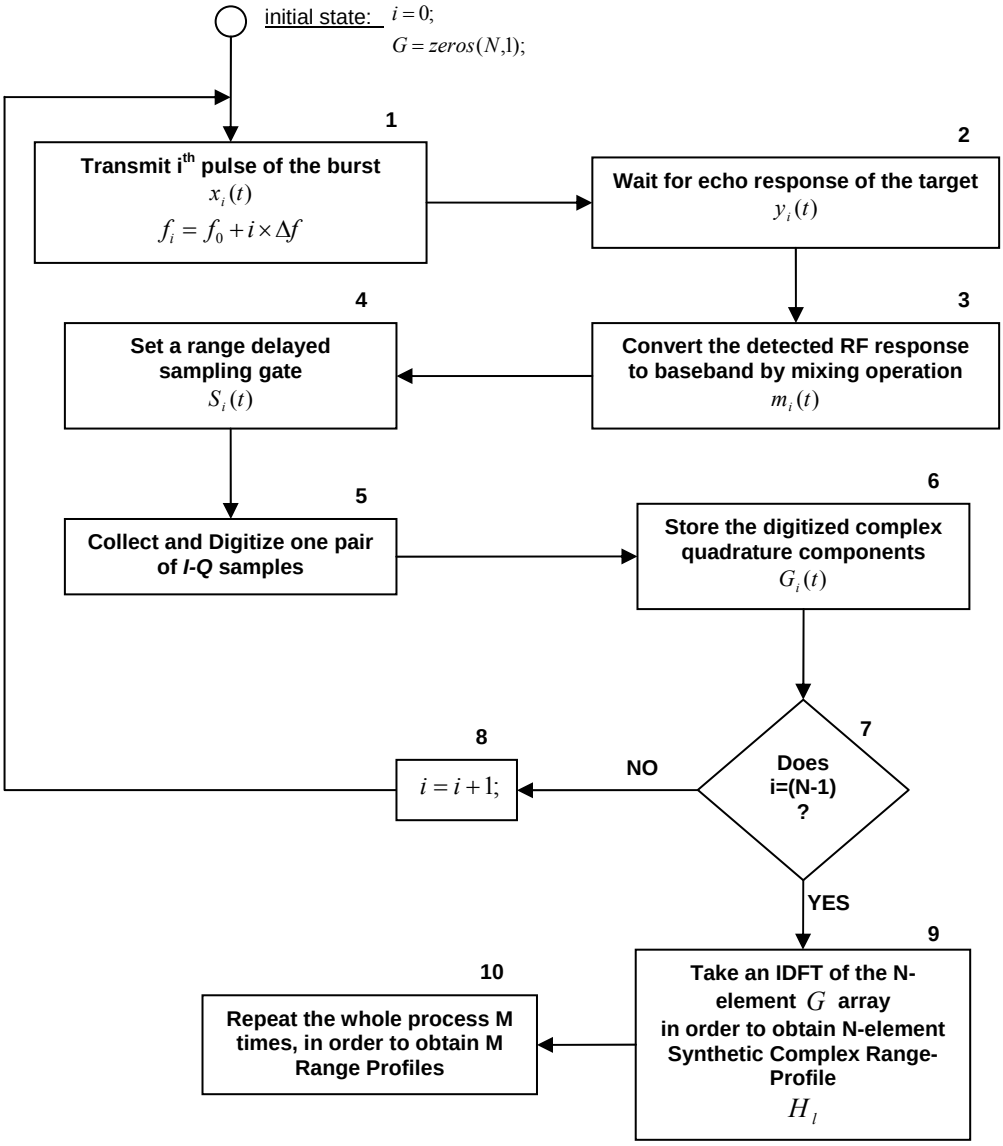

Figure2.10 Block diagram of synthetic range-profile generation

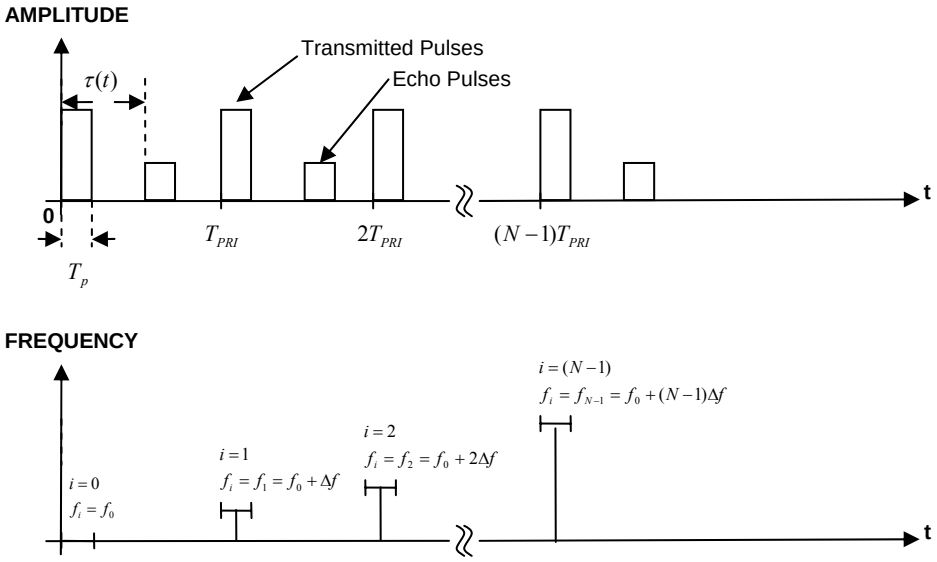

Figure 2.11 Stepped-frequency waveforms and echo pulses

First step is generation and transmission of the radar signal, $x_i(t)$. Transmitted signal frequency, f_i is increased in each transmission by an amount of frequency step size, Δf.

$$x_i(t) = \begin{cases} B_i \cos(2\pi f_i t + \theta_i), & iT_{PRI} \le t \le iT_{PRI} + T_p \\ 0, & otherwise \end{cases} \qquad i = 0 \; to \; (N-1) \qquad (2.9)$$

where T_{PRI} is the pulse repetition interval, T_p is the pulse duration, θ_i is the relative phase and B_i is the amplitude of the *i*th pulse.

Second step is the detection of the target's echo response, y_i. The received signal can be expressed as,

$$y_i(t) = \begin{cases} B_i' \cos\{2\pi f_i[t - \tau(t)] + \theta_i\}, & iT_{PRI} + \tau(t) \le t \le iT_{PRI} + T_p + \tau(t) \\ 0, & otherwise \end{cases} \qquad (2.10)$$

where $B_i^{'}$ is the amplitude of the i[th] received pulse at frequency f_i. Range delay for the target, which has an initial range *R* at time t=0 is

$$\tau(t) = \frac{R - v_t t}{c/2} \tag{2.11}$$

The baseband mixer product output from the inphase mixer is,

$$m_i = \begin{cases} A_i \cos\{-2\pi f_i \tau(t)\}, & iT_{PRI} + \tau(t) \le t \le iT_{PRI} + T_p + \tau(t) \\ 0, & otherwise \end{cases} \qquad i = 0 \; to \; (N-1) \tag{2.12}$$

where A_i is the amplitude of the mixer output at frequency step *i*. The phase of the mixer output is,

$$\psi_i(t) = -2\pi f_i \tau(t) \tag{2.13}$$

This equation can be rewritten by using (2.11) as,

$$\psi_i(t) = -2\pi f_i \left(\frac{2R}{c} - \frac{2v_t t}{c} \right) \tag{2.14}$$

Equation (2.14) is the total echo phase advance seen from transmission to reception for i[th] pulse.

The next step is sampling of the received baseband echo signal, m_i. In order to take a steady-state complex-sample from the echo pulse, the sample has to be taken from the middle part of the echo response. Because initial (end) part of the echo may not include the back-side (front-side) response of the target and, end part of the echo may not include the front-side response. So, the sampling time, S_i, is defined as,

$$S_i = iT_{PRI} + \frac{2R}{c} + \tau_r \tag{2.15}$$

where the above requirement is met by the τ_r, the receiving system transfer delay, which is typically half of the pulse duration; $T_p/2$. S_i, is advanced pulse to pulse to

produce a sample near the center of each echo response at baseband. Then, the phase of the sampled quadrature mixer output in Equation (2.14) becomes,

$$\psi_i\big|_{t=S_i} = -2\pi f_i\left[\frac{2R}{c} - \frac{2v_t}{c}\left(iT_{PRI} + \frac{2R}{c} + \tau_r\right)\right] \tag{2.16}$$

The sampled output from the inphase mixer is $m_i = A_i \cos(\psi_i)$. The sampled mixer output from both *I* and *Q* channels can be represented as,

$$\begin{aligned} G_i &= A_i(\cos\psi_i + j\sin\psi_i) \\ G_i &= A_i e^{j\psi_i} \end{aligned} \tag{2.17}$$

where $G_0,.....,G_{N-1}$ are the samples of target reflectivity in the frequency domain. Let us assume that these complex values are stored in an array, G. Then, IDFT of this N-element array gives a series of range-delay reflectivity estimates, H_l, which is the complex range profile of the target.

$$H_l = \sum_{i=0}^{N-1} G_i e^{j(2\pi/N)li}, \qquad 0 \le l \le N-1 \tag{2.18}$$

where l is the slant range position.

The last step is the repetition of the whole process M times, in order to obtain M range-profiles. This is necessary to construct an ISAR Image, since generation of synthetic cross-range resolution requires coherent processing of many Range-Profiles.

CHAPTER 3

CONVENTIONAL ISAR PROCESSING: RANGE-DOPPLER IMAGING

3.1 Introduction

In this chapter, Conventional ISAR Processing Method: Range-Doppler Imaging is introduced. First of all, image dimensions are examined by the way of their resolution and image window concepts. These concepts are easy to understood, since previous chapters give detailed examinations about the basics of these concepts. Then, ISAR image generation method with stepped-frequency radar waveforms is explained and some primitive, but very important ISAR imaging examples are presented.

Effect of the target's motion on ISAR images and motion compensation concepts are going to be explained in the following chapters but the seeds of the curious about these concepts are sprinkled in this chapter.

3.2 Image Dimensions

ISAR images consist of estimates of the magnitude and position of scatterers in the slant-range and cross-range. As it was said in the previous chapters, the slant-range is the radar LOS range dimension and the cross-range is the dimension lying normal to the plane contained by the radar LOS and target rotation axis.

The Range-Doppler model is going to be used to develop expressions for slant-range and cross-range resolution; sampling requirements, and target image plane.

Range-Doppler imaging is very well discussed by and the principles are settled in [2,8,9].

3.2.1 The First Dimension: Slant-Range

Slant-range resolution and slant-range window criteria are examined for chirp and stepped-frequency type of radar waveforms.

Slant-Range Resolution

Rayleigh resolution for *chirp waveforms*, from Equation (2.1), is,

$$\Delta r_s = \frac{c}{2\beta} \tag{3.1}$$

where β is the chirp bandwidth, c is the velocity of the light.

Synthetic Processing of *stepped-frequency waveforms*, as discussed in previous chapter, requires the conversion of echo data, collected in the frequency domain, into synthetic range profiles. This is typically carried out by using a DFT process.

The resolution for N steps of Δf Hz each, from Equation (2.1), is

$$\Delta r_s = \frac{c}{2\beta} = \frac{c}{2(N\Delta f)} \tag{3.2}$$

Slant-Range Window

Slant-range window is the extent of the ISAR image in the direction of the radar LOS. Slant-range window could be defined as the product of slant range resolution and number of collected samples to produce a range-profile.

A sampled target range-profile received from the transmission of a single chirp pulse is illustrated in Figure 3.1. The unambiguous sampled slant-range extent, called the slant-range window, is given by

$$w_s = N\Delta r_s = N\frac{c}{2\beta} \tag{3.3}$$

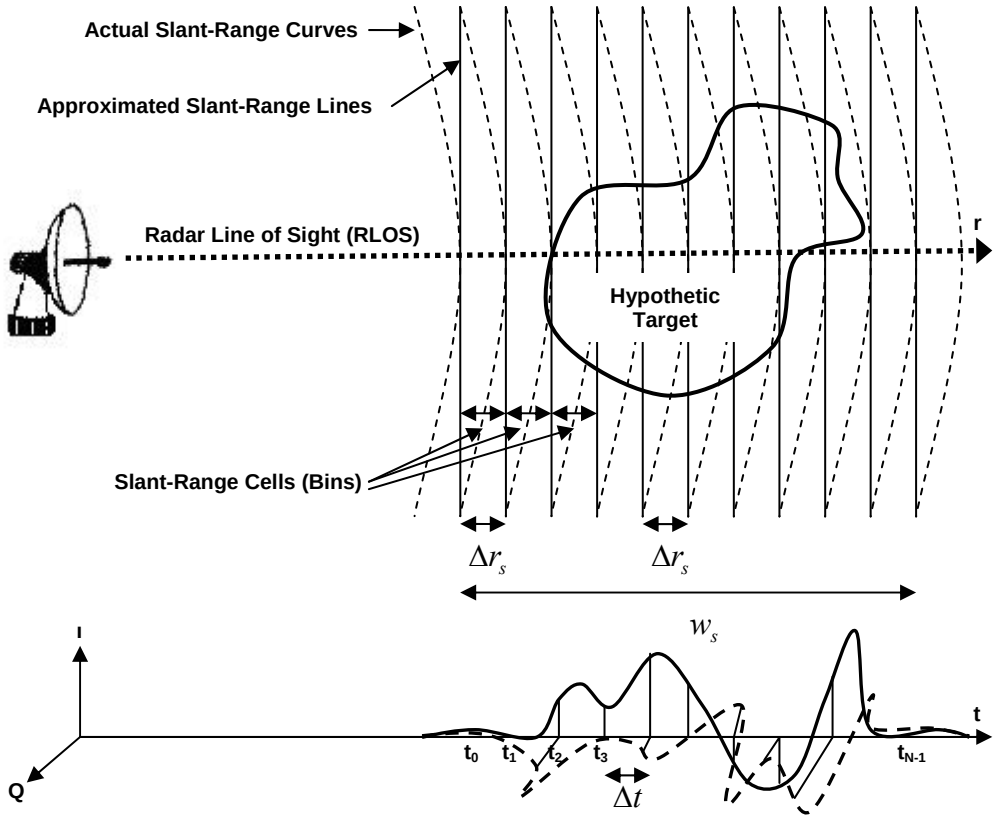

Figure 3.1 Slant-range resolution and slant-range window

Samples are obtained by using some form of range tracking that starts the first sample just before the target echo arrives from each pulse. Following samples are collected during a total delay interval corresponding to the slant-range window given by Equation (3.3).

As it was explained in the synthetic range-profile generation concept, synthetic range window is effectively sampled by the N samples per burst collected over bandwidth $\beta = n\Delta f$. Hence, slant-range window for the stepped-frequency waveforms is given by,

$$w_s = N\Delta r_s = \frac{c}{2\Delta f} \tag{3.4}$$

The term *range ambiguity window* is also used instead of slant-range window, in the case of stepped frequency waveforms.

Relationship Between Target Extent and Slant Range Window

What if target's range-delay extent (length of the target in the direction of the radar LOS) exceeds the slant-range window and what kind of situation or a lack of design would produce this kind of an effect?

The answer has to be examined for chirp and stepped-frequency type of waveforms separately.

Firstly, let us investigate the case of chirp type of radar waveforms. As it was discussed in the previous chapter and as it was illustrated in Figure 3.1, range-profiles are generated by time sampling of the target's echo responses. Hence, targets that exceed the slant-range window defined by the Equation (3.3) is going to be imaged over only that portion of the range-delay extent of the target where samples are taken, since the range-profiles are going to involve only that portion of the target scatterers' echo responses. This situation is illustrated in Figure 3.2.

The answer is a little bit complicated for the stepped-frequency type of radar signals. Equation (3.4) states that the slant-range window is only related to the frequency step-size, Δf . Hence, if the frequency step-size is increased, the slant-range window shrinks at the same time (if the number of frequency steps, N , is kept constant). In other words, if the frequency step-size, which is a design criteria, is chosen for a target of range-delay extent equal to w_s , then the targets that exceed the range

ambiguity window will produce range-profiles (and images) that are folded over within the range-window.

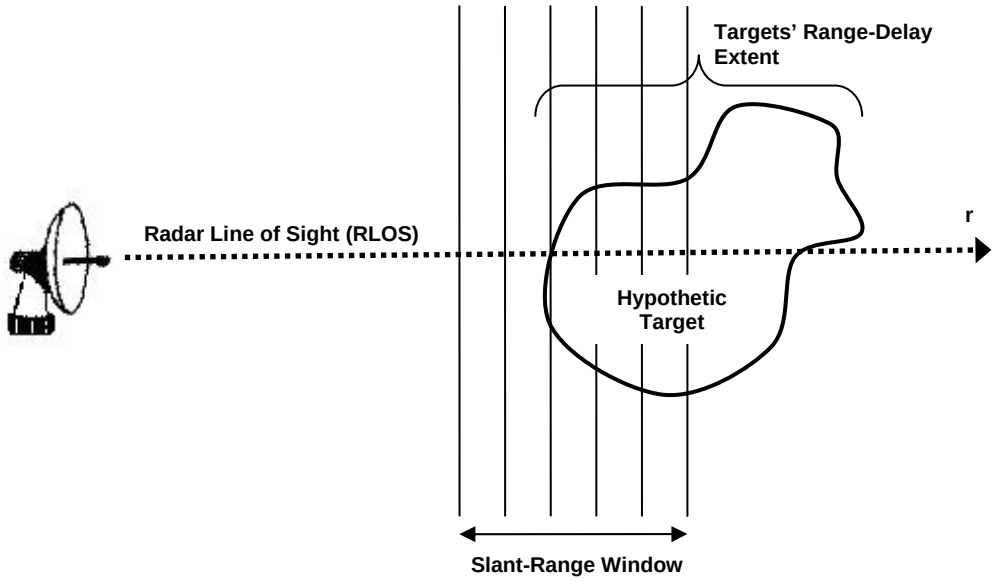

Figure 3.2 Targets' range-delay extent exceeds the slant-range window

An example of this kind of slant-range *fold-over* is illustrated in Figure 3.3 and Figure 3.4. Figure 3.3 shows the simulation model by the way of point scatterers' spatial distributions. Five point-scatterers are located on the edges of a hypothetical pentagon and one point-scatterer at the center. Simulation parameters are listed in Table 3.1.

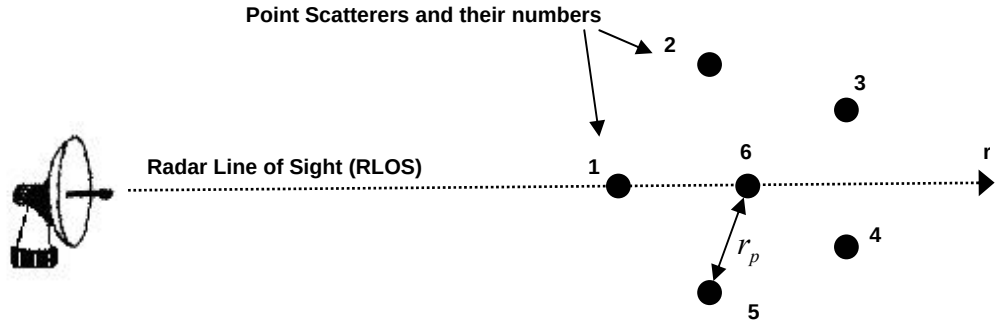

Figure 3.3 Description of the simulation model: scatterers' spatial distribution

Table 3.1 Simulation Parameters

Simulation Parameter		***Value***
Δf	: frequency step size	1 MHz
f_0	: starting frequency.	3 GHz
N	: the number of discrete pulses per burst.	128
M	: the number of bursts coherently processed to form an ISAR image.	256
β	: the effective bandwidth of a burst.	128 MHz
T_P	: the pulse width.	5 us
T_{PRI}	: the pulse repetition interval (PRI).	50 us

The control-parameter of the simulation is the radius of the pentagon, r_p, which determines the target's range-delay extent. Related range-profiles and resultant ISAR images are shown in Figure 3.4 (a,b) for $r_p = 30m$.; Figure 3.4 (c,d) for $r_p = 70m$; Figure 3.4 (e,f) for $r_p = 100m$.

Slant-range resolution and slant-range window (range ambiguity window) could be calculated by the parameters, listed in Table 3.1, as

$$\Delta r_s = \frac{c}{2\beta} = \frac{c}{2(N\Delta f)} = \frac{3\times10^8}{2\times128\times10^6} = 1{,}172\, m \tag{3.5}$$

$$w_s = N \times \Delta r_s = 150\, m \tag{3.6}$$

which means that, if r_p is chosen as $r_p \geq 75\, m$, target's range-delay extent becomes larger than the slant-range window, hence fold-over of the range-profile and ISAR image could be observed. Figure 3.4 (e,f) illustrates this case, where $r_p = 100m$.

A Few Words About The Slant Range Resolution and Window

It is very useful to put a comment about the Equations (3.2) and (3.4) at this stage. As it could be seen from (3.4), the slant-range window depends only to the frequency step-size, Δf, for step-frequency radars and, number of pulses in a burst, N, determines the slant-range resolution.

An example of this comment is illustrated in Figure 3.5. Simulation model and parameters are same as in the Figure 3.3 and Table 3.1, except for the N, which is chosen as 16. $r_p = 30m$ is chosen. Then, the slant-range resolution becomes,

$$\Delta r_s = \frac{c}{2\beta} = \frac{c}{2(N\Delta f)} = \frac{3\times10^8}{2\times16\times10^6} = 9{,}3750\, m$$

Hence, as it could be seen from the Figure 3.5, 2nd 5th and 6th scatterers are no longer resolvable on the range-profile, although the slant-range window is constant.

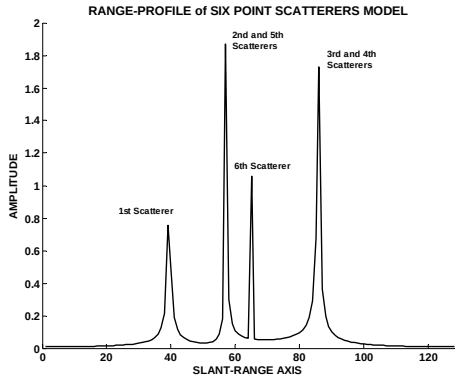

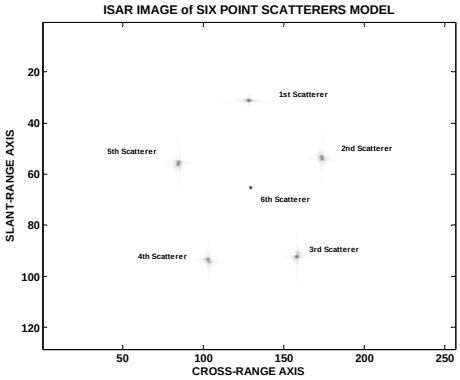

(a) $r_p = 30m$ **(b)** $r_p = 30m$

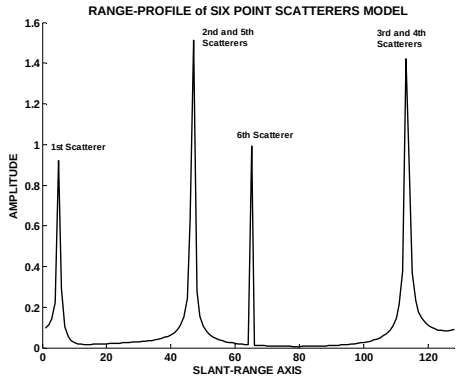

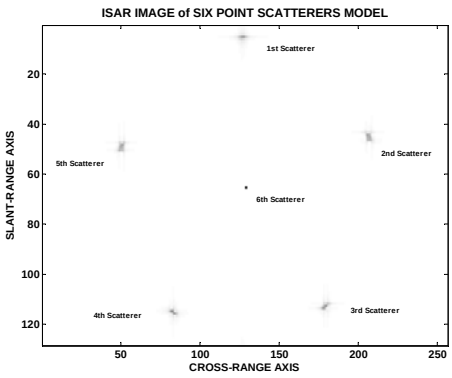

(c) $r_p = 70m$ **(d)** $r_p = 70m$

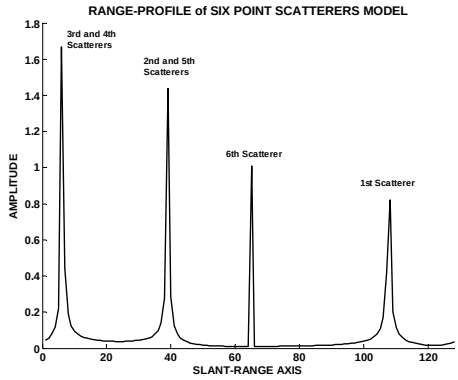

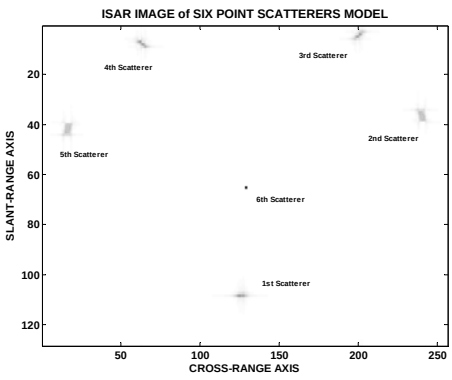

(e) $r_p = 100m$ **(f)** $r_p = 100m$

Figure 3.4 ISAR image and Range-Profile fold-over

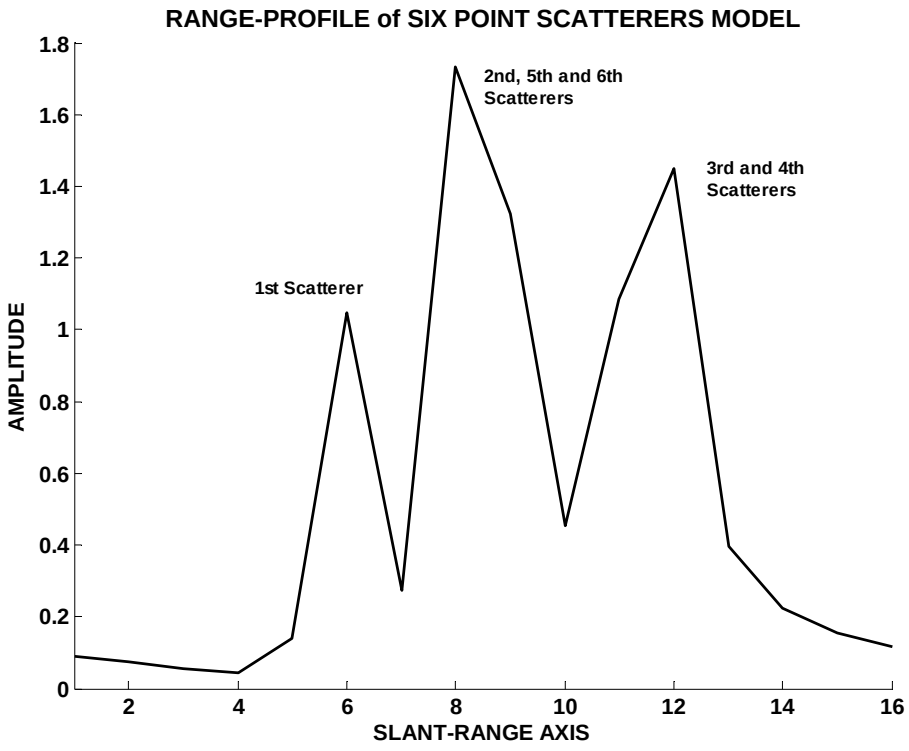

Figure 3.5 Low resolution range-profile of six point scatterer model, r_p=30m.

3.2.2 The Second Dimension: Cross-Range (Doppler)

In this section, a little bit further information about the generation of cross-range dimension in ISAR images is going to be exposed. Cross-range resolution and cross-range window criteria are going to be examined.

As it was introduced in the previous chapters, *cross-range resolution is obtained synthetically, by coherent processing of many range-profiles, along the range cells. What we need is to distribute the target scatterers, located in the same range cell of the generated range-profiles, to their spatial locations.* Logical illustration of this process is given in Figure 3.6.

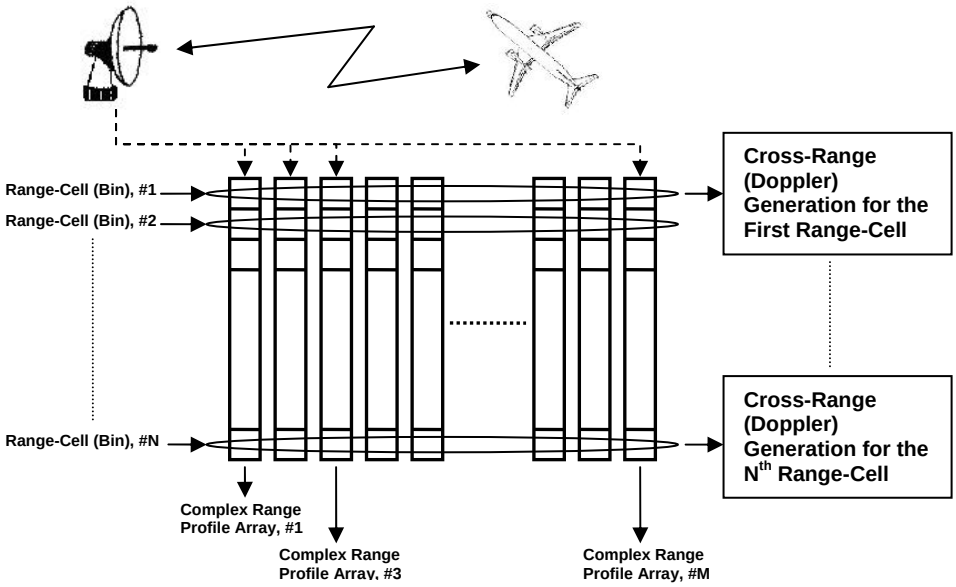

Figure 3.6 Cross-range (Doppler) generation logic

Cross-Range (Doppler) Resolution

The reason of availability of the cross-range information is the target's own rotation motion and resultant Doppler shift information in the echo pulses. This basic relation is illustrated in Figure 3.7 [4].

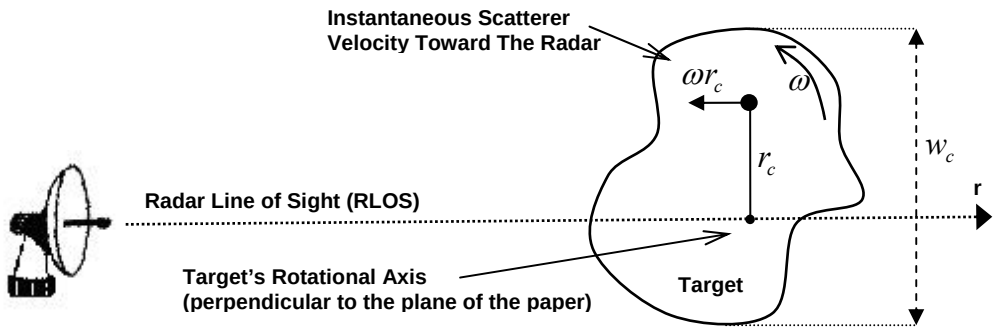

Figure 3.7 Radial velocity produced by a scatterer on a rotating target

The target has a cross-range extent of w_c and rotates at a constant angular rotation rate ω (rad/sec) about a fixed axis perpendicular to the plane of the paper. A single scatterer at a cross-range distance r_c could be seen with instantaneous velocity ωr_c toward the radar. The instantaneous Doppler frequency shift is

$$f_D = \frac{2}{c}\omega r_c \bar{f} = \frac{2\omega r_c}{\lambda} \tag{3.7}$$

where $\bar{f}$ is the carrier or center frequency of the radar. Let us assume that f_D is constant during the coherent integration time, T.

If two scatterers in the same slant-range cell are separated in the cross-range by a distance of δr_c, then the separation between the frequencies of the received signals, from Equation (3.7), is

$$\delta f_D = \frac{2}{c}\omega \delta r_c \bar{f} = \frac{2}{\lambda}\omega \delta r_c \tag{3.8}$$

so,

$$\delta r_c = \frac{c}{2\omega \bar{f}}\delta f_D = \frac{\lambda}{2\omega}\delta f_D \tag{3.9}$$

Then, for a radar that has a Doppler frequency resolution of Δf_D, the cross-range resolution could be expressed as,

$$\Delta r_c = \frac{c}{2\omega \bar{f}}\Delta f_D = \frac{\lambda}{2\omega}\Delta f_D \tag{3.10}$$

The Doppler resolution, Δf_D, is related to the coherent integration time, T, in terms of Rayleigh resolution, by,

$$\Delta f_D = \frac{1}{T} \tag{3.11}$$

Derivation and details of this relation could be found in [5]. Equation (3.10) could be rewritten as,

$$\Delta r_c = \frac{c}{2\omega T \bar{f}} = \frac{\lambda}{2\omega T} = \frac{\lambda}{2\,\Delta\theta} \tag{3.12}$$

where $\omega T = \Delta\theta$ is the aspect change seen by the radar (the term *coherent angle* is used in many of the sources). Typically, a DFT process is used to convert the set of time history samples collected in each range-cell during the time segment T into a discrete Doppler spectrum. An illustration of the process is given in Figure 3.8 [4], for stepped-frequency radar.

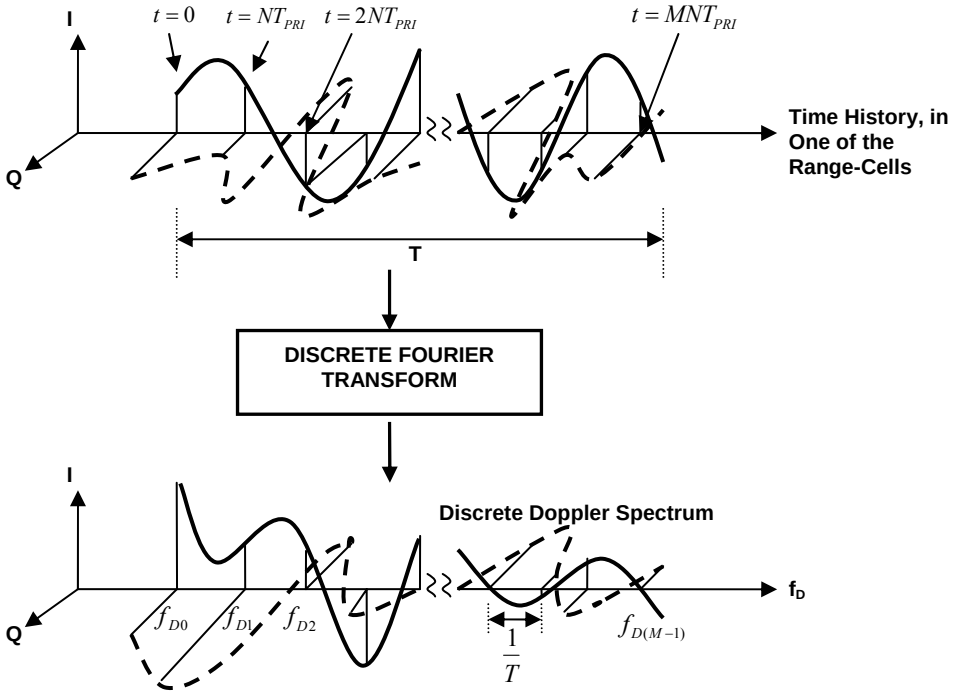

Figure 3.8 Sampled time history and associated doppler spectrum in one range-cell

In Figure 3.8, M is the number of range-profiles used to generate the cross-range extent of the target. Related time intervals between each time samples are NT_{PRI},

since N pulses are used to generate a range-profile. Hence, total coherent integration time, T, could be expressed as,

$$T = MNT_{PRI} \tag{3.13}$$

Cross-Range (Doppler) Sampling

Let us assume a target which has a cross-range extent of w_c and rotating at a rate of ω, as shown in the Figure 3.7. Then, the Doppler frequency bandwidth *produced* by this target could be expressed, referring to the Equation (3.8), as,

$$\beta_{D_{produced}} = \frac{2\omega w_c}{\lambda} \tag{3.14}$$

Referring to Figure 3.8, *obtained* Doppler frequency bandwidth of the stepped-frequency radar imaging system, could be expressed as,

$$\beta_{D_{obtained}} = M\frac{1}{T} = \frac{1}{NT_{PRI}} \tag{3.15}$$

The divisor, N, has to be omitted for the chirp-pulse radar imaging systems.

Hence, unambiguous sampling criteria could be stated, referring to the Equations (3.14) and (3.15), as,

$$\beta_{D_{obtained}} \geq \beta_{D_{produced}} \tag{3.16}$$

so,

$$\frac{1}{NT_{PRI}} \geq \frac{2\omega w_c}{\lambda} \tag{3.17}$$

From the radar point of view, only the number of pulses in a burst, N, and the pulse-repetition interval, T_{PRI}, parameters are controllable. But, as it could be remembered from the previous discussion about the slant-range resolution concept, number of

pulses in a burst is directly related to the slant-range resolution. Hence, the only independent parameter to optimize the cross-range sampling is the pulse-repetition interval, and could be expressed as,

$$\frac{1}{T_{PRI}} \geq \frac{2N\omega w_c}{\lambda} \tag{3.18}$$

Cross-Range (Doppler) Window

The unambiguous cross-range window extent could be expressed, referring to Equation (3.12), as,

$$w_{cr} = M\Delta r_c = M\frac{\lambda}{2\Delta\theta} \tag{3.19}$$

Cross-range related concepts are going to be examined in the following example. Simulation model of this example is illustrated in Figure 3.9. The Model looks like the one represented in Figure 3.3. The only difference is extra 3 point scatterer, so the scatterers are located on a hypothetical octagon of radius is equal to 70 m.

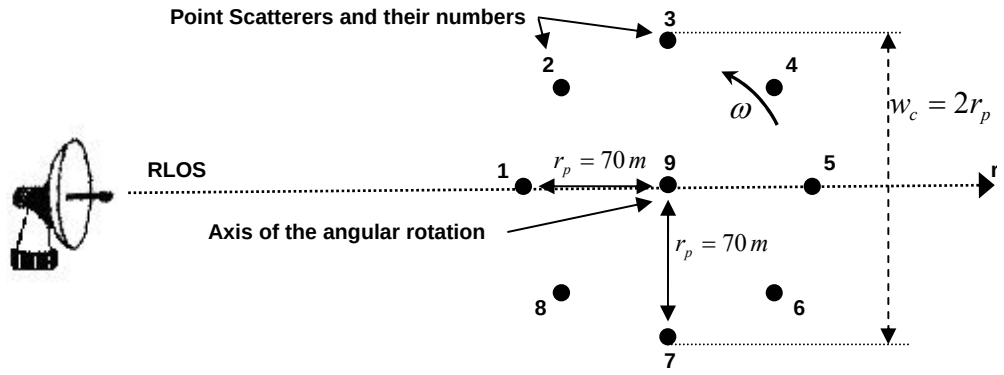

Figure 3.9 Description of the simulation model: scatterers' spatial distribution

The target is assumed to have a constant rotational motion, ω, during the data collection time (coherent integration time). Rotational motion axis is located at the middle of the geometry and perpendicular to the plane of the paper. Hence the target is said to be rotation on the axis of the 9th point scatterer. The target is assumed to have zero translational motion.

Radar parameters are chosen same as given in Table 3.1. Hence, slant-range resolution, from the Equation (3.5), is equal to the 1.1719 m. In order to achieve equivalent resolution in cross-range, total required aspect change of the target could be calculated from Equation (3.12) as,

$$\Delta\theta = \frac{\lambda}{2\Delta r_c} = \frac{0.1}{2\times 1.1719} = 0.0427\, radians = 2.445^\circ \tag{3.20}$$

Since,

$$\Delta\theta = \omega T = \omega MNT_{PRI} \tag{3.21}$$

angular rotation rate, ω, could be calculates as,

$$\omega = \frac{\Delta\theta}{T} = \frac{2.445}{128\times 256\times 50\times 10^{-6}} = 1.4921 \text{ deg/ sec} \tag{3.22}$$

Equation (3.20), (3.21) and (3.22) states that*, if a target has an angular rotation rate of 1.4921 deg/sec (or, total aspect change of 2.445 deg), regardless of its dimensions, it produces a cross-range resolution which is equivalent to the slant-range resolution.*

If the target has an angular rotation rate of 1.4921 deg/sec, related cross-range window could be calculated from Equation (3.19) as,

$$w_{cr} = M\Delta r_c = 256\times 1.1719 = 300\, m \tag{3.23}$$

according to the Equation (3.23), target's cross-range extent, $w_c = 2r_p$, is smaller than the total cross-range window, w_{cr}. This means that the target is completely

covered in the cross-range dimension, without any ***cross-range fold-over***. The term cross-range fold-over is not used in the formal literature, but it has to be, in order to explain the problematic cases.

The simulation is run for the four simulation cases with the parameters that are explained in Table 3.2, in order to strengthen the perception about the cross-range concept. Resultant ISAR images are illustrated in Figure 3.10, Figure 3.11, Figure 3.12 and Figure 3.13.

Table 3.2 Simulation cases and related parameters

	Parameter Description	***Case-1*** $\Delta r_c = \Delta r_s$	***Case-2*** $\Delta r_c \geq \Delta r_s$	***Case-3*** $\Delta r_c \leq \Delta r_s$	***Case-4*** $\Delta r_c \leq \Delta r_s$
Input Parameters	*Rotational Velocity* ω*, (degrees/sec)*	1.4921	1	2	3.8
	Target's cross-range extent w_c*, (m)*	140	140	140	140
	Coherent Integration Time T, seconds	1.6384	1.6384	1.6384	1.6384
Derived Parameters	*Total angular rotation,* $\Delta\theta$*, radians*	2.4447	1.6384	3.2768	6.2259
	Slant-Range Resolution Δr_s*, (m)*	1.1719	1.1719	1.1719	1.1719
	Cross-Range Resolution Δr_c*, (m)*	1.1719	1.7485	0.8743	0.4601
	Cross-Range Window w_{cr}*, (m)*	300	447.6	223.8	117.8
	Occurrence of Cross-Range Fold-Over, (YES/NO)	NO	NO	NO	YES

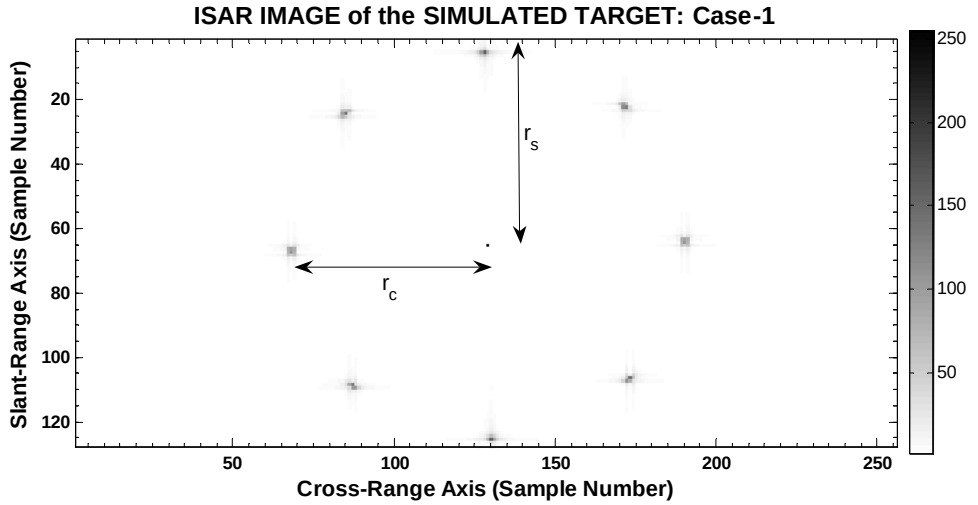

Figure 3.10 ISAR Image of the nine-points simulated target: Case-1

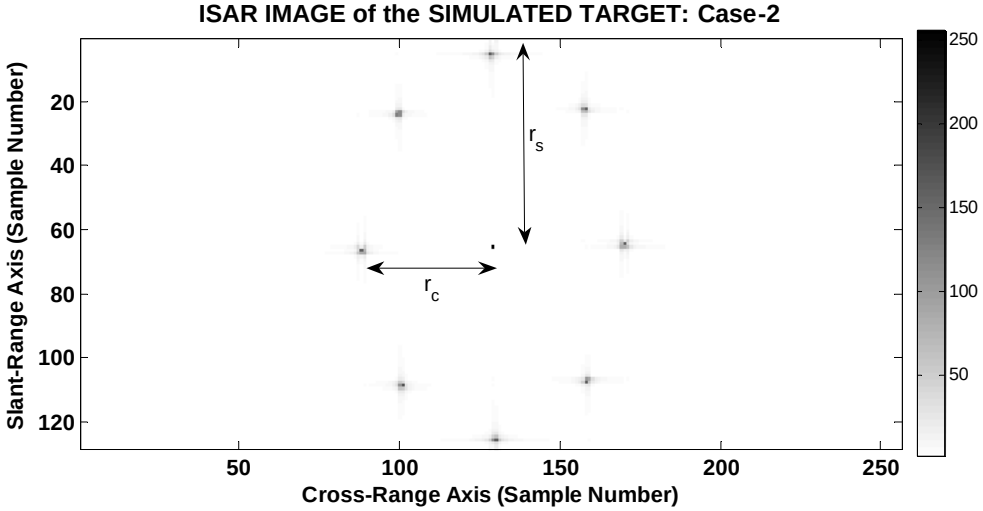

Figure 3.11 ISAR Image of the nine-points simulated target: Case-2

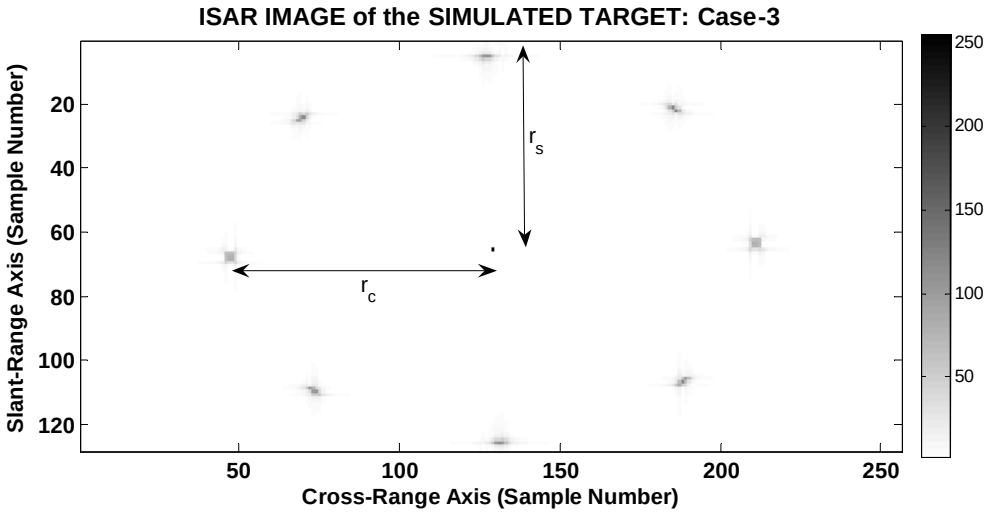

Figure 3.12 ISAR Image of the nine-points simulated target: Case-3

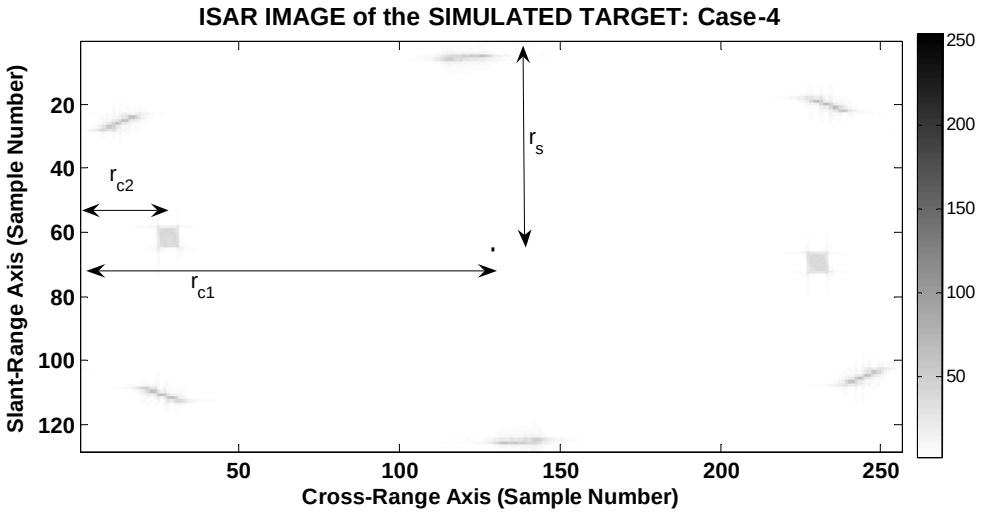

Figure 3.13 ISAR Image of the nine-points simulated target: Case-4

Two new abbreviations are used on these figures, r_s and r_c, which represent slant-range and cross-range extents of the ISAR images, respectively.

Figure 3.10 illustrates Case-1, where the cross-range resolution is equivalent to the range-resolution. Since actual length of the range and cross range extents, r_p, are equivalent, then

$$r_s = r_c \tag{3.24}$$

In Case-2, which is illustrated in Figure 3.11; slant-range resolution is better than the cross-range resolution. As a result of this, slant-range extent of the target *seems* wider than the cross-range extent,

$$r_s > r_c \tag{3.25}$$

In Case-3, which is illustrated in Figure 3.12; cross-range resolution is better than the slant-range resolution. As a result of this, cross-range extent of the target *seems* wider than the slant-range extent,

$$r_s < r_c \tag{3.26}$$

Case-4 is illustrated in Figure 3.13 and a good example of cross-range fold-over. In this case, total cross range extent of the target, 140 m, becomes larger than the total cross-range window's extent, 117.8 m. Hence, cross-range extent of the target could be represented as,

$$w_c = 2r_{c1} + 2r_{c2} \tag{3.27}$$

since $w_c > w_{cr}$.

Effect of the rotational motion on the resultant ISAR Images could be well observed in these figures: Minimum and maximum total aspect changes occur in Case-2 and Case-4, respectively. Although the higher aspect change means higher cross-range

resolution, it also results blurring and smearing in the images, which does mean worst ISAR Images.

3.3 Conventional ISAR Image Generation Stages for Stepped-Frequency Radars

In the light of the previous discussions, Conventional ISAR image generation stages are illustrated in Figure 3.14.

First stage includes initial data processing steps. Transmission, detection, sampling and storage of these samples occur at this stage. As a result of these procedures, *Target's Frequency Domain Signature* matrix is obtained. In this matrix, each column includes the response of the target to a single burst. Hence, number of the columns represents the number of the bursts.

In order to obtain Synthetic Range-Profiles, column-wise IDFT is processed. Then, row-wise (along the range-cells) DFT process is applied in order generate the cross-range information by the way of extracting the Doppler shift information.

Conventional ISAR Image, Range-Doppler Image in other words, is the magnitude of this matrix. Each element of this matrix represents a pixel on the ISAR image.

This method is also called *Fourier Based ISAR Image Formation*, because of the Fourier Transform application which is used in order to obtain Doppler (Cross-Range) information of the target.

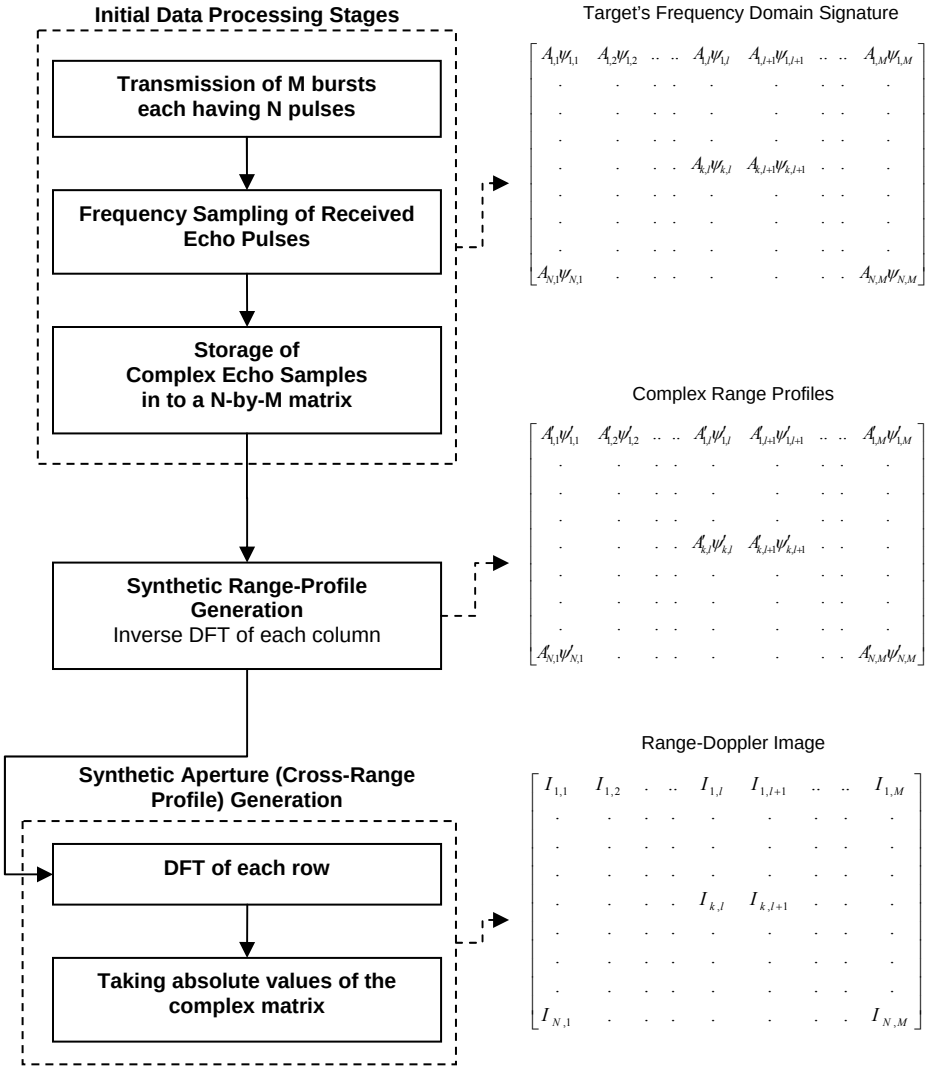

Figure 3.14 Conventional ISAR image processing stages

Some examples are illustrated in Figure 3.15, Figure 3.16, Figure 3.17, Figure 3.18, Figure 3.19 and Figure 3.20. Effect of the translational and rotational motion could be observed on these images.

First example is a stationary point source. Figure 3.15 illustrates the magnitudes of the range-profile matrix, by the way of its intensity and density images. Figure 3.16 illustrates related ISAR Images again by the way of intensity and density images.

Effect of Translational Motion of the Target: Range Walk

Second example is again a point source but with a constant translational velocity of 20 m/sec towards the radar, in the direction of the radar's LOS. Figure 3.17 and Figure 3.18 illustrates the Range Profile Matrix and ISAR images, respectively, by the way of intensity and density images.

Effect of translational motion could be very well observed by a comparison of Figure 3.15(b) and Figure 3.17(b). Translational motion of the target, within the coherent integration time, causes burst-to-burst shifts in range profiles of the target which means dispersion of the target's energy into several range-bins. In formal literature this effect is named as ***Range Walk***. Results of range-walk could be summarized as

1. Loss of range resolution,
2. Loss of range accuracy,
3. Loss of signal-to-noise ratio.

Loss of range resolution could be explained as follows. Let us assume that one more scatter is located very close to this scatterer. Then, because of the smearing effect of the translational motion, it could not be possible to resolve these two points.

Loss of range accuracy could be observed in Figure 3.18(b). Actual scatterer is point shaped; it has to occupy one range and one cross-range cell (pixel) on the ISAR image, as it was in Figure 3.16(b). But, as a result of translational motion, smearing exists in the ISAR images.

Loss of signal-to-noise ratio could be observed by a color-bar wise comparison of the Figure 3.16(b) and Figure 3.18(b). Under the translational motion, peak energy of the target's response decreases ten times of its stationary response.

Difficulty of the ISAR Image Generation

As it was explained in the previous sections, ISAR imaging is possible only if the observed target has a relative rotational motion with respect to the radar. Figure 3.19 illustrates an example of this situation (intensity images are omitted in this example). Simulation model is same with represented in Figure 3.9, with zero translational and zero rotational motions, which does mean stationary nine-point target geometry. Since the target does not exhibit a rotational motion, 2nd and 8th; 3rd, 9th and 7th; 4th and 6th scatterers appear in the same ISAR range-cross range cells (pixels) as they are in the range-profile matrix.

Another example is illustrated in Figure 3.20 in order to emphasize the effect of the target's motion on the ISAR images. Simulation model is same with the above one. Simulation parameters, including the rate of rotational motion, are chosen same as defined in the Table 3.2, in order to make a comparison of the resultant ISAR images which are represented in Figure 3.10 and Figure 3.20 (b). The only difference between these two simulation cases is the additive translational motion of 9 m/sec strength. Range wise fold over is a result of this additive translational motion. Smearing of the point sources in the ISAR image, and shifts in the tracks of the scatterers could be very well observed in Figure 3.20(b) and (a), respectively. Actually, 9 m/sec is too small for the translational motion but it is enough to blur the image. In order to give an idea about the effect of nearly realized translational motions on the image quality and the necessity of the motion compensation, one more example is illustrated in Figure 3.21 with the translational velocity of 100 m/sec.

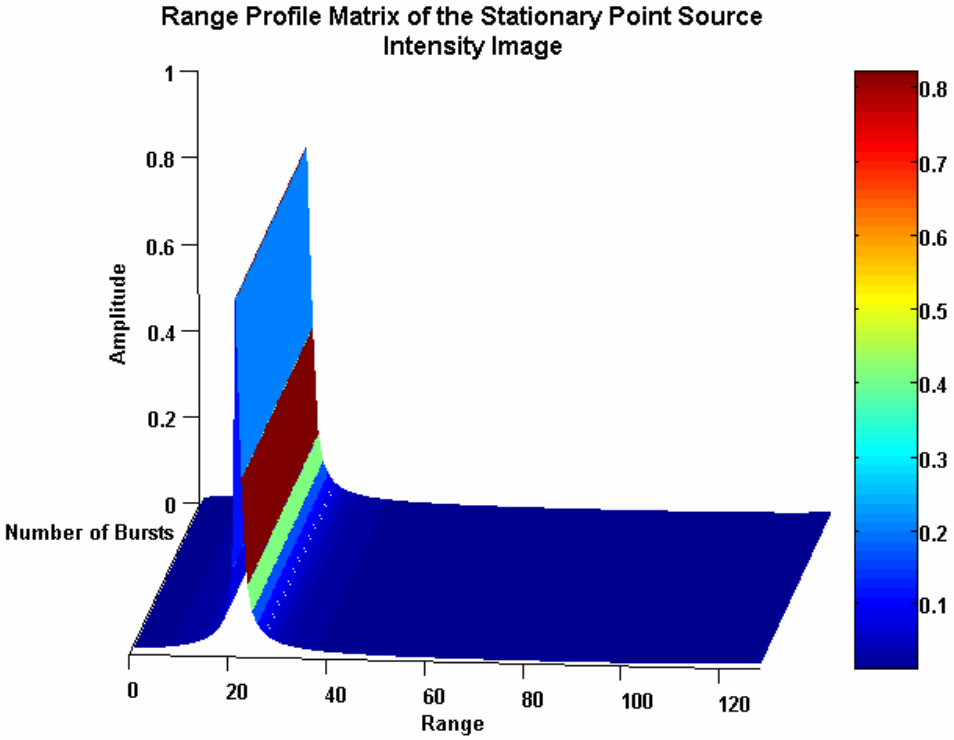

(a)

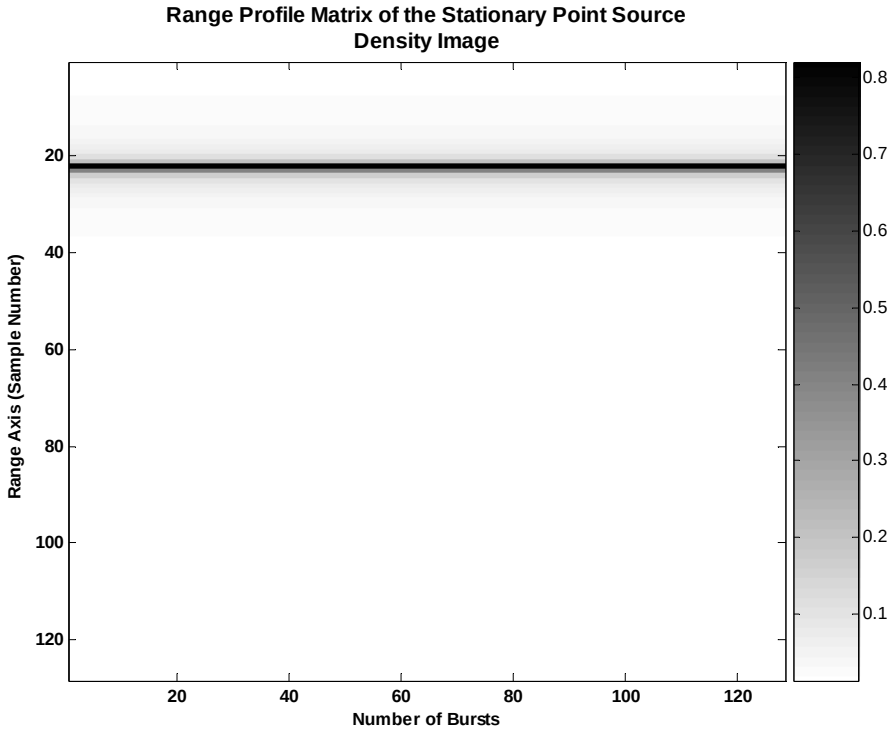

(b)

Figure 3.15 **Magnitudes of the range profile matrix images: (a) intensity image (b) density image**

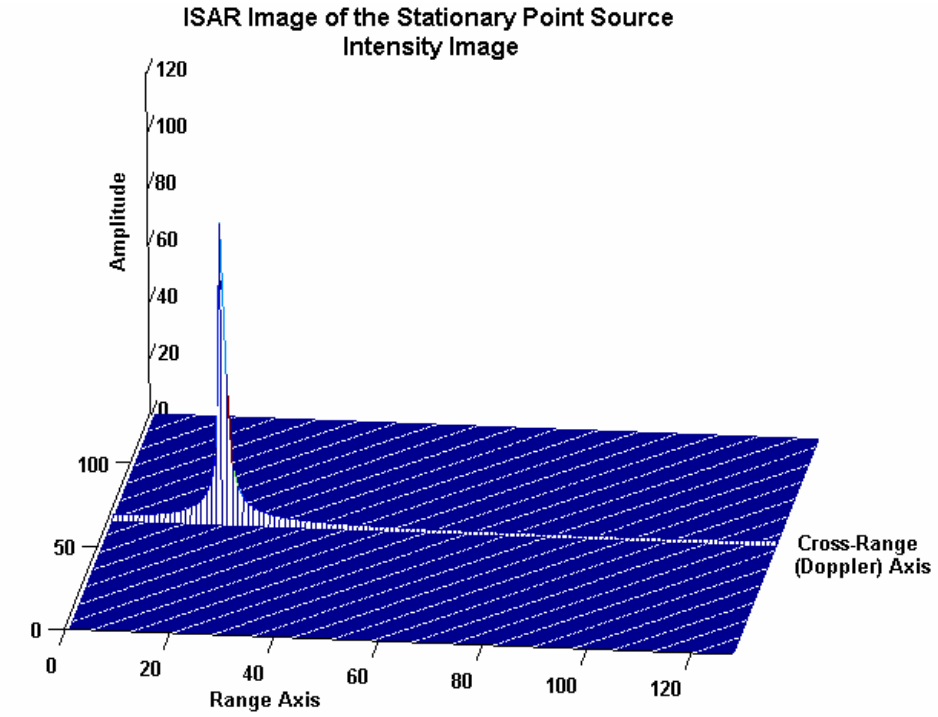

(a)

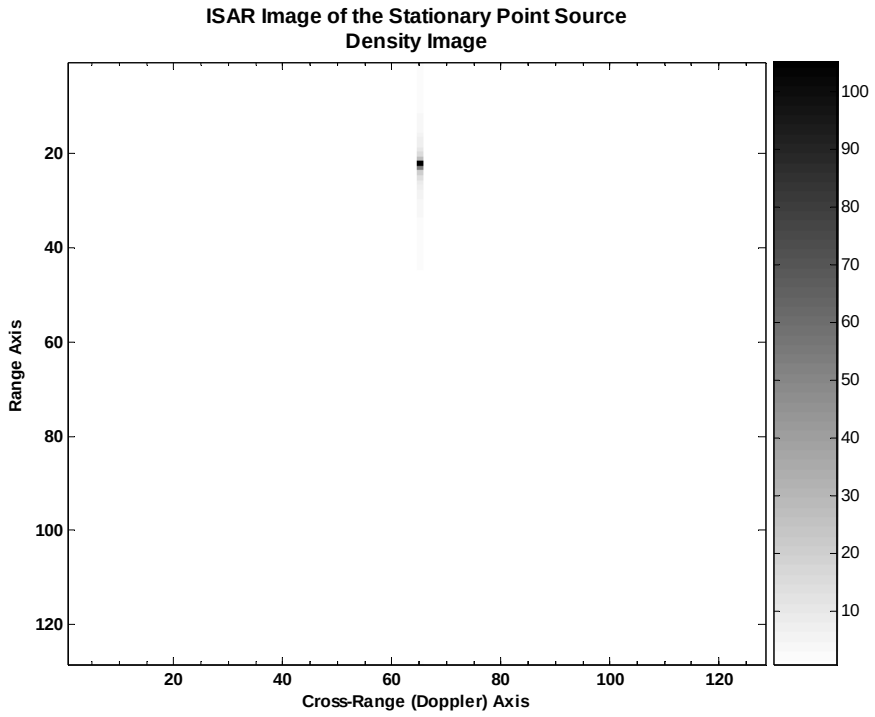

(b)

Figure 3.16 ISAR Images of the stationary point source: (a) intensity ımage (b) density image

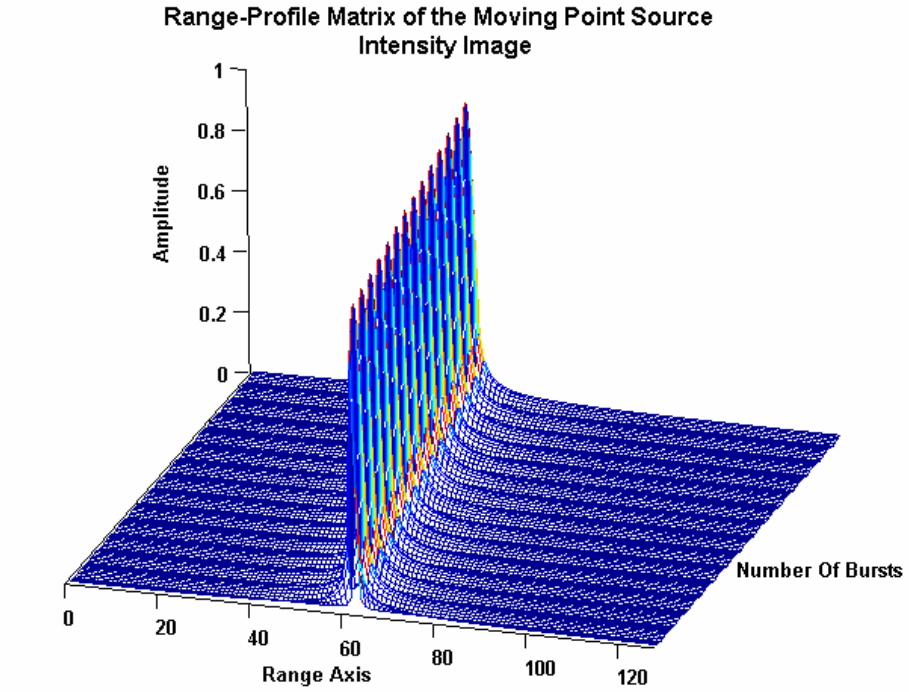

(a)

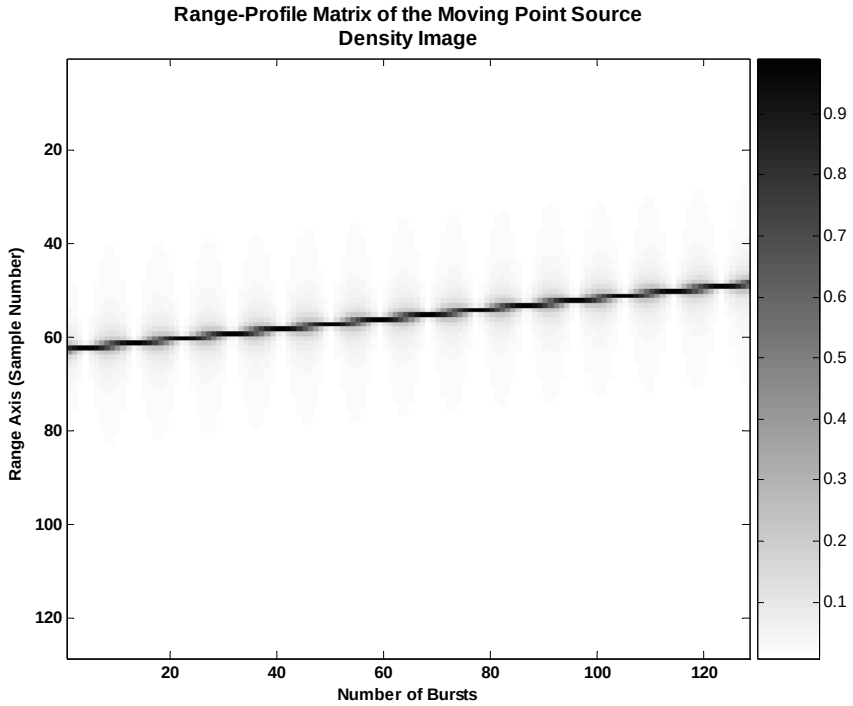

(b)

Figure 3.17 Magnitudes of the range profile matrix: (a) intensity image (b) density image. v_trans=20 m/sec.

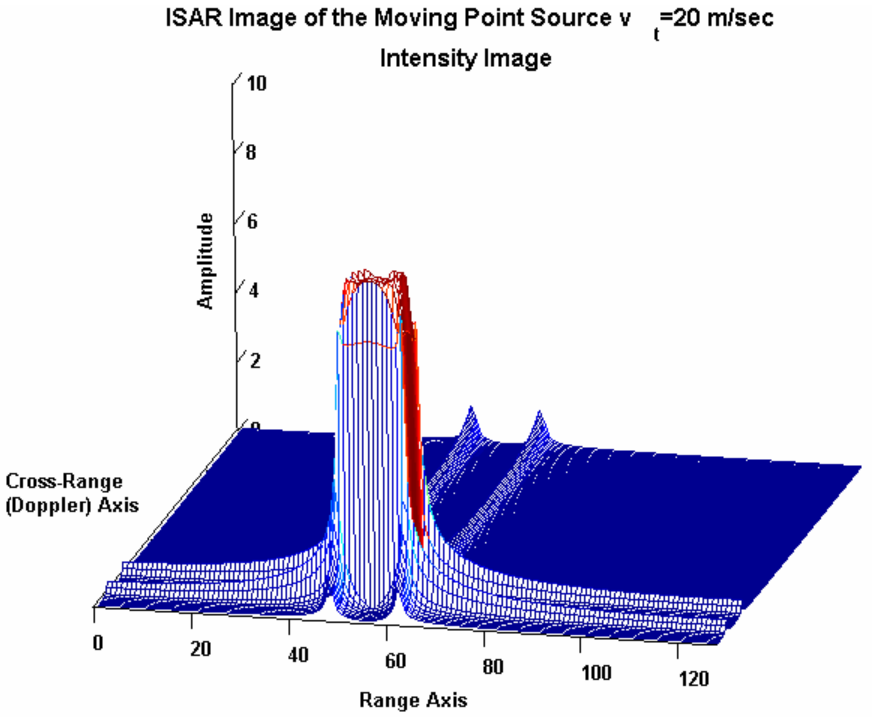

(a)

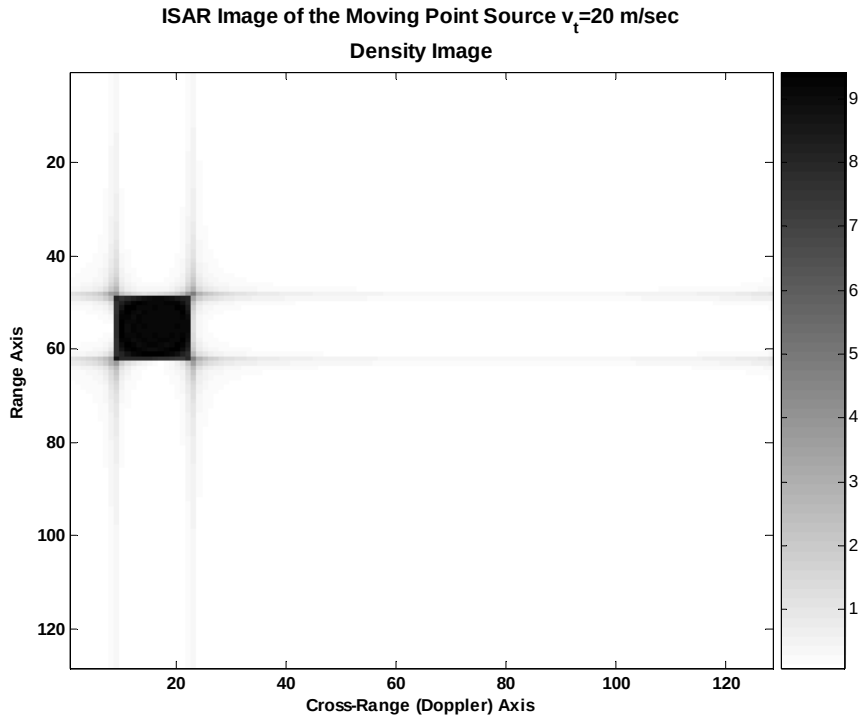

(b)

Figure 3.18 ISAR Images of the moving point source: (a) intensity image (b) density image. v_trans=20 m/sec.

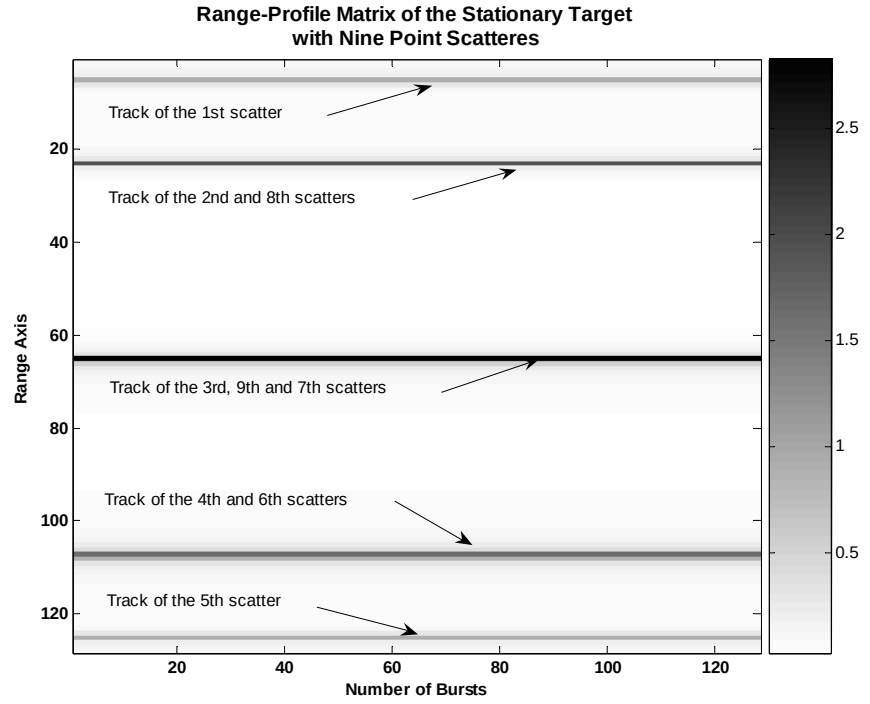

(a)

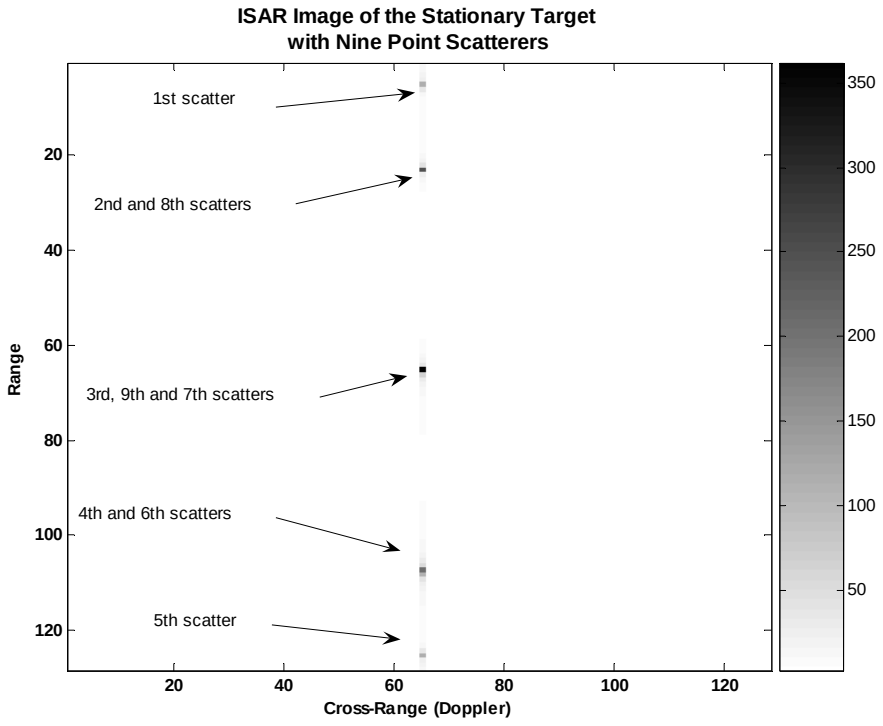

(b)

Figure 3.19 Range profiles and ISAR image of a Stationary Target

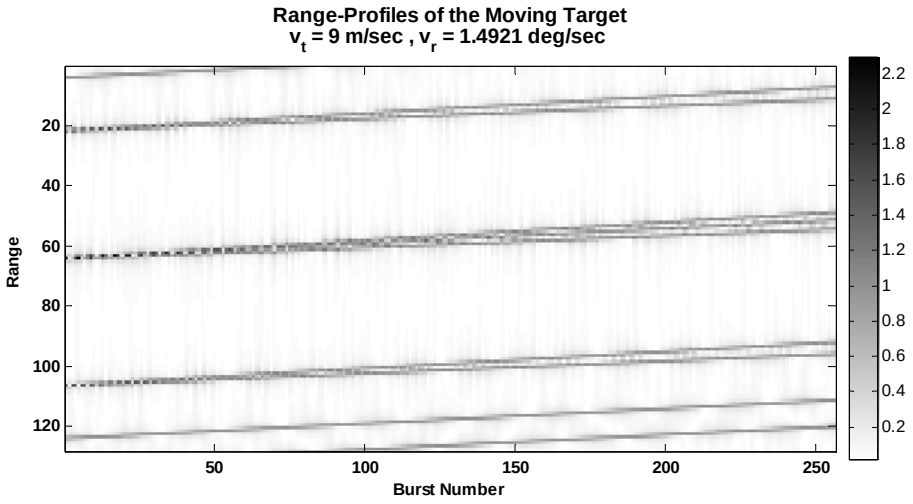

(a)

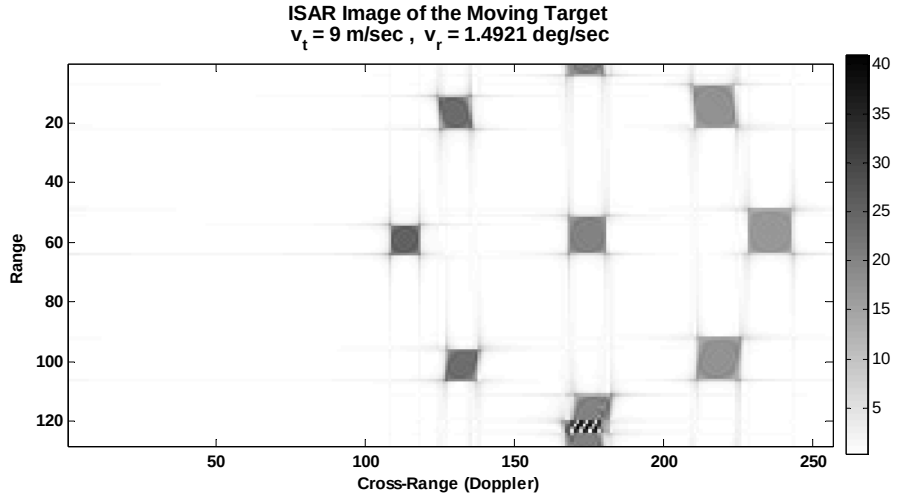

(b)

Figure 3.20 Range profiles and ISAR image of a Moving Target

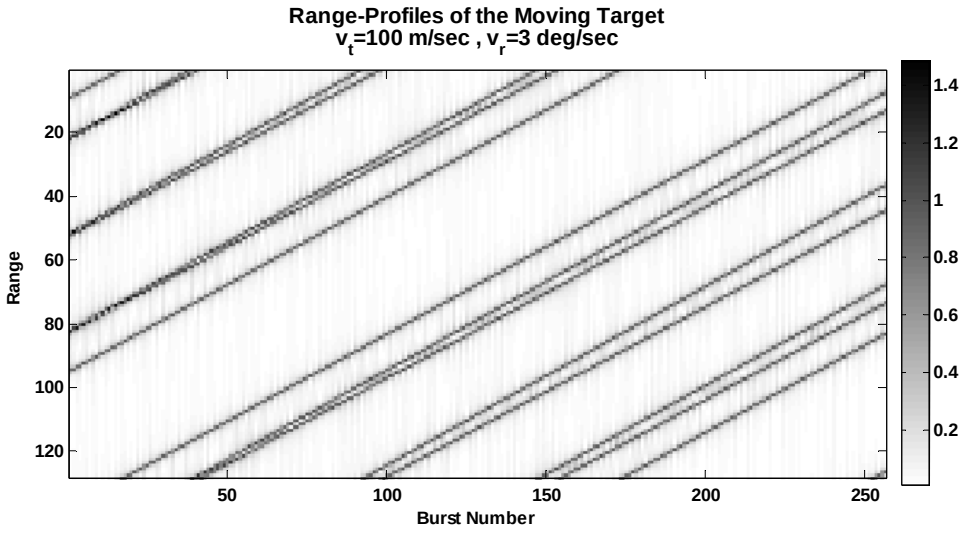

(a)

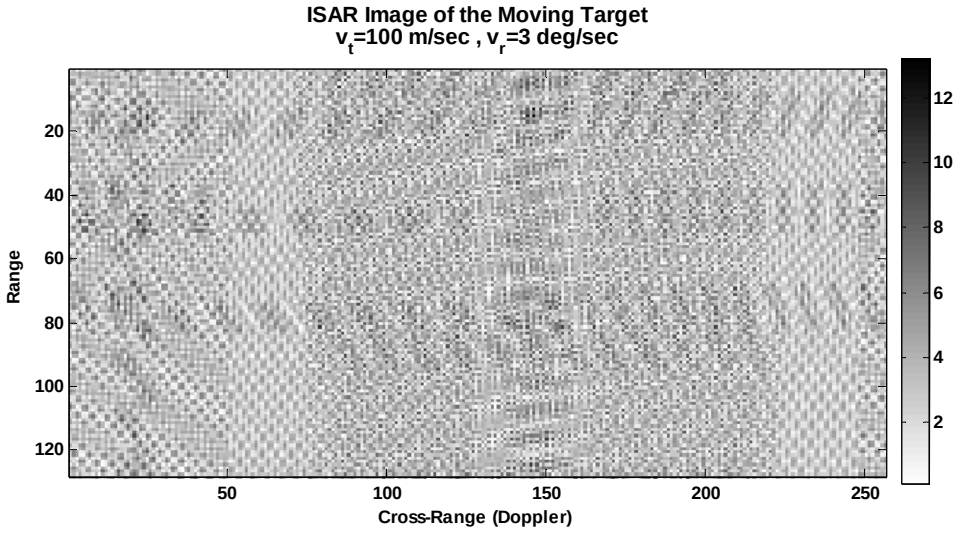

(b)

Figure 3.21 Range profiles and ISAR image of a FAST Moving Target

CHAPTER 4

APPLICATION OF THE JOINT TIME-FREQUENCY ANALYSIS TO ISAR IMAGE GENERATION

4.1 Introduction

In this chapter, a basic method of time-frequency transformation, Short Time Fourier Transform (STFT) is going to be explained in order to give an idea about the meaning, importance and functionality of the time-frequency transformations. Then, on this basis, an alternative method of ISAR image generation; Time-Frequency Transformation Method is going to be introduced and some examples of its usage in ISAR imaging are going to be demonstrated.

The aim of this chapter is to introduce the application of the Joint Time-Frequency Transformation (JTFT) technique to the ISAR image generation, not to find an optimum way or the best way to produce an ISAR image. Hence, advanced JTFT techniques are omitted and only STFT is examined.

JTFT concept is also applicable in motion compensation subjects which are going to be discussed in the following chapters. This chapter would be the basis of these future discussions.

4.2 Joint Time-Frequency Transforms

As it is well known, basic Fourier Transformation (FT) process characterize the frequency content of a time domain signal. But it does not give any idea about the time-dependent characteristics of this frequency content. JTFT is used in order to cover this deficiency. It becomes possible to analyze and characterize the time-varying frequency content of a signal, by the way of JTFT analysis [11].

Actually, JTFT is the name of the concept and there are various analysis techniques which could be used to characterize the time frequency content of the signals: Short-Time Fourier Transform (STFT), Continuous Wavelet Transform (CWT), Adaptive Time-Frequency Representation, Wigner-Ville Distribution, Cohen's Class and the Time-Frequency Distribution Series (TFDS) are the most important ones.

4.2.1 The Short-Time Fourier Transform

As the name implies, STFT method splits the time domain signal into many short time-segments and then uses standard FT to characterize the frequency content of the time-domain signal. This splitting process is done by a multiplication of the investigated signal, $s(t)$, with a moving time-window, $w(t)$. Figure 4.1 illustrates the logic of this process.

Mathematical representation of the STFT operation could be represented as,

$$S_{STFT}(t,\omega) = \int s(\tau)w(\tau - t)\exp(-j\omega\tau)d\tau \qquad (4.1)$$

Both of the investigated signal and the obtained STFT transform might be real or complex. Hence, the magnitude display of the STFT signal, $\left|S_{STFT}(t,\omega)\right|$, is called the ***spectrogram*** of the signal. Spectrograms are two-dimensional functions and they show how the frequency spectrum of the signal varies as a function of time.

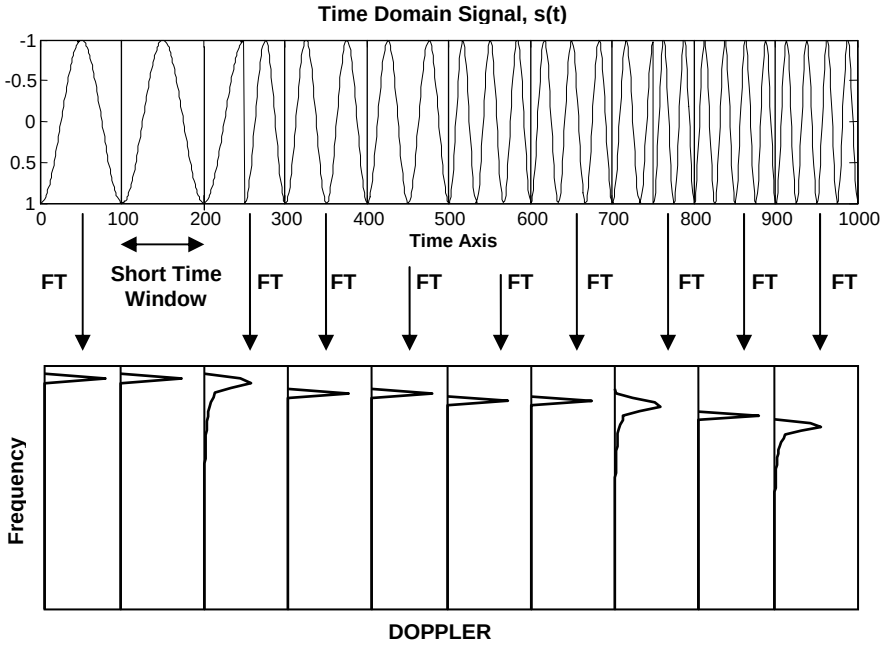

Figure 4.1 Illustration of the STFT

There are two important points about the STFT process:

1. Length of the window function,
2. Shape of the window function,

Length of the window function determines both the time and the frequency resolution limits. Shorter time window means good resolution in time but poor resolution in frequency. Similarly, poor resolution in time (longer window) means good resolution in time.

Main advantage of the STFT is, any signal components with durations shorter than the duration of the time window tend to get smeared out [11]. But, this windowing procedure also becomes main drawback of the STFT, since it is being a restriction on the frequency resolution. Because of this restriction, some other form of JTFT techniques are derived and widely used, such as Adaptive Time-Frequency Representation, which requires much more computational complexity but offers

same resolution as the ordinary FT. These kinds of advanced TF analysis method are also called ***High-Resolution Time-Frequency Transforms***.

Shape of the window function affects the level of the side-lobes in the frequency domain. Hence, in order to cut-down sidelobe interference in the spectrogram the window function should taper to zero smoothly.

An example STFT results are shown in Figure 4.2. Figure 4.2(a) represents the original time-domain signal, $s(t)$. It contains five nonoverlapping finite duration sinusoids, which could be defined as,

$$s(t) = \cos(2\pi f_1 t)w_1 + \cos(2\pi f_2 t)w_2 + \cos(2\pi f_3 t)w_3 + \cos(2\pi f_4 t)w_4 + \cos(2\pi f_5 t)w_5 \quad (4.2)$$

where w_1, w_2, w_3, w_4 and w_5 are non-overlapping finite duration rectangular window functions.

Figure 4.2(b) represents FT of the signal. Figure 4.2(c) and (d) are the STFT spectrograms generated using a Rectangular window of 100 and 200 points respectively. Figure 4.2(e) and (f) are the STFT spectrograms generated using a Gaussian window of 100 and 200 points respectively.

Effect of the length of the window function on the resultant spectrograms could be observed in Figure 4.2(c) and (d). Figure 4.2(d) has better frequency localization (thinner frequency steps) but worse time localization (longer and cloudy frequency-step transitions).

Effect of the window function on the spectrograms could be observed by a comparison of Figure 4.2(d) and (f). Figure 4.2(f) includes much less side-lobes than Figure 4.2(d), which is a superiority of Gaussian window function to the Rectangular window in the manner of side-lobe reduction.

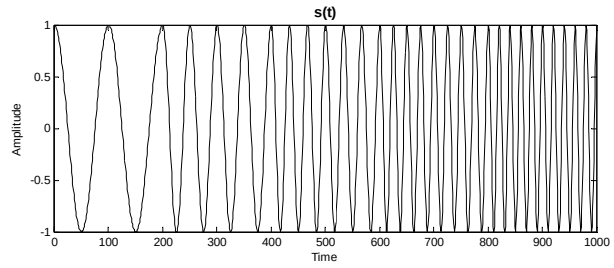

(a)

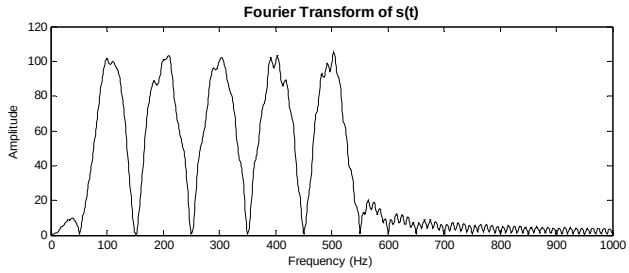

(b)

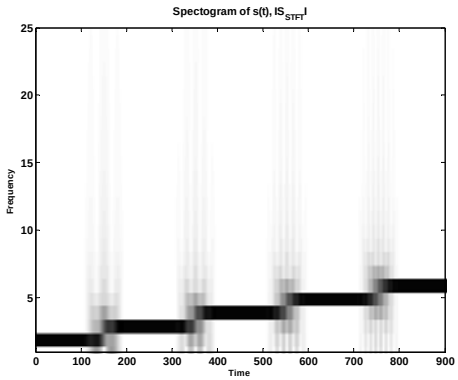

(c)

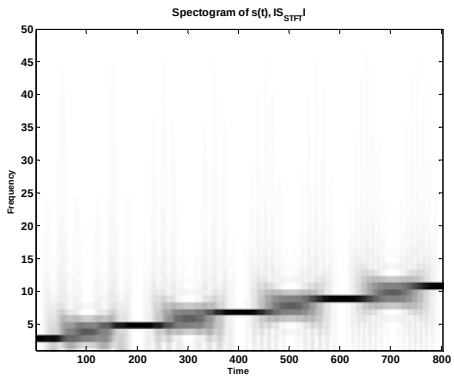

(d)

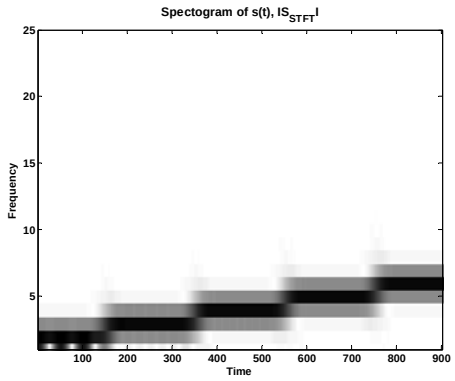

(e)

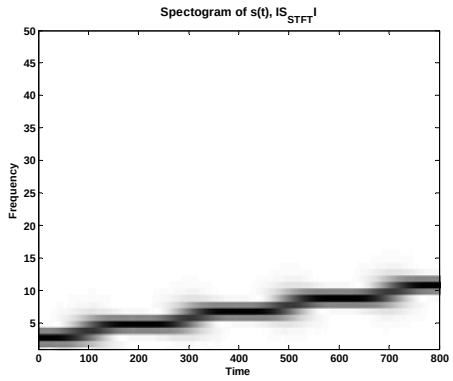

(f)

Figure 4.2 An Example of STFT

4.3 Time-Frequency Based ISAR Image Generation

Conventional and Time-Frequency Based imaging systems are differ from each other by the method of the synthetic aperture generation. As it was discussed in the Chapter 3.3, Fourier-based Conventional imaging systems use basic DFT process in order o generate cross-range profiles. In the case of time-frequency based image formation, this DFT process is replace by a time-frequency transformation.

Figure 4.3 illustrates the radar imaging system based on the time-frequency transformation (related data is obtained from [12]). At the initial step, it is assumed to have M range profiles, each having N range-cells. This complex range-profile matrix is going to be denoted as $RP(r_{n,m})$ from now on.

Fourier based image formation process generates only one image frame of $N \times M$ dimensions:

$$I(r_n, f_m) = DFT_m\left\{RP(r_{m,n})\right\} \tag{4.3}$$

Time-frequency-based image formation takes time-frequency transforms along the each of N range-cells, and generates time-frequency (time-Doppler or spectrogram definition are also applicable) distributions of $k \times l$ dimensions. Here, k and l represents the length of the time and the frequency axis respectively.

Dimensions of the resultant time-Doppler distribution, k and l, depends to the applied JTFT method. For example, if STFT is used with a time-window of W extent and $(W-1)$ overlaps per FT (which does mean one element shift of time-window for each FT process), resultant dimensions of the spectrogram would be $W \times (M - W + 1)$. But the dimensions would be $M \times M$, if any kind of high-resolution JTFT is used, in order to generate the time-Doppler distributions.

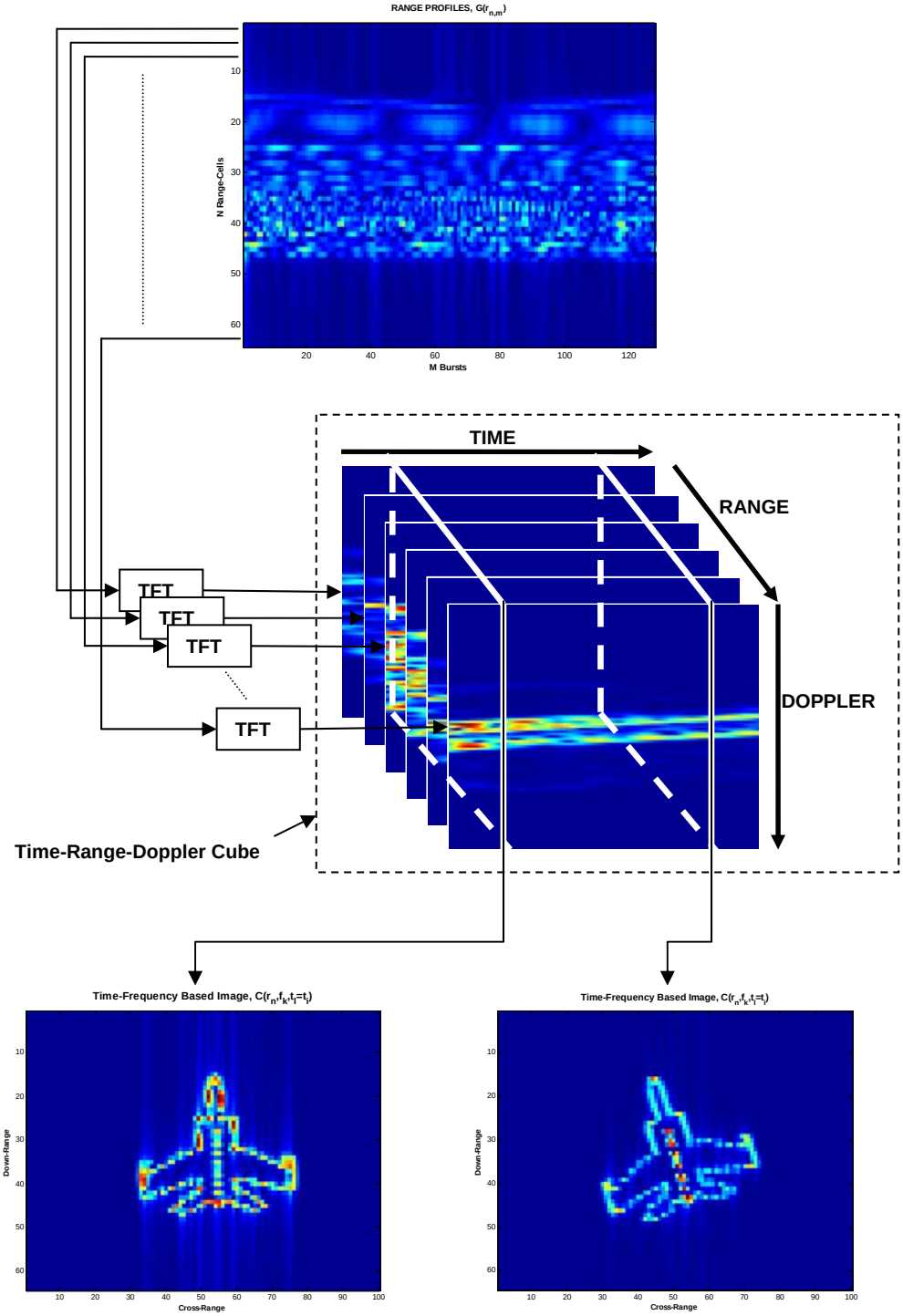

Figure 4.3 Time-Frequency based ISAR image formation

Time-Range-Doppler Cube

Hence, N number of time-Doppler distributions, each having $k \times l$ dimensions, would produce a *range-Doppler-time* cube, $C(r_n, f_k, t_l)$, of $N \times k \times l$ dimensions, which could be denoted as,

$$C(r_n, f_k, t_l) = TFT_m \left\{ G(r_{n,m}) \right\} \tag{4.4}$$

where TFT_m denotes the time-frequency transform with respect to the variable m.

Because the time-frequency transform can calculate the instantaneous Doppler frequency shift, at any instant the Doppler frequency shift of each scatterer on a target becomes a fixed value with its Doppler resolution determined by the selected time-frequency transform. At a sampling time t_i, only one range and instantaneous Doppler image frame $C(r_n, f_k, t_l = t_i)$ can be extracted from the $N \times k \times l$ range-Doppler-time cube. There are a total of l image frames available.[11]. Two sample image-slices are illustrated at the bottom of the Figure 4.3.

It is not usually necessary to take the maximal l time-samples because the Doppler variation from one sample to the next is not significant. In many cases, 16 or 32 equally spaced time-samples may be good enough to show the detailed Doppler variations [11].

4.4 A Short Comparison of Conventional and TF Based ISAR Image Generation

Many of the targets exhibits complicated motions in the coherent Integration Time. This means fluctuation of the Doppler shifts along the range profiles. This fluctuations decrease the image quality by the way of blurring. Basic DFT operation is insufficient to parse these kinds of time-dependent Doppler variations. Main advantage of the JTFT appears at this point. Especially, if a high-resolution JTFT

technique is occupied in order to generate an ISAR image, then same cross-range resolution could be obtained as it was in DFT process. The plus is Doppler wise stabilized images, without applying any complicated motion compensation algorithms.

Main disadvantage of the JTFT is the extra signal processing: in any type of JTFT, an optimization for the time-window, with respect to the length and standard deviation is required.

4.5 Some Examples of TF Based ISAR Images

In this section, four comparative examples of TF-based and Conventional ISAR images are going to be introduced and illustrated.

STFT method is used in order to construct the TF-based images. Hence, advanced resolution examinations are omitted.

Other important point is the induced translational motions in Simulation-2 and Simulation-3. They are much smaller than the realistic values. Since the motion compensation concept is not introduced yet, those kinds of small values have to be used, in order to construct acceptable (clear and understandable) ISAR images. The last simulation example, Simulation-4, is included in order to express this important point; necessity of the translational motion and its compensation.

Simulation-1

First example is simulated Mig-25 target. The data of this simulation is used with the permission of Dr. V.C. Chen [12]. The target was assumed to have only a rotational motion. Related simulation parameters and illustrations are given in Table 4.1 and Figure 4.6 respectively. Figure 4.6(a) represents conventional Fourier-based image. Blurring effect of the target's rotational motion could be observed on this image. The target is looking like turning around itself on the axis located on its tail. Figure 4.6(b) includes nine equally-spaced range-Doppler slices from the range-Doppler-time

cube. As it is expected, much more clear ISAR images are handled by the way of TF imaging. The cost is extra signal processing and lower Doppler resolution.

Simulation-2

Second example is a cross-shaped target. The target is constructed as a collection of fifteen point sources. These scatterers are assumed to locate on a rigid body. Simulation model is explained in Figure 4.4, by the way of point sources' planar distributions. Related parameters are listed in Table 4.2. Figure 4.7 illustrates resultant Conventional and TF-based ISAR images.

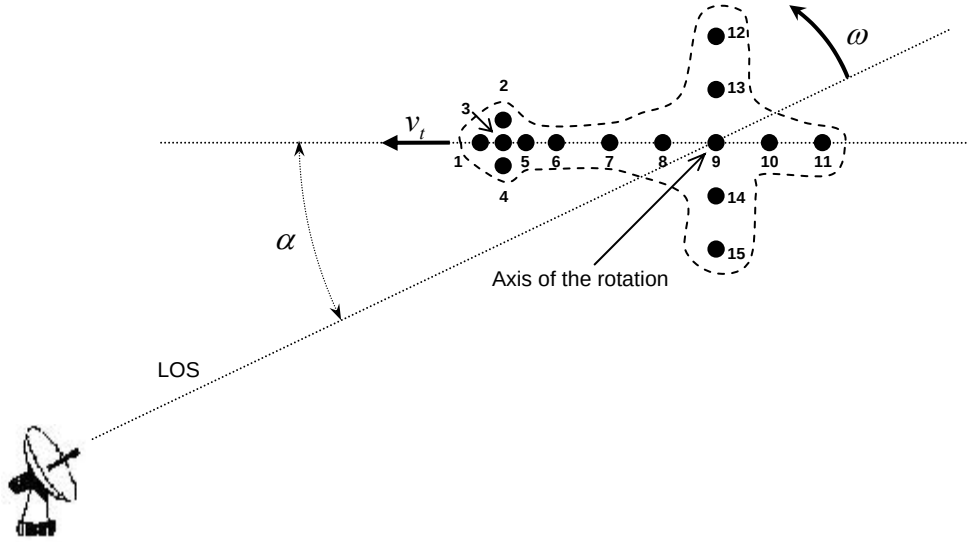

Figure 4.4 Illustration of Simulation Model-2

According to the simulation scenario, target exhibits both translational and rotational motions; v_t and ω. Translational motion is towards the radar with an offset angle, α.

First, second, third, fourth and fifth point sources (first five points) play an important role in this simulation. As it could be seen from Figure 4.7(a), Conventional image

quality is spoiled according to the motion of the target. First five points are no more distinguishable because of the targets both translational and rotational motions. Figure 4.7(b) proves that TF-based image slices are much clearer and closer points are much more resolvable.

Simulation-3

Third simulation model is the circle of scatterers. The target is constructed as a collection of twenty five point sources. Point sources are distributed on a hypothetical circle and grouped three-by-three. One extra point scatterer is located at the middle of the circle. These scatterers are assumed to locate on a rigid body. Simulation model is explained in Figure 4.5, by the way of point sources' planar distributions. Translational motion of the target is discarded in this example; hence it is equal to zero. This point is important, because it is going to give some important ideas about the TF-based imaging and its usage. Related parameters are listed in Table 4.3. Figure 4.8 illustrates resultant Conventional and TF-based ISAR images.

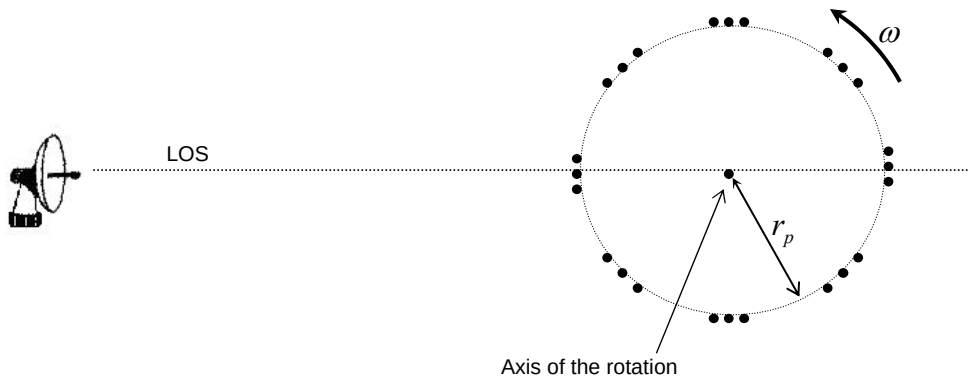

Figure 4.5 Illustration of Simulation Model-3

Figure 4.8(a) shows that, as a result of rotational motion of the target, individual point sources of the scatterer groups are no more distinguishable and no more

resolvable. Hence, conventional Fourier-based image looks like a blurred image of total number of nine scatterers. Effect of the rotational motion is very well handled and overcame by the way of TF-based imaging technique. TF-based six image slices are shown in Figure 4.8(b). Scatterer-trios are resolvable in spite of the reduced Doppler Resolution, which is a natural result of STFT. This means that, if the case is rotational motion; TF-based image generation is an applicable method of motion compensation; without applying any complicated rotational motion compensation.

Simulation-4

Simulation model and related parameters are all same with the Simulation-3. The only difference is the additional translational motion of 200 m/sec, which does look like much more realistic value. Fourier-based and TF-based images are illustrated in Figure 4.9. Only one sample image slice is included in this figure, for TF-based imaging. It could be said that, TF-based ISAR imaging and its advantages about rotational motion elimination does mean nothing, without proper translational motion compensation.

Table 4.1 Parameters of Simulation-1

Parameter Description	***Value***
Rotational Velocity, ω *, (degrees/sec)*	Compensated
Translational velocity, v_t *, (m/sec)*	Unknown
Δf , frequency-step size, MHz	1
f_0, starting frequency, GHz	9
N , The number of discrete pulses per burst	64
M , The number of bursts	512
β , The effective bandwidth of a burst, MHz	512
T_P , The pulse width, μsec	Unknown
T_{PRI} , The pulse repetition interval (PRI), μsec	66
T, Coherent Integration Time, seconds	2.18
STFT Window Type	Gaussian
STFT Window Length, W	100
Conventional Image Dimensions, NxM	64x512
TF-Based Image Dimensions, NxW	64x100

Table 4.2 Parameters of Simulation-2

Parameter Description	***Value***
Rotational Velocity, ω *, (degrees/sec)*	6
Translational velocity, v_t *, (m/sec)*	17
Translational Motion Angle with respect to the LOS, α *, degrees*	45
Δf , frequency-step size, MHz	1.025
f_0, starting frequency, GHz	3
N , The number of discrete pulses per burst	128
M , The number of bursts	256
β , The effective bandwidth of a burst, MHz	131.2
T_P , The pulse width, μsec	5
T_{PRI} , The pulse repetition interval (PRI), μsec	50
T, Coherent Integration Time, seconds	1.64
STFT Window Type	Gaussian
STFT Window Length	80
Conventional Image Dimensions, NxM	128x256
TF-Based Image Dimensions, NxW	128x80

Table 4.3 Parameters of Simulation-3

Parameter Description	***Value***
Rotational Velocity, ω *, (degrees/sec)*	4
Translational velocity, v_t *, (m/sec)*	0
Δf , frequency-step size, MHz	1
f_0 , starting frequency, GHz	3
N , The number of discrete pulses per burst	128
M , The number of bursts	256
β , The effective bandwidth of a burst, MHz	128
T_P , The pulse width, μsec	10
T_{PRI} , The pulse repetition interval (PRI), μsec	50
T, Coherent Integration Time, seconds	1.64
STFT Window Type	Gaussian
STFT Window Length	80
Conventional Image Dimensions, NxM	128x256
TF-Based Image Dimensions, NxW	128x80

(a) FT-Based Conventional Image

First Time Slice

Second Time Slice

Third Time Slice

Fourth Time Slice

Fifth Time Slice

Sixth Time Slice

Seventh Time Slice

Eighth Time Slice

Ninth Time Slice

(b) TFT-Based Image Slices

Figure 4.6 Simulation-1: Mig-25

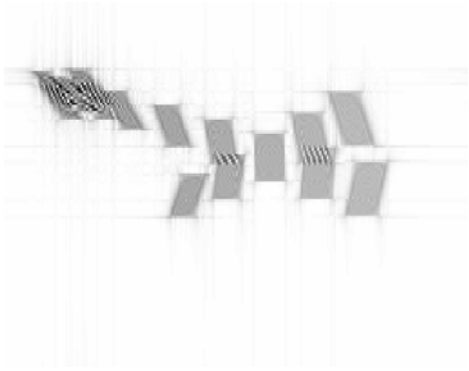

(a) FT-Based Conventional Image

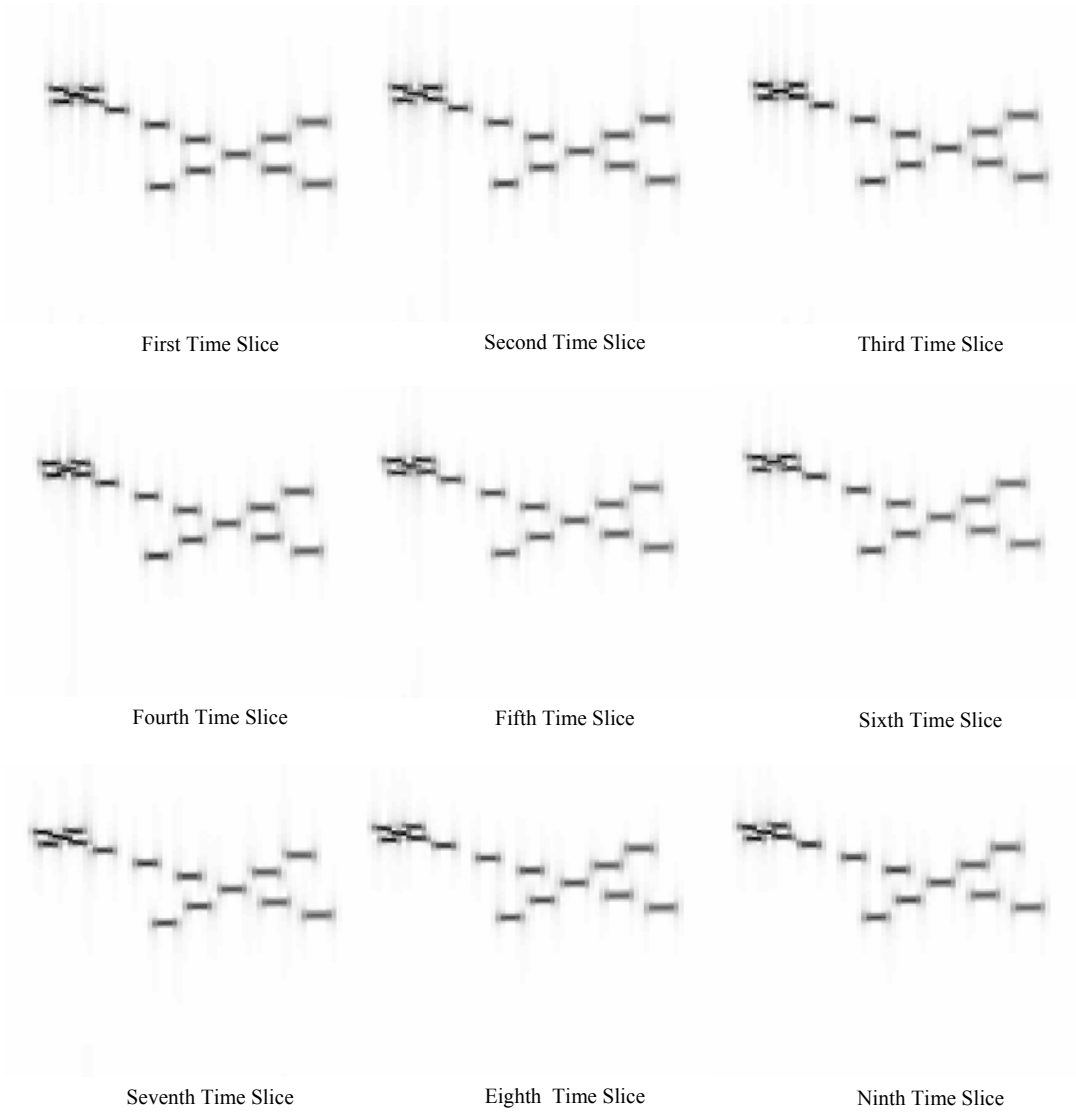

(b) TFT-Based Image Slices

Figure 4.7 Simulation-2: Cross-Shaped object

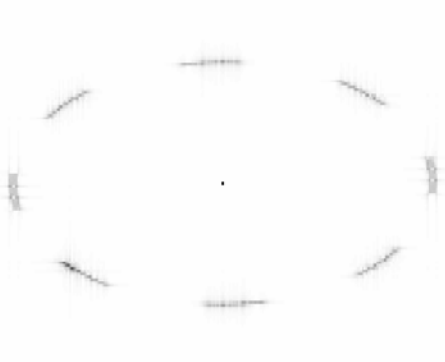

(a) FT-Based Conventional Image

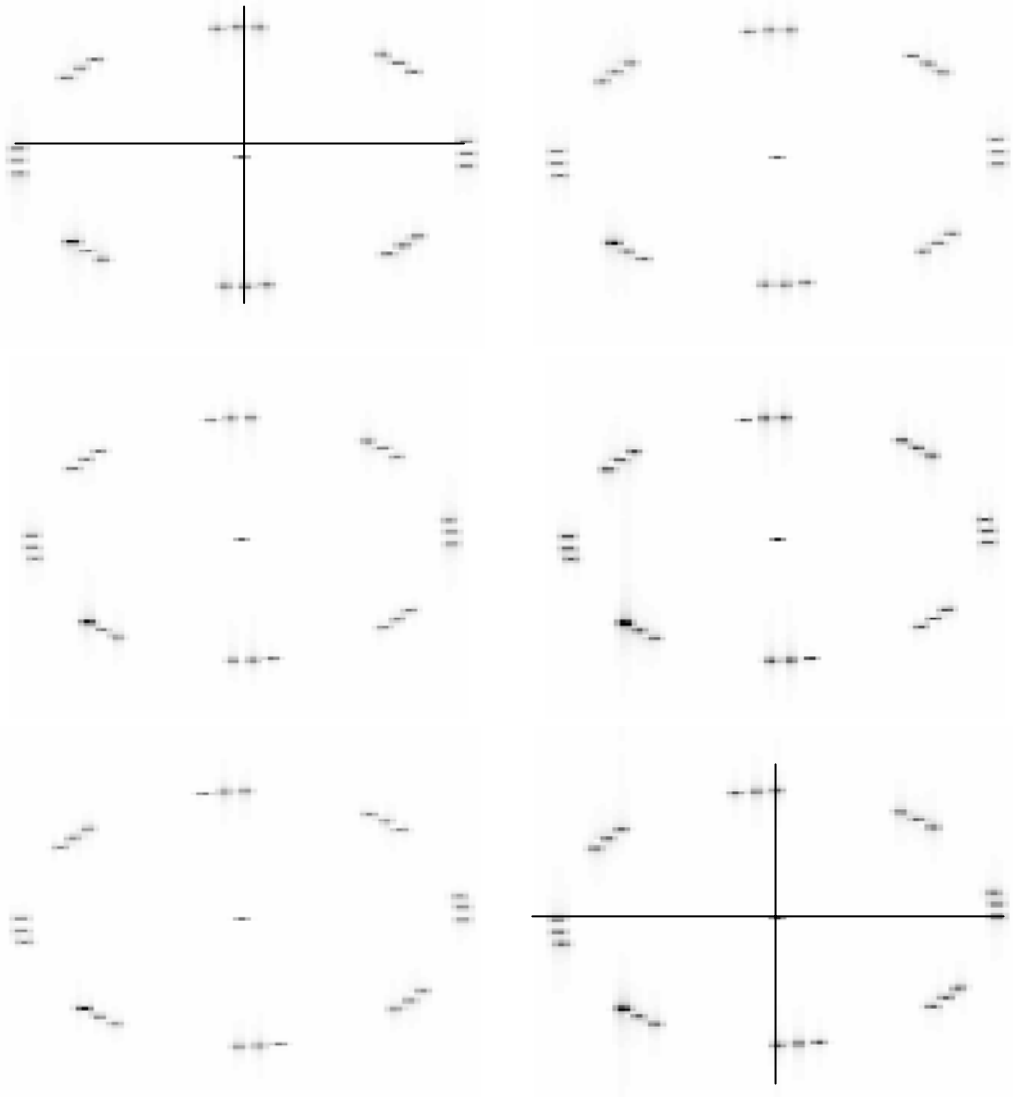

(b) TFT-Based Image Slices

Figure 4.8 Simulation-3: Circle-Shaped object, zero translational velocity

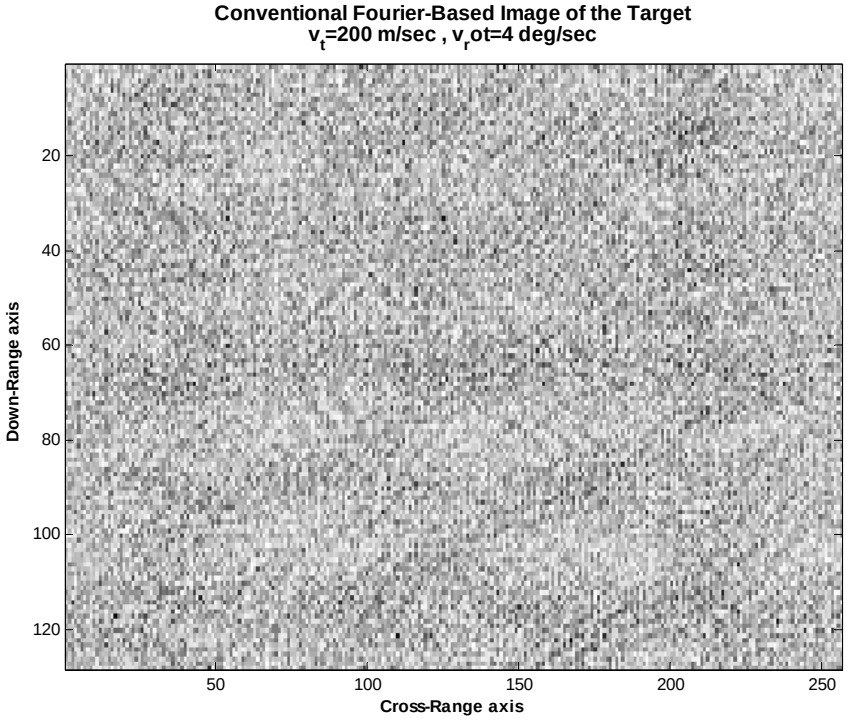

(a) FFT-Based conventional ISAR image

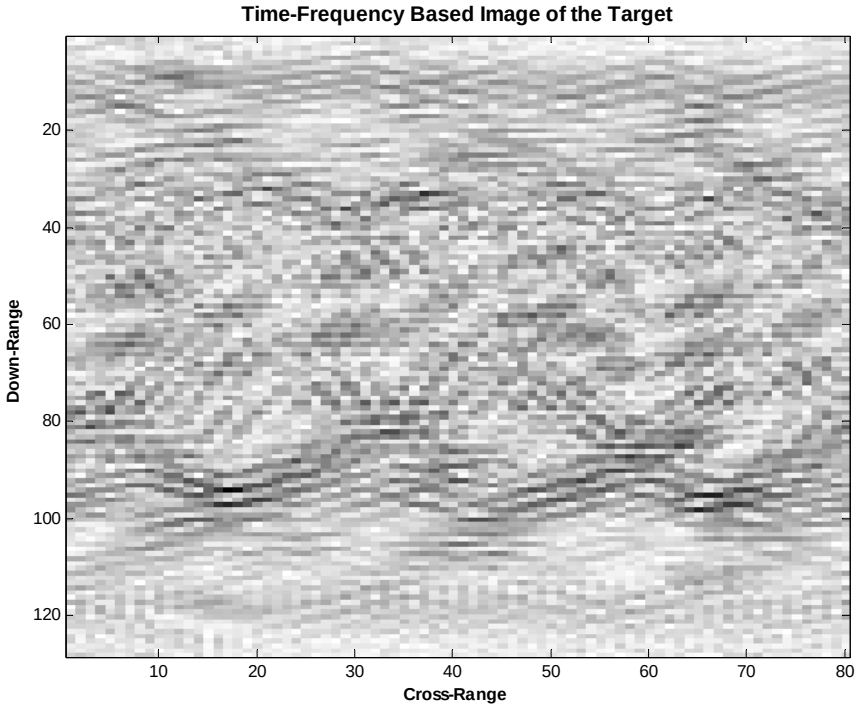

(b) TFT-Based ISAR image, one sample slice

Figure 4.9 Simulation-4: Circle-Shaped object, v_rot=200 m/sec

CHAPTER 5

MOTION COMPENSATION

5.1 Introduction

The goal of motion compensation is to estimate and correct for any unknown and undesired target motion, in order to suggest a solution to the blurring of the target image. But it is a little bit complicated process. The main difficulty is that the ISAR processing is a blind process. Hence, nobody knows any about the parameters of the motion of the target. That is why, motion compensation algorithms only suggest some optimal solutions, but they could not always be successful.

Motion compensation phenomenon and researches was burn at the same time with the ISAR imaging activities, early in 80's [2,9,13]. Research into motion compensation algorithms is still an ongoing activity [11].

Researchers were only dealt with translational motion compensation in the early times [9]. Then, extending technological opportunities and fast processors let them to look for much and some kind of rotational motion compensation algorithms was suggested.

In this chapter, effects of the target's rotational and translational motions on the ISAR image generation process are going to be discussed deeply. These discussions are going to be connected to the need of the motion compensation. Then, basic scheme of the motion compensation is illustrated. Translational and rotational motion compensation steps are explained with the main lines.

5.2 Effects of Targets Translational and Rotation Motions in ISAR Imaging

In Chapter 2, the total echo phase advance of a point-scatterer, seen from transmission to reception for i[th] pulse was given in Equation (2.14) as,

$$\psi_0(t) = -2\pi f_0\left(\frac{2R}{c} - \frac{2v_t t}{c}\right) \tag{5.1}$$

where v_t is referring to the translational velocity of the point-scatterer, f_0 is the frequency of the transmitted pulse, and c is the speed of the light. The equation could be rewritten as,

$$\psi_0(t) = -2\pi f_0 \frac{2R_p(t)}{c} \tag{5.2}$$

where, $R_p(t)$ is the instantaneous range of the target.

Let us define a target geometry as illustrated in Figure 5.1 and let us locate this point shaped scatterer, *P*, on to this target [11].

Let us assume that the target is stationary for the initial range analysis. At time $t = 0$, the target range *is R.* Hence, the distance from the radar to the point-scatterer *P*, R_p, could be rewritten as,

$$\begin{aligned} R_p &= \left[(T_x + x\cos\theta_0 - y\sin\theta_0)^2 + (T_y + y\cos\theta_0 + x\sin\theta_0)^2\right]^{1/2} \\ &= \left\{R^2 + (x^2 + y^2) + 2R\left[x\cos(\theta_0 - \alpha) - y\sin(\theta_0 - \alpha)\right]\right\}^{1/2} \\ &\cong R + x\cos(\theta_0 - \alpha) - y\sin(\theta_0 - \alpha) \end{aligned} \tag{5.3}$$

where $(T_x, T_{y,} T_z = 0)$ is the translation of the origin of the *(x, y, z)* coordinates with respect to the radar *(U, V, W)* coordinates, α is the azimuth angle of the target with respect to the *(U, V, W)* coordinates, and θ_0 is the initial rotation angle of the *(x, y, z)*

coordinates about the *Z*-axis in the *(X, Y, Z),* coordinates as illustrated in Figure 5.1 [11].

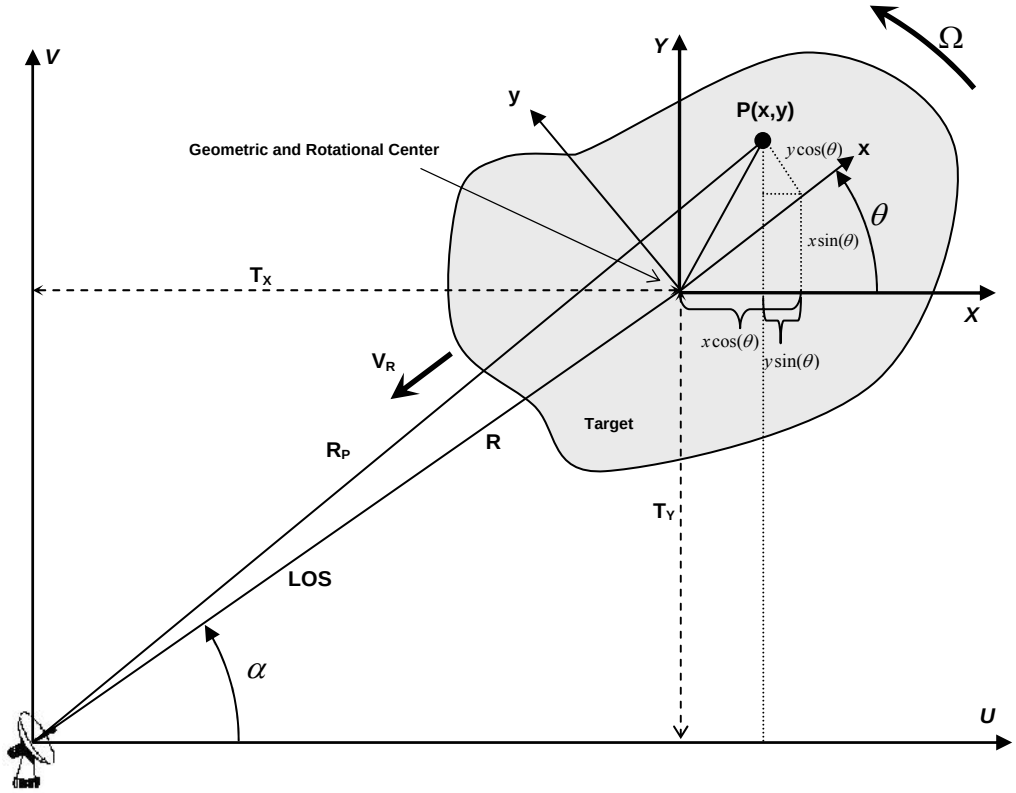

Figure 5.1 Illustration of the moving target geometry

Now, let us assume that the target exhibits a complicated motion, which is a combination of translational and rotational motions. Related motion parameters could be represented as,

$$R(t) = R_0 + V_R t + \frac{1}{2} a_R t^2 + \ldots \tag{5.4}$$

and

$$\theta(t) = \theta_0 + \Omega t + \frac{1}{2} \gamma t^2 + \ldots \tag{5.5}$$

where, R_0 and θ_0 are the initial distance of the target center to the radar point and the offset rotational angle, respectively. The radial and the rotational velocities, accelerations, and higher order terms are included in Equation (5.4) and Equation (5.5).

Thus, in the light of the Equation (5.4) and (5.5), Equation (5.3) could be rewritten as,

$$R_p(t) = R(t) + x\cos[\theta(t) - \alpha] - y\sin[\theta(t) - \alpha] \tag{5.6}$$

Doppler frequency shift induced by the target's motion could be written by taking the time-derivative of the phase in Equation (5.2) as,

$$\begin{aligned} f_D &= \frac{2f_0}{c}\frac{d}{dt}R_p(t) \\ &= \frac{2f_0}{c}V_R + \frac{2f_0}{c}[-x\Omega\sin(\theta_0 + \Omega t - \alpha) - y\Omega\cos(\theta_0 + \Omega t - \alpha)] \\ &= \frac{2f_0}{c}V_R + \frac{2f_0}{c}\begin{Bmatrix} -x\Omega[\sin(\theta_0 - \alpha)\cos\Omega t + \cos(\theta_0 - \alpha)\sin\Omega t] \\ -y\Omega[\cos(\theta_0 - \alpha)\cos\Omega t - \sin(\theta_0 - \alpha)\sin\Omega t] \end{Bmatrix} \end{aligned} \tag{5.7}$$

where, only the zero and first-order terms in (5.4) and (5.5) are used. For a given rotation rate and coherent processing time T, if $\Omega^2 t^2 << 1$ and $\Omega^3 t^3 << \Omega t$, hence

$$\cos\Omega t = 1 - \Omega^2 t^2 / 2 + ... \cong 1$$

and

$$\sin\Omega t = \Omega t - \Omega^3 t^3 / 6 + ... \cong \Omega t$$

Thus, we have [11]

$$\begin{aligned} f_D &\cong \frac{2f_0}{c}V_R + \frac{2f_0}{c}\begin{Bmatrix} -x\Omega[\sin(\theta_0 - \alpha) + \cos(\theta_0 - \alpha)\Omega t] \\ -y\Omega[\cos(\theta_0 - \alpha) - \sin(\theta_0 - \alpha)\Omega t] \end{Bmatrix} \\ &= \frac{2f_0}{c}V_R + \frac{2f_0}{c}\begin{Bmatrix} -[x\sin(\theta_0 - \alpha) + y\cos(\theta_0 - \alpha)]\Omega \\ -[x\cos(\theta_0 - \alpha) - y\sin(\theta_0 - \alpha)]\Omega^2 t \end{Bmatrix} \\ &= f_{D_{Trans}} + f_{D_{Rot}} \end{aligned} \tag{5.8}$$

where, the Doppler frequency shift induced by the translational motion is

$$f_{D_{Trans}} = \frac{2f_0}{c} V_R \tag{5.9}$$

and that induced by the rotational motion is,

$$f_{D_{Rot}} = \frac{2f_0}{c} \begin{Bmatrix} -[x\sin(\theta_0 - \alpha) + y\cos(\theta_0 - \alpha)]\Omega \\ -[x\cos(\theta_0 - \alpha) - y\sin(\theta_0 - \alpha)]\Omega^2 t \end{Bmatrix} \tag{5.10}$$

Only the first term of the Equation (5.10) is needed for ISAR imaging; in order to generate synthetic aperture.

The translational Doppler frequency shift shown by Equation (5.9) is constant for all of the scatterers on the target and produce a uniform (not differential) Doppler shift. Hence, this motion does not contribute to the cross-range resolution and of course to the ISAR imaging [13]. Unfortunately, this kind of translational motion causes the ***range walk***, which was introduced in Chapter 3. Range walk is referred as ***range misalignment*** in many of the sources. Hence, assuming the target's translational motion parameters and removing the related phase component from the received signals phase is called the **translational motion compensation**. Radial motion compensation term could be used interchangeably.

The quadratic part of the rotational Doppler frequency shift, which is shown by the second term of the Equation (5.10), is a function of time. Therefore, it would need to be compensated depending to the strength of the angular rotation rate, Ω, even if the translational motion compensation is already done. This process is called **rotational motion compensation**.

The motion of the targets could be generalized as shown in Figure 5.2 [13]. Typical trajectory is shown by the dashed line between the A and B points. T represents the coherent integration time. A is the position of the target at the starting time, $t = 0$, of the image processing. B is the reached point of the target at the and of the Coherent

Integration time, $t = T$. Then, motion of the target could be decomposed in to three parts:

1. A circular motion of the target about the radar at a constant range; R,
2. A translational motion of the target along the LOS; s(t),
3. A Rotational motion about the reference point.

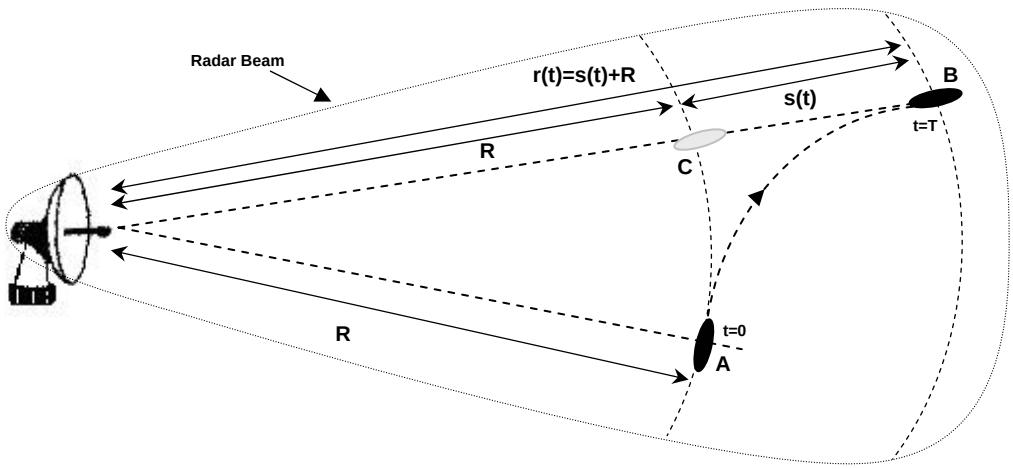

Figure 5.2 Target with general motion

The first component does not affect the imaging process. The second component; translational motion, is the reason of range walk and has to be compensated. Translational motion compensation removes the effect of the s(t) and target appears as it is located at C. The third component makes ISAR imaging possible. But if the total rotation of the target is high enough to make the scatterers of the target drift from one range-cell to the other, it has to be compensated by a proper method of the rotational motion compensation.

5.3 Translational Motion Compensation Steps

In order to obtain clear and sharp images, the following conditions must be satisfied during the coherent image processing time:

1. The scatterers on the target must remain in their range cells
2. Scatterers' Doppler frequency shifts must be constant.

If the scatterers drift out their range cells or their Doppler frequency; shifts are time varying, the Doppler spectrum obtained from the Fourier transform becomes smeared, and the radar image becomes blurred.

Figure 5.3 illustrates standard translational motion compensation steps. First step is the ***Range Tracking***. Range Tracking step includes re-alignment of the range profiles, in order to compensate the effect of range-walk. If a compensation algorithm only includes Range Tracking step, it is called ***coarse motion compensation***.

The coarse range alignment allows a point-scatterer to be sorted into the same range-cell across all the pulses. However, the accuracy of the alignment is limited by the range resolution, which is typically tens of centimeters. This is not sufficient to overcome the phase errors measured in terms of the radar operating wavelength, which is typically a few centimeters. Hence, in many cases, range tracking does not give sufficient results because of the time-varying characteristic of the Doppler shifts in one range-cell, as shown in Figure 5.3. Thus, ***fine motion compensation***, called Doppler Tracking, should be applied to make phase compensation and, hence, Doppler frequency shifts, constant. Doppler Tracking step includes correction and compensation of the phases along the range-cells [11].

As a summary of the translational motion compensation; Range Tracking keeps scatterers in their range cells; and Doppler Tracking makes Doppler frequency shifts to be constant as it was illustrated in Figure 5.3.

Therefore, referring to the Figure 5.2, after Range and Doppler tracking steps, the target appears to be moving from A to C, with only a rotational motion about a reference point. Actually, this reference point (axis of the rotation) might be on the target itself or any where at the space. In this thesis, simulations are based on as if the rotational axis is a point on the target.

5.4 Range Tracking Application

There are many of kind of range tracking techniques are suggested from 80's up to now. Some of them could be listed as,

- Cross-Correlation method [9,14],
- Prominent Point Processing [15],
- Target Centroid Tracking [16],

Range Tracking application and algorithm in this thesis is constructed according to [9], [14] and [6]. The main idea of the method is to find the amount of range misalignment by the way of cross correlation application.

5.4.1 Algorithm of the Range Tracking

Basic steps of the algorithm could be written according to the M number of complex RPs as,

1. One of the M complex RPs, is chosen arbitrarily, as a reference RP.
2. All other (M-1) RPs are cross-correlated with the reference RP. Only the magnitudes of the complex RPs are used in this cross-correlation process.

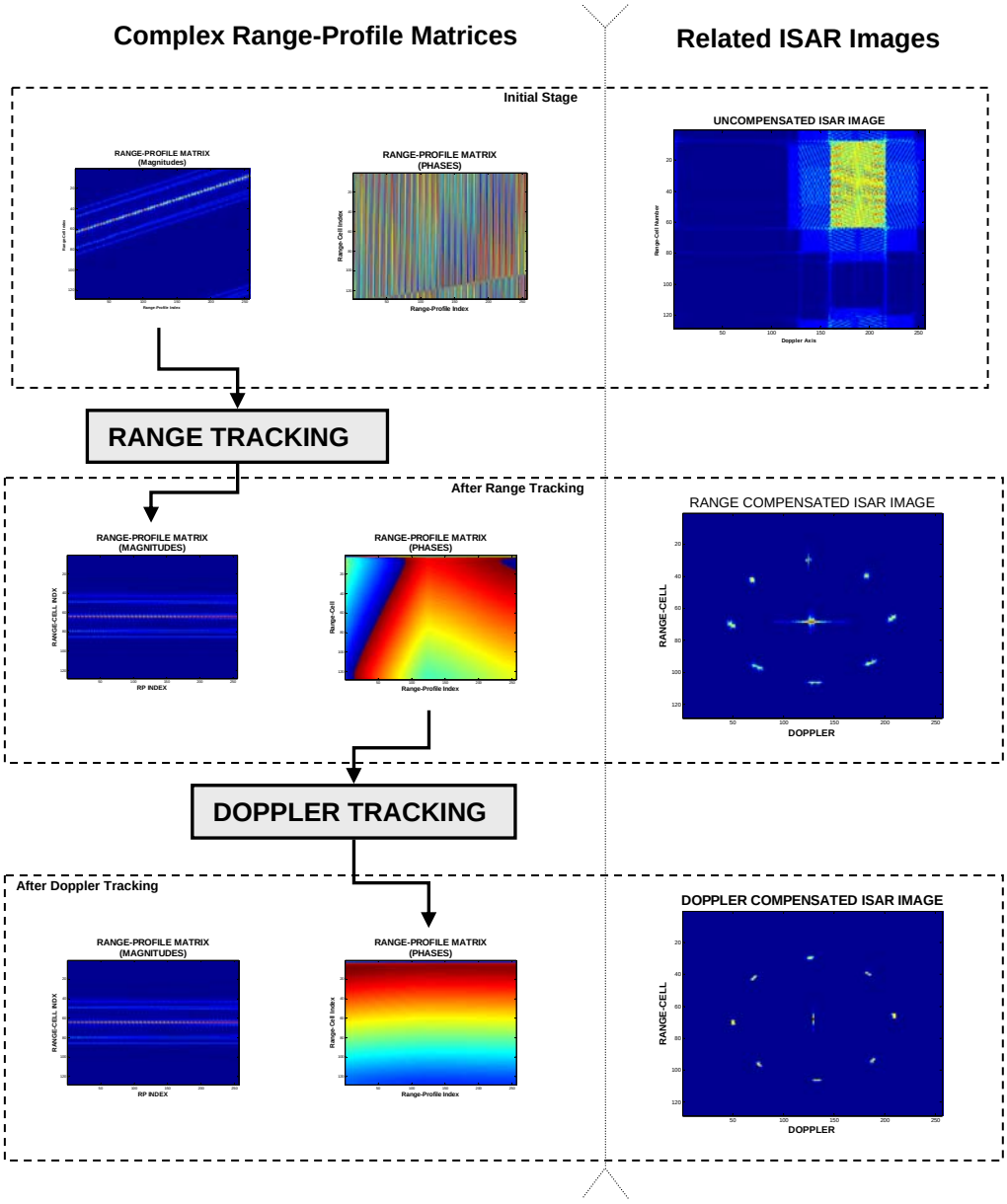

Figure 5.3 Standard translational motion compensation steps

3. The location of the peak of this cross-correlation process indicates the range shift (time delay) necessary for alignment with the reference RP. Not the peak values, but the peak indices of these range delays are stored in an array.
4. Resultant sequence of range delays need to be smoothed by fitting them to a low-order polynomial. Actually, some other kinds of corrections are needed because of the nature of the stepped-frequency radar signals. This subject is going to be discussed.
5. The smoothed delay corrections are applied to the original RPs by element-wise multiplication in the frequency domain, to the I-Q data.
6. Re-generation of the RPs is needed after this correction process.

5.4.2 Mathematical Details

Let us assume that there are M bursts are used each with N range-cells. It means that $N \times M$ number of complex *I-Q* pair is used for the ISAR Imaging. Hence raw I-Q data matrix could be represented as,

$$\begin{bmatrix} A_{1,1}\psi_{1,1} & A_{1,2}\psi_{1,2} & .. & .. & A_{1,l}\psi_{1,l} & A_{1,l+1}\psi_{1,l+1} & .. & .. & A_{1,M}\psi_{1,M} \\ . & . & . & . & . & . & . & . & . \\ . & . & . & . & . & . & . & . & . \\ . & . & . & . & . & . & . & . & . \\ . & . & . & . & A_{k,l}\psi_{k,l} & A_{k,l+1}\psi_{k,l+1} & . & . & . \\ . & . & . & . & . & . & . & . & . \\ . & . & . & . & . & . & . & . & . \\ . & . & . & . & . & . & . & . & . \\ A_{N,1}\psi_{N,1} & . & . & . & . & . & . & . & A_{N,M}\psi_{N,M} \end{bmatrix} \tag{5.11}$$

Assuming a constant translational velocity, v_t, the phase of the l^{th} burst's k^{th} element could be written as,

$$\psi_i\big|_{k,l} = -\frac{4\pi f_k}{c}\left[R_0 - PRI \cdot v_t \cdot \left(k-1+N\cdot\left(l-1\right)\right)\right] \tag{5.12}$$

where f_k is the transmitted frequency for k^{th} element. The phase of the $(l+1)^{th}$ burst's k^{th} element could be written as,

$$\psi_i\big|_{k,l+1} = -\frac{4\pi f_k}{c}\left[R_0 - PRI \cdot v_t \cdot \left(k - 1 + N \cdot l\right)\right] \tag{5.13}$$

Hence, burst-to-burst phase advance could be written as,

$$\Delta\psi\big|_{burst-to-burst} = \psi_i\big|_{k,l+1} - \psi_i\big|_{k,l} = \frac{4\pi f_k}{c} PRI \cdot v_t \cdot N = \frac{4\pi f_k}{c} \Delta R\big|_{burst-to-burst} \tag{5.14}$$

which does mean that, if $\Delta R\big|_{burst-to-burst}$ is somehow know, the range walk, which is a result of translational motion, could be eliminated, by an element wise multiplication of the matrix elements with this phase advance.

Actually, *main purpose of Range-Tracking is to find this phase advance, caused by* $\Delta R\big|_{burst-to-burst}$ *, by using the magnitudes of the RPs and then making a compensation for it.*

Let us define the complex RP matrix as,

$$\begin{bmatrix} RP_1 \\ RP_2 \\ . \\ . \\ . \\ . \\ . \\ . \\ . \\ RP_M \end{bmatrix}^T = \begin{bmatrix} A'_{1,1}\psi'_{1,1} & A'_{1,2}\psi'_{1,2} & .. & .. & A'_{1,l}\psi'_{1,l} & A'_{1,l+1}\psi'_{1,l+1} & .. & .. & A'_{1,M}\psi'_{1,M} \\ . & . & . & . & . & . & . & . & . \\ . & . & . & . & . & . & . & . & . \\ . & . & . & . & . & . & . & . & . \\ . & . & . & . & A'_{k,l}\psi'_{k,l} & A'_{k,l+1}\psi'_{k,l+1} & . & . & . \\ . & . & . & . & . & . & . & . & . \\ . & . & . & . & . & . & . & . & . \\ . & . & . & . & . & . & . & . & . \\ A'_{N,1}\psi'_{N,1} & . & . & . & . & . & . & . & A'_{N,M}\psi'_{N,M} \end{bmatrix} \tag{5.15}$$

which is the column-wise IFFT processed version of the Equation (5.11). Hence, every column defines a RP and every row a range-cell.

The reference RP could be represented as,

$$RP_{ref} = \left[A'_{1,ref}\psi'_{1,ref} \quad . \quad . \quad . \quad . \quad . \quad . \quad . \quad A'_{N,ref}\psi'_{N,ref} \right]^T \tag{5.16}$$

In all of the simulations in this thesis, first RP is used as the reference RP. Each RP (magnitude only) is going to cross-correlated with this reference RP as [6],

$$cr_l = \left| IDFT\left(DFT\left(\left| RP_{ref} \right| \right) \quad DFT\left(\left| RP_l \right| \right)^* \right) \right| \qquad \forall\, l = 1.....M \tag{5.17}$$

where DFT and IDFT represent the discrete Fourier operators. The location of the peak of cr_l indicates the range shift (time delay) necessary for alignment with the reference RP and could be represented as,

$$pk_l = location\left[\max\left(cr_l \right) \right] \qquad \forall\, l = 1.....M \tag{5.18}$$

The sequence of discrete range delays $pk_1, ..., pk_M$ is smoothed by fitting it to a low order polynomial,

$$s_{pk_l} = smoooth(pk_l) \tag{5.19}$$

Hence, $\Delta R\big|_{burst-to-burst}$ could be found as,

$$\Delta R_{ref-to-l} = \Delta r_s \times s_{pk_l} \tag{5.20}$$

where Δr_s is the slant-range resolution. All of the indices in the matrices represents *cell-number or burst-number* kind of things. In order to make a conversion from *index* to *meters*, this kind of multiplication, presented in Equation (5.20), has to be done.

Hence, phase advance of the l^{th} RP's k^{th} pulse, with respect to the reference RP could be written as,

$$\Delta\psi\big|_{k,l} = \frac{4\pi f_k}{c} \Delta R_{ref-to-l} \tag{5.21}$$

Then, range aligned RPs could be obtained as [6],

$$RP'_l = IDFT\left(\Delta\psi_l \begin{bmatrix} A_{1,l}\psi_{1,l} & . & . & . & . & . & . & . & A_{N,l}\psi_{N,l} \end{bmatrix}^T\right) \quad \forall\, l = 1.....M \quad (5.22)$$

where,

$$\Delta\psi_l = \begin{bmatrix} \Delta\psi\big|_{1,l} & . & . & . & . & . & . & . & \Delta\psi\big|_{N,l} \end{bmatrix}^T \quad (5.23)$$

After this range-alignment process, RP matrix could be represented as,

$$\begin{bmatrix} RP'_1 \\ RP'_2 \\ . \\ . \\ . \\ . \\ . \\ . \\ RP'_M \end{bmatrix}^T = \begin{bmatrix} B_{1,1}\Phi_{1,1} & B_{1,2}\Phi_{1,2} & .. & .. & B_{1,l}\Phi_{1,l} & B_{1,l+1}\Phi_{1,l+1} & .. & .. & B_{1,M}\Phi_{1,M} \\ . & . & . & . & . & . & . & . & . \\ . & . & . & . & . & . & . & . & . \\ . & . & . & . & . & . & . & . & . \\ . & . & . & . & B_{k,l}\Phi_{k,l} & B_{k,l+1}\Phi_{k,l+1} & . & . & . \\ . & . & . & . & . & . & . & . & . \\ . & . & . & . & . & . & . & . & . \\ . & . & . & . & . & . & . & . & . \\ B_{N,1}\Phi_{N,1} & . & . & . & . & . & . & . & B_{N,M}\Phi_{N,M} \end{bmatrix}$$

5.5 Doppler Tracking Application

Range Tracking ensures that each particular scatterer on the target only contribute to those cells which are aligned for cross-range processing. This does not, however, take into account phase changes caused by movement in range and any instantaneous radial velocity that exceed a small fraction of a wavelength [14].

Many of kind of Doppler tracking schemes are suggested from 80's up to now. Some of them could be listed as,

- Dominant scatterer algorithm [14,20,6],
- The sub-aperture approach [8,22],
- The cross-range centroid tracking [17],
- The phase gradient autofocus technique [18],

- Multiple prominent point processing [15,19],

Doppler Tracking application and algorithm in this thesis is constructed according to [14], [20] and [6]; the ***Dominant Scatterer Algorithm (DSA)***.

The basic principle of the DSA is to find a ***dominant scatterer*** and use that scatterer as a phase synchronizing source. The scatterer is considered dominant if it provides a majority contribution to the phasor sum of backscatter in a particular range-cell. Since a range-cell with a small amplitude variance is likely to be dominated by a single scatterer, the amplitude variance for each range-cell is calculated over the M RPs [6],

$$\sigma_k^2 = \frac{1}{M}\sum_{l=1}^{M}\left(B_{k,l} - \frac{1}{M}\sum_{l=1}^{M}B_{k,l}\right)^2 \qquad \forall\, k = 1,\ldots..,N \tag{5.24}$$

The range-cell with the minimum amplitude variance (range-cell q) is chosen as the phase synchronizing source as long as it satisfies the ***dominant*** scatterer criteria,

$$\sigma_q^2 < \sigma_k^2 \qquad \forall\, k \neq q \tag{5.25}$$

and

$$\sum_{l=1}^{M}\left(B_{q,l}\right)^2 > \frac{1}{N}\sum_{k=1}^{N}\left(\sum_{l=1}^{M}\left(B_{k,l}\right)^2\right) \tag{5.26}$$

The phase differences between the reference cell in the reference RP and the reference cell in every other RP could be calculated as [6],

$$\varphi_l = \Phi_{q,l} - \Phi_{q,p} \qquad \forall\, l = 1,\ldots..,M \tag{5.27}$$

These phase differences are applied to every RP as,

$$RP_l'' = RP'e^{-j\varphi l} \qquad \forall\, l = 1,\ldots..,M \tag{5.28}$$

After adaptive beamforming the RP data could be represented as

$$\begin{bmatrix} RP''_1 \\ RP''_2 \\ . \\ . \\ . \\ . \\ . \\ . \\ . \\ RP''_M \end{bmatrix}^T = \begin{bmatrix} B'_{1,1}\Phi'_{1,1} & B'_{1,2}\Phi'_{1,2} & .. & .. & B'_{1,l}\Phi'_{1,l} & B'_{1,l+1}\Phi'_{1,l+1} & .. & .. & B'_{1,M}\Phi'_{1,M} \\ . & . & . & . & . & . & . & . & . \\ . & . & . & . & . & . & . & . & . \\ . & . & . & . & . & . & . & . & . \\ . & . & . & . & B'_{k,l}\Phi'_{k,l} & B'_{k,l+1}\Phi'_{k,l+1} & . & . & . \\ . & . & . & . & . & . & . & . & . \\ . & . & . & . & . & . & . & . & . \\ . & . & . & . & . & . & . & . & . \\ B'_{N,1}\Phi'_{N,1} & . & . & . & . & . & . & . & B'_{N,M}\Phi'_{N,M} \end{bmatrix} \quad (5.29)$$

5.6 Applications of Range and Doppler Tracking

In this section, some case studies including the range and the Doppler tracking are presented. Examples are carefully chosen, in order to emphasize and highlight the critical points of the range and Doppler tracking algorithms.

First RP is chosen as the reference RP in all of the simulations and first order polynomial fitting is used for all of the Simulations, except the last simulation, which is included in order to show the importance of the degree of the fitting function.

The Simulation Model-1 is illustrated in Figure 5.4. It is the nine-point scatterer model given in Chapter 3.2.2. All of the scatterers are assumed to have same radar cross section along the coherent integration time. Simulation parameters are listed in Table 5.1. In order to explain the cross-correlation process, small amount of translational motion is induced to the target. Initial ISAR image (without any kind of motion compensation) is shown in Figure 5.5 with the related RP matrix. Figure 5.6(a) shows the effect of the cross-correlation process. Hence, it could be said that, *50th RP seems like the 3 range-cell shifted version of the reference RP*. These results are fit to a low order polynomial in order to smooth them. Result of this smoothing process is given in Figure 5.6(b) with the dashed line. This smoothing procedure has to be done. Because, in reality, targets exhibit continuous movements; not like range-cell-by-range-cell. This figure contains one more line called Re-arranged Range-Delays and shown by a solid line. The importance of this line is going to be discussed in 3rd simulation example. Then, Range Tracked RPs and ISAR Image are

shown in Figure 5.7. Each single scatterer is distinguishable but a little bit blurring still exists. It is because of the target's small uncompensated movements which are only a fraction of wavelength. Figure 5.8 illustrates the results of Doppler Tracking, by the way of resultant RP and ISAR images. In this simulation, the upper scatterer (the closest one to the radar point) is chosen as the Dominant Scatterer, by the algorithm. Someone could identify the Dominant Scatterer by looking at the ISAR image: chosen Dominant Scatterer appears at the center vertical line of the ISAR image, which corresponds to a DC component.

The same simulation model is used in Simulation-2. The only difference is the increased rotational velocity, which is 3 deg/sec. As a result of this, each single scatterer appears like two connected scatterers, as a result of Range Tracking (Figure 5.12), which does not fit to the real situation. The power of DSA, Doppler Tracking shows itself on the resultant ISAR image in Figure 5.13.

The simulation model given in Figure 5.14 is used in Simulation-3, in order to show the power of Range and Doppler Tracking schemes. The model contains three circles, one is located within the other. Every circle has equally spaced eight scatterers and one more scatterer is also located to the center of the geometry. Hence, there are total twenty-five number of scatterers are used in Simulation-3. The distance between the circles are equal to 5 m and the radius of the inner circle is 30 m. The most important point in this simulation is the induced translational motion, which is equal to 250 m/sec. This is a realistic value if we think of the combat planes. The length of the range window is 150 m and total image time is 819 milliseconds. Hence, this target moves ahead nearly 1.4 times of the total range-window. This could be seen in both RPs of Figure 5.15 and cross-correlation results of Figure 5.16(a). Importance of the Re-Arrangement of the Range-Delay functions (shown in Figure 5.16(b) with solid lines) could be seen by a comparison of raw cross-correlation results, Figure 5.16(a), and re-arranged range delays, Figure 5.16(b). Figure 5.17 shows range tracking results. It is an interesting illustration. Because of the fast maneuvering characteristic of the target, it seems like two chained, separate targets. Figure 5.18 illustrates the results of Doppler Tracking, which denotes nearly perfect Doppler compensation.

The Simulation model-4 is illustrated in Figure 5.19. This simulation is given in order to emphasize the ***lack of DSA algorithm***. Related parameters of the simulation are given in Table 5.4. Figure 5.20 shows uncompensated RPs and ISAR Image. Figure 5.22 shows that the range tracking is enough to achieve compensated image for this case. But the algorithm is forced to choose the 77th range-cell, as the Dominant Scatterer's location, which is actually not true. Hence the result is illustrated in Figure 5.23. Doppler tracked image looks like three separate circles. 77th range-cell contains three equal strength scatterers; so they are not dominant about the each other. Hence, the image is compensated according to each of the three circles, which results in abrupt image shifts in cross-range dimension. Actually this point was stated in [13] and [20] at different times. [14] and [20] also states that the DSA method is applicable and gives good results if one of the scatterers energy in that range-cell is at least 4 dB above the total of the all other scatterers in that range-cell.

The Simulation model-5 is illustrated in Figure 5.24, which was also used in Chapter 4.5. All of the scatterers are assumed to have same radar cross section in the coherent integration time. Simulation parameters are listed in Table 5.5. Figure 5.25 shows uncompensated RPs and ISAR image. The most important feature of this simulation model is that the scatterers are closer to each other. Hence, cross-correlation process could produce small ripples around a mean value, as shown in Figure 5.26. This results with a small misalignment in range-axis after the range tracking (Figure 5.27), especially if a scatterer does not dominate the RP signatures. Thus, Doppler tracked ISAR image quality is a decreased in respect to this range alignment (Figure 5.28).

Sixth simulation (Figure 5.29) is a typical example of range-misalignment, where the range tracking algorithm fails. Related parameters of this simulation are given in Table 5.6. Figure 5.30 shows uncompensated RPs and ISAR image. Because of the high ripples in the re-arranged range delays, solid line in Figure 5.31(b), smooth operation is failed, dashed line in Figure 5.31(b). Range-misalignment could be seen in Figure 5.32 very clearly. If the range tracking algorithm fails, then there isn't any possibility and chance of successful Doppler Tracking. Hence, Figure 5.33 shows the natural result of image blurring because of failed range tracking process.

Simulation-7 is generated with the parameters of Simulation-6 shown in Table 5.6. The only difference is the dominating tail scatterer, which could be seen in Figure 5.35(a) as a dominant black line. This dominating tail scatterer makes the cross-correlation and also smoothing process to operate successfully. Figure 5.36 shows range tracked RPs and ISAR image. There is still considerable amount of Doppler shifts, but now, kept inside the range-cells. Doppler tracking results are shown in Figure 5.37. The model has five closer point-scatterers on the nose of the target. But these points are still not distinguishable as shown in Figure 5.37(b). Now, let the domination scatterer be the fuselage (center) of the target (Figure 5.38). Then, these five-points are a-little bit (but not completely) resolvable. But if the dominant scatterer is located near the nose of the target, then all of the closer five scatterers are very well distinguishable as shown in Figure 5.39. Hence, it could be concluded that the location of the dominant scatterer also determines the clarity and resolvability of the image partially: nearer points to the reference dominant scatterer are much more resolvable.

The last example, Simulation-8, is given in order to emphasize the importance of the polynomial fitting procedure of range delays, which are the results of cross-correlation of RPs. The model is illustrated in Figure 5.40. The target is traveling tangential to the radar's LOS with a translational velocity of 350 m/sec. This target could be thought as a supersonic plane. It exhibits some rotational motion around itself at the same time, with a velocity of 4 deg/sec. Figure 5.41 is an illustration of the uncompensated RPs and ISAR image. In this case, trajectory of the range profiles follows some kind of parabolic track. If the results of cross-correlation process, range-delays, are fit to a first order polynomial, as shown in Figure 5.42, RPs become as shown in Figure 5.44 and the resultant ISAR image is going to be look like as shown in Figure 5.45. High level of smearing could be observed in Figure 5.45, as a result of range-misalignment (shown in Figure 5.44). Figure 5.43 illustrates the results of second order polynomial fitting. Figure 5.46 proves that the second order fitting is much more effective for this example, where the target's trajectory exhibits a parabolic curve. Figure 5.47 is the Range-Doppler ISAR image, after the Doppler tracking. If Figure 5.47 is compared with Figure 5.45, it could be concluded that the second order polynomial fitting is the best solution for this case.

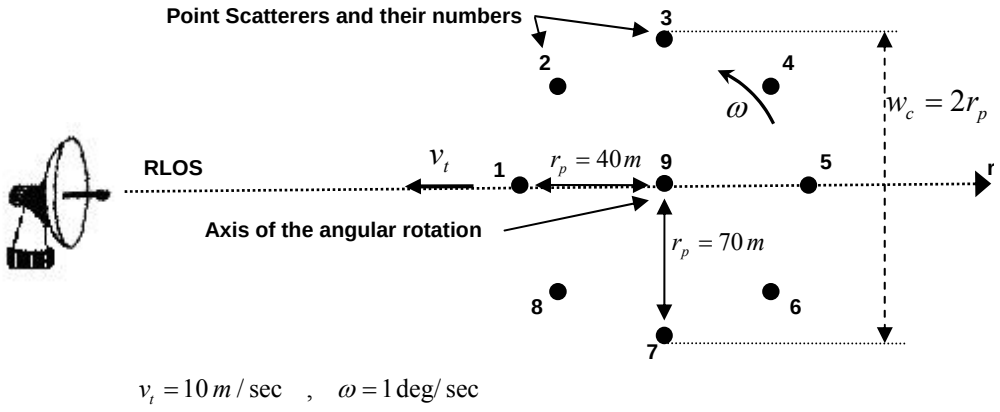

Figure 5.4 Illustration of the Simulation Model-1

Table 5.1 Parameters of Simulation-1

Parameter Description	***Value***
Rotational Velocity, ω *, (degrees/sec)*	1
Translational velocity, v_t *, (m/sec)*	10
Δf , frequency-step size, MHz	1
f_0 , starting frequency, GHz	9
N , The number of discrete pulses per burst	128
M , The number of bursts	128
β , The effective bandwidth of a burst, MHz	128
T_P , The pulse width, μsec	5
T_{PRI} , The pulse repetition interval (PRI), μsec	50
T, Coherent Integration Time, seconds	0.819

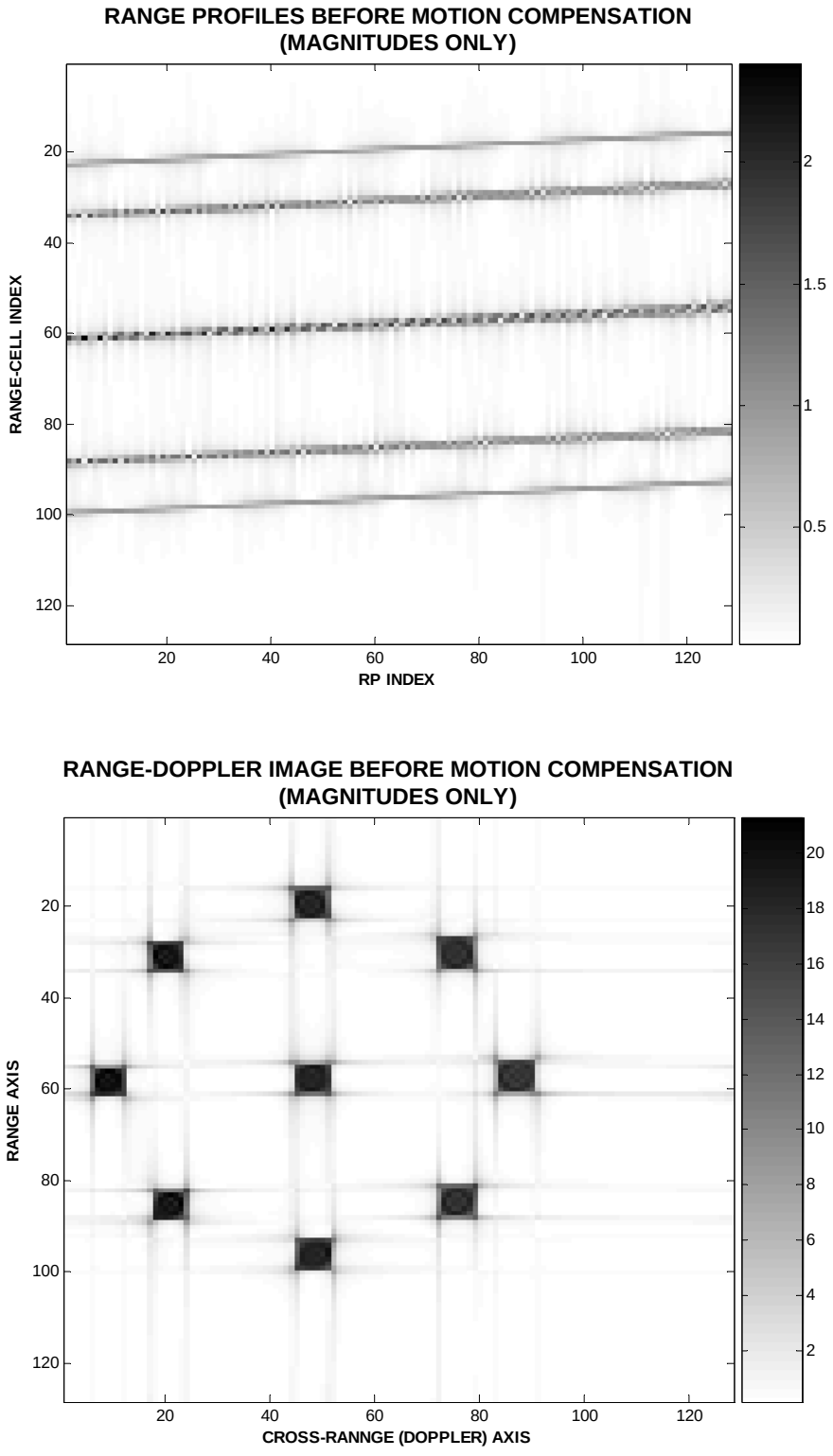

Figure 5.5 Uncompensated RPs and related ISAR Image of Simulation Model-1

(a)

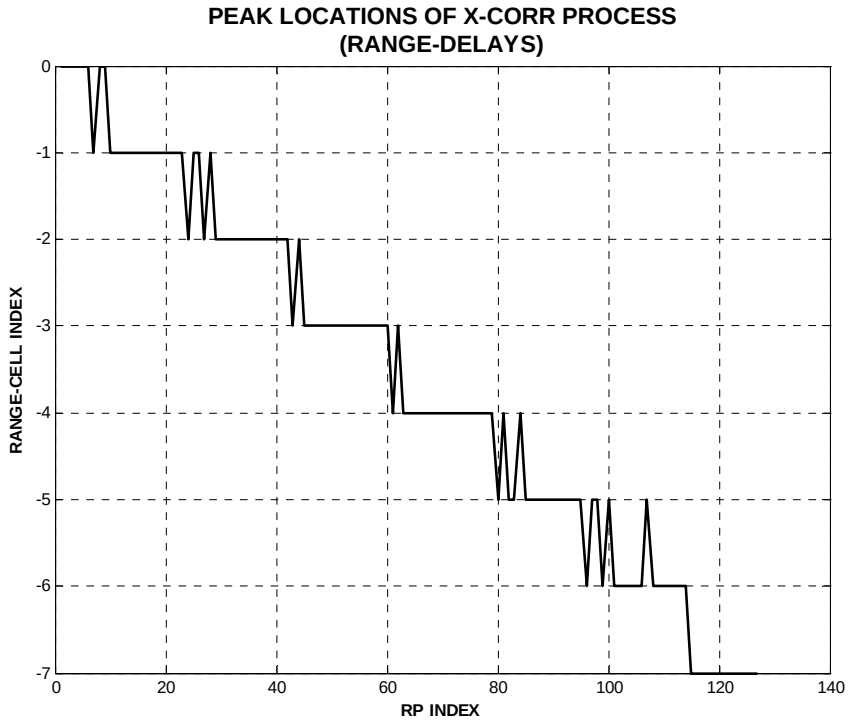

(b)

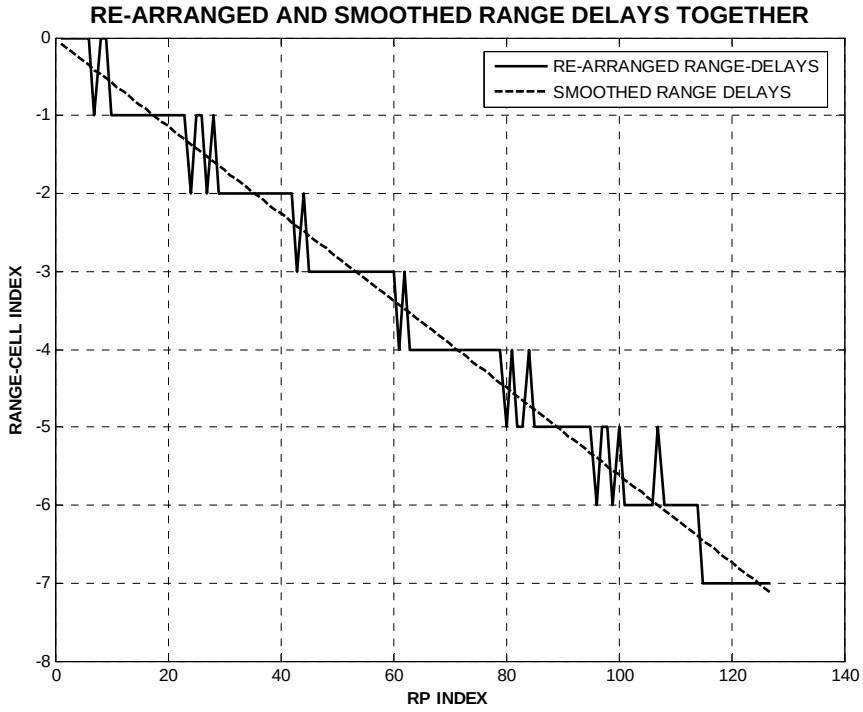

Figure 5.6 Cross-Correlation results of Simulation-1

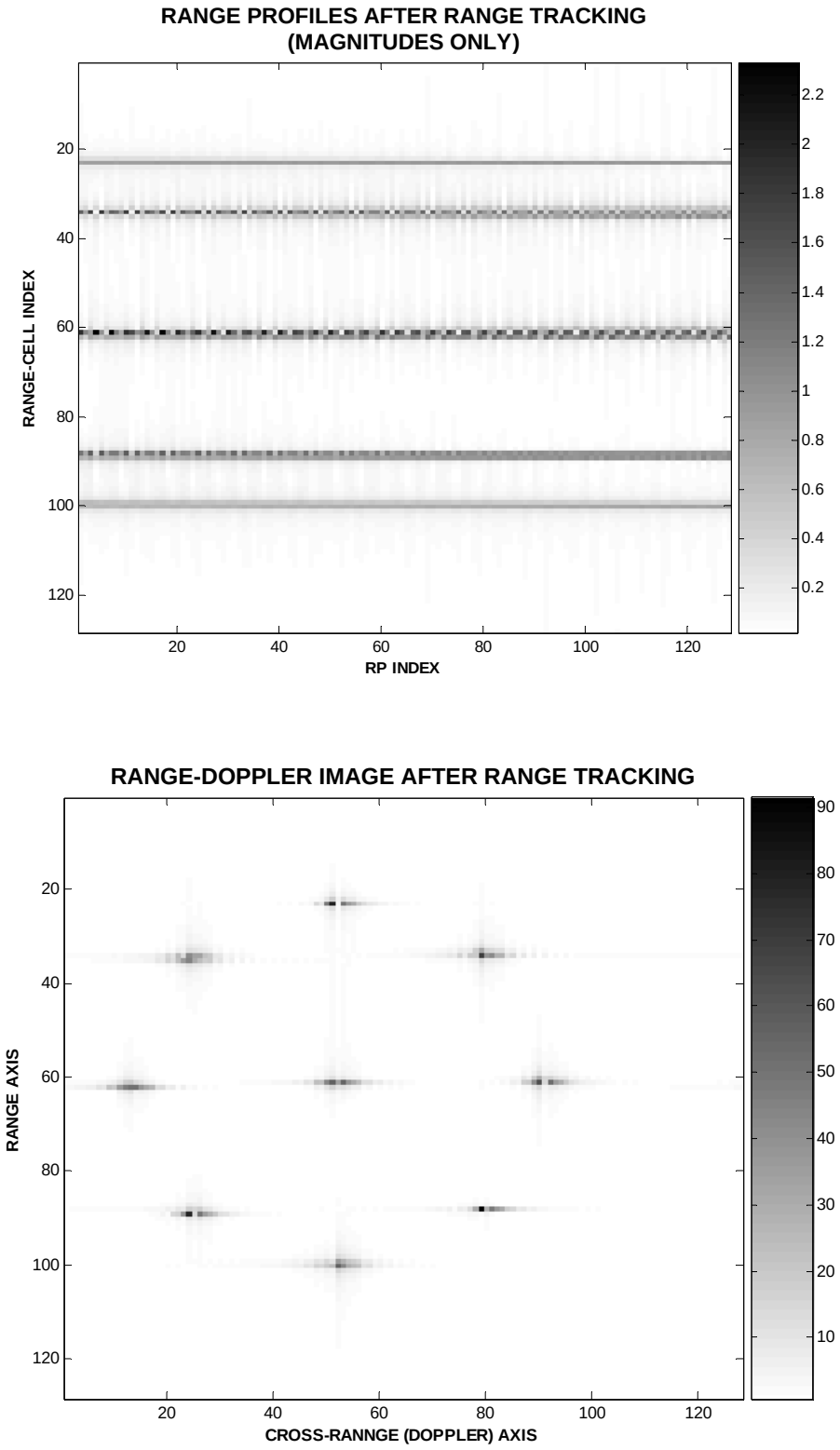

Figure 5.7 RPs and ISAR Image after Range Tracking algorithm: Simulation Model-1

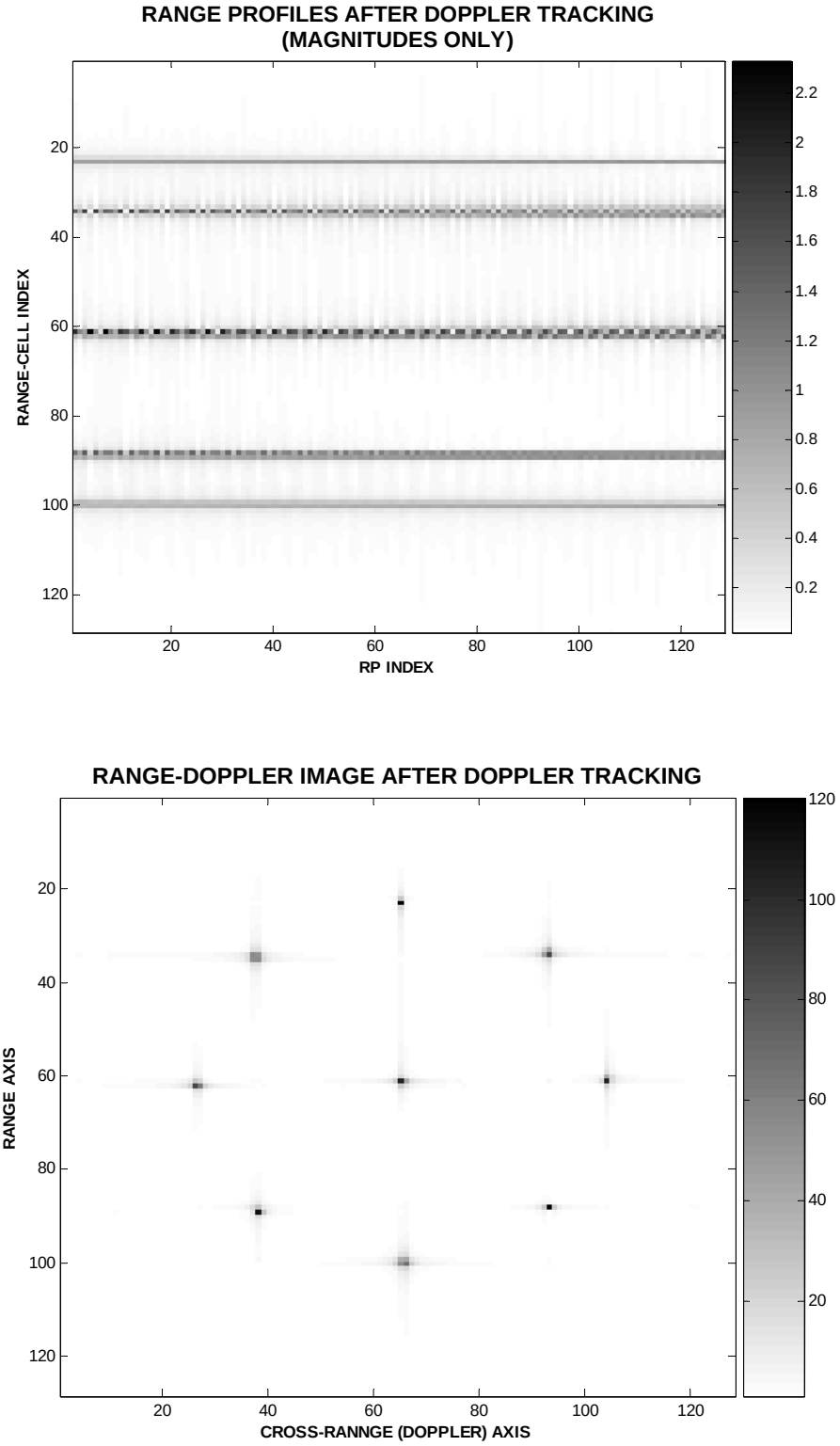

Figure 5.8 RPs and ISAR Image after Doppler Tracking algorithm: Simulation Model-1

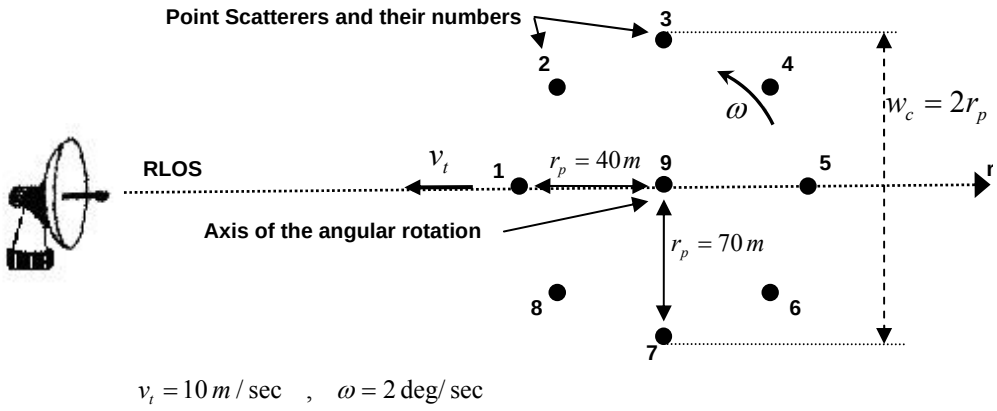

Figure 5.9 Illustration of the Simulation Model-2

Table 5.2 Parameters of Simulation-2

Parameter Description	***Value***
Rotational Velocity, ω *, (degrees/sec)*	2
Translational velocity, v_t *, (m/sec)*	10
Δf , frequency-step size, MHz	1
f_0 , starting frequency, GHz	3
N , The number of discrete pulses per burst	128
M , The number of bursts	128
β , The effective bandwidth of a burst, MHz	128
T_P , The pulse width, μsec	5
T_{PRI} , The pulse repetition interval (PRI), μsec	50
T, Coherent Integration Time, seconds	0.819

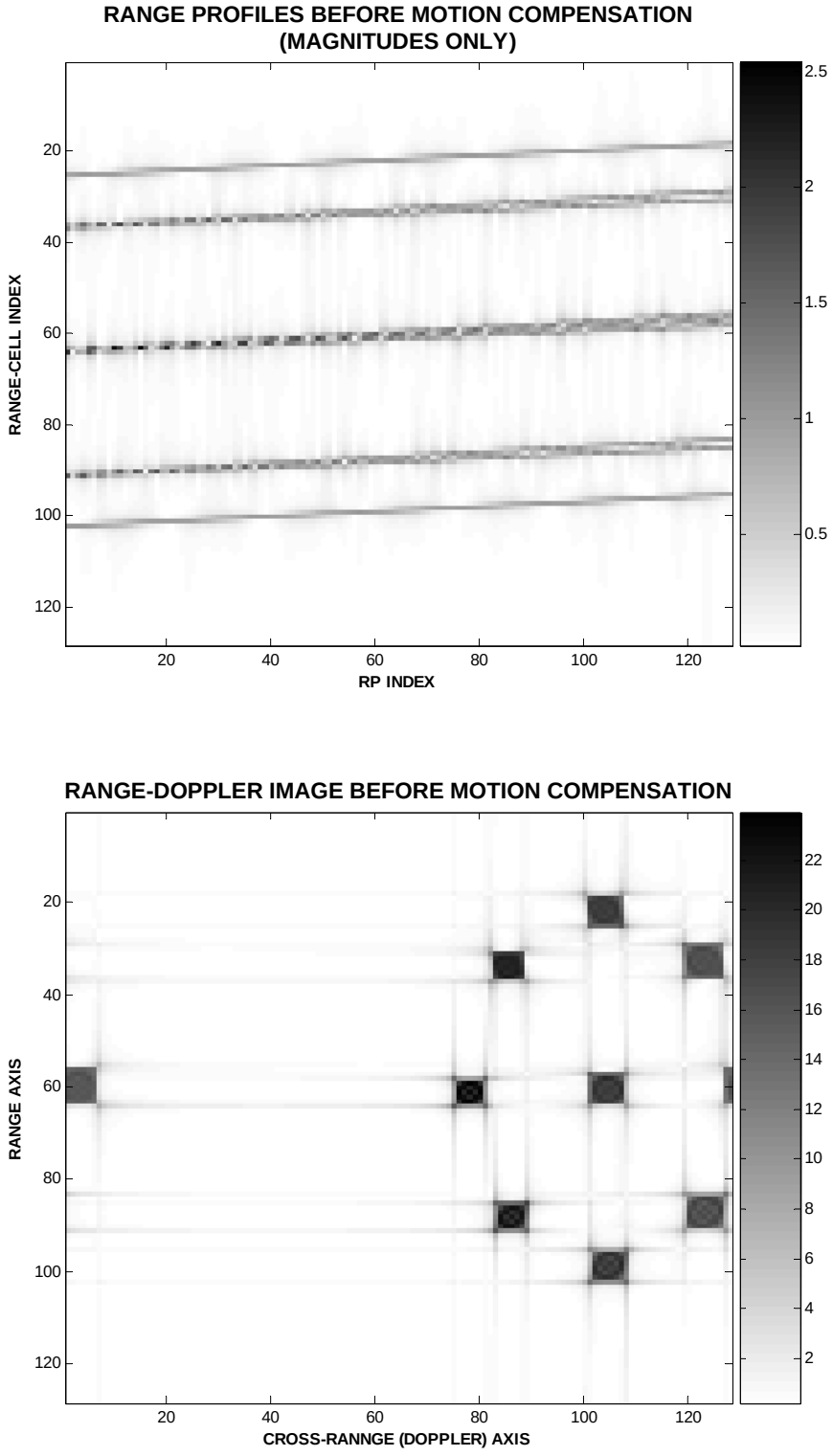

Figure 5.10 Uncompensated RPs and related ISAR Image of Simulation Model-2

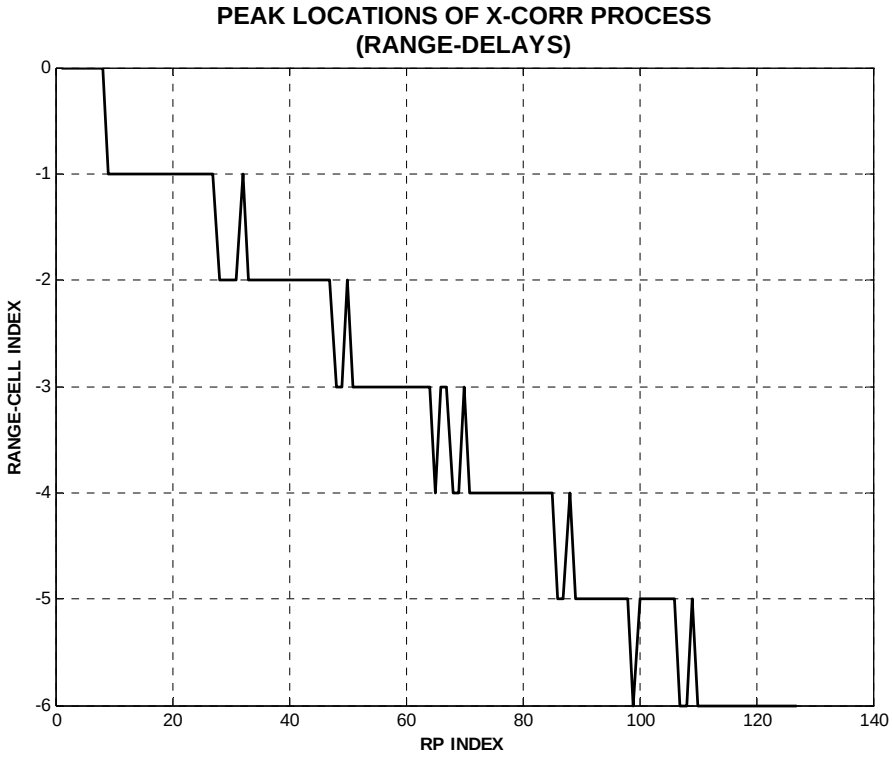

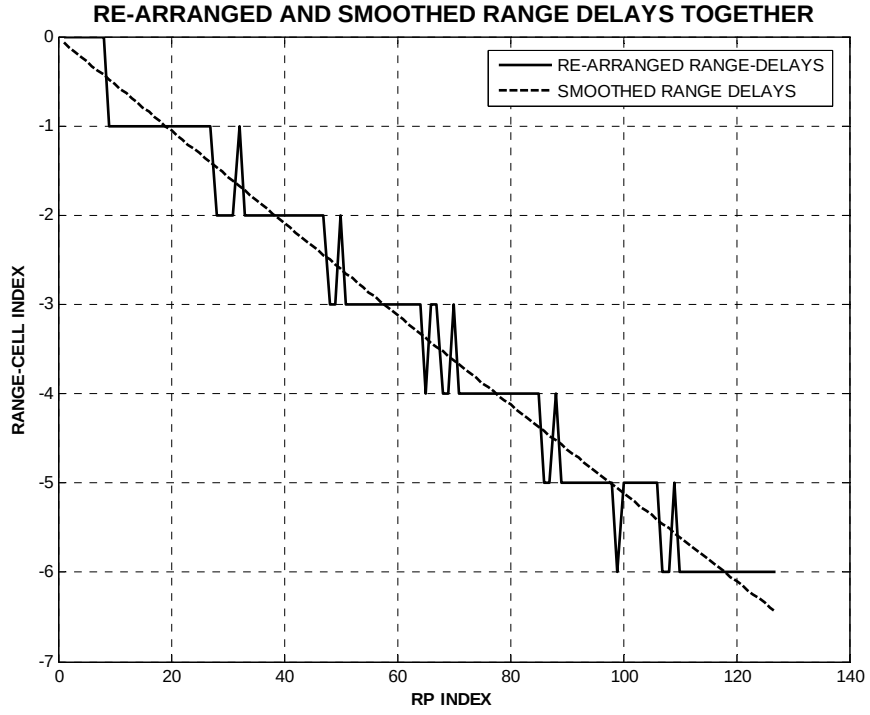

Figure 5.11 Cross-Correlation results of Simulation-2

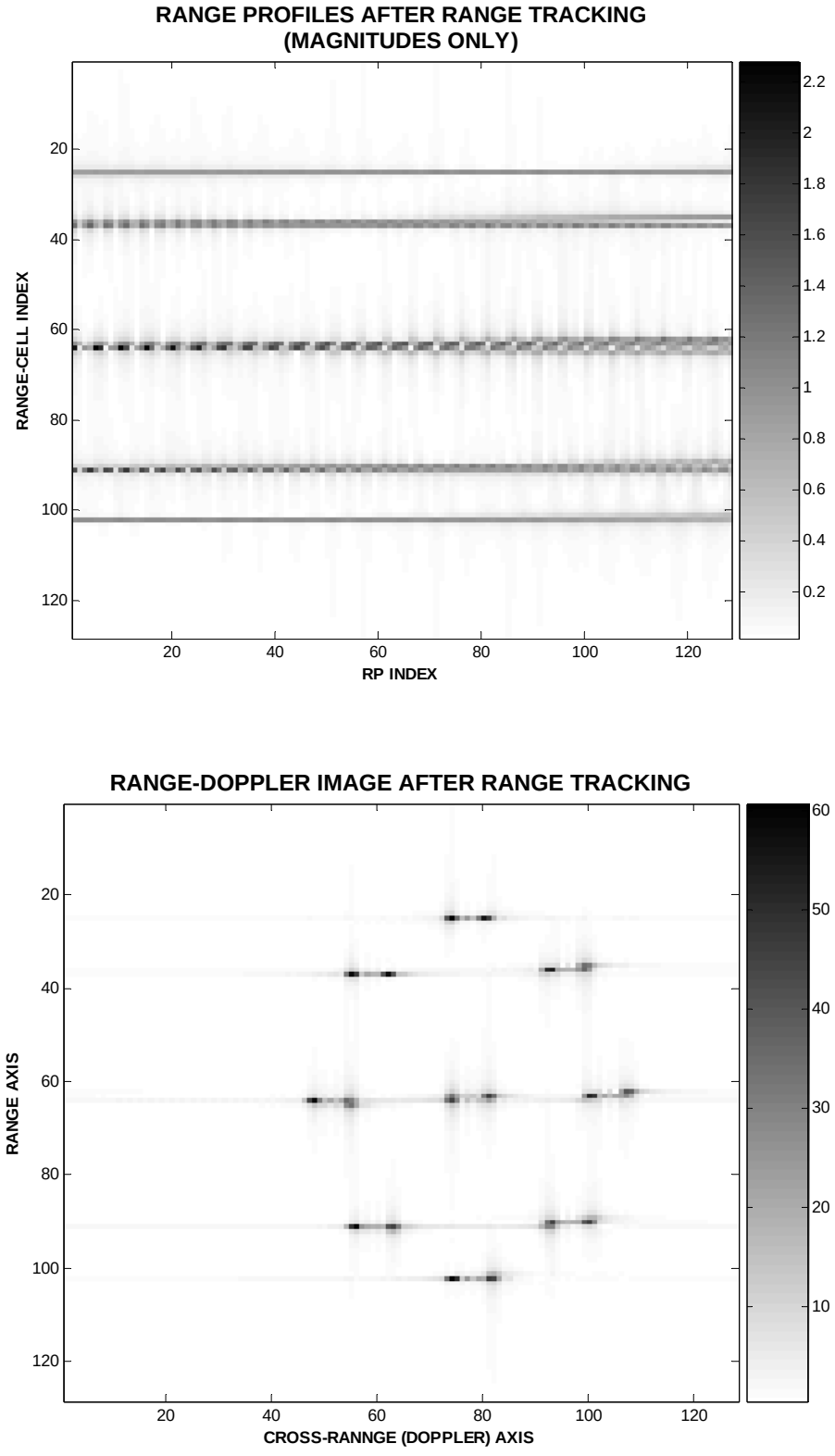

Figure 5.12 RPs and ISAR Image after Range Tracking algorithm: Simulation Model-2

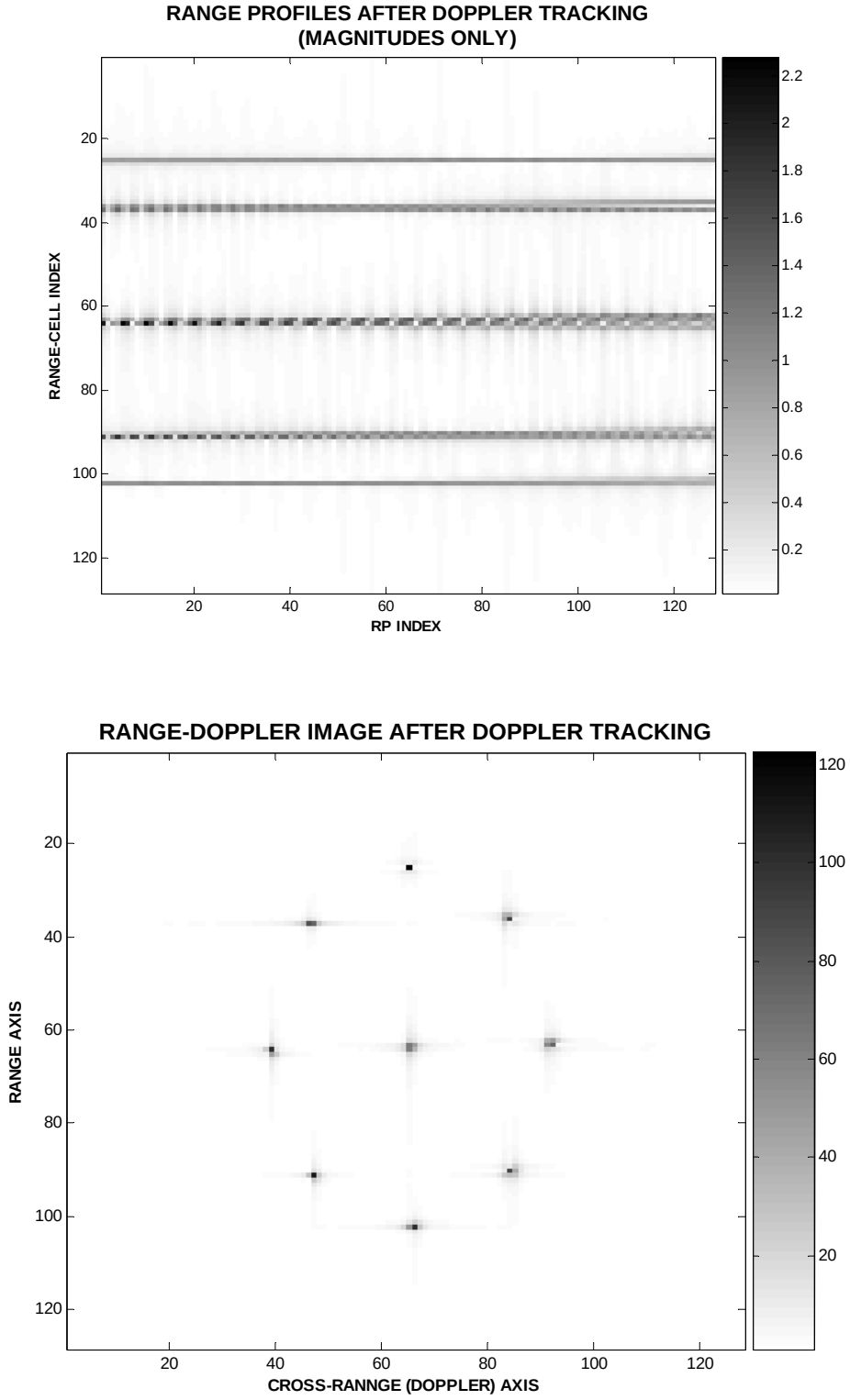

Figure 5.13 RPs and ISAR Image after Doppler Tracking algorithm: Simulation Model-2

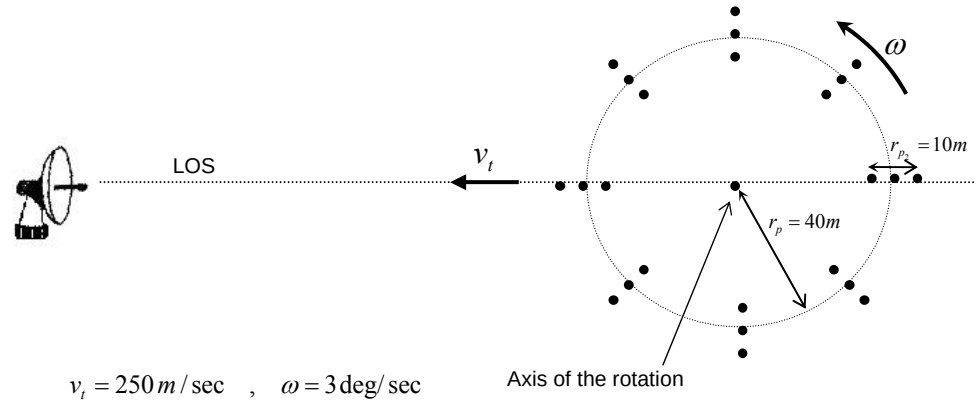

Figure 5.14 Illustration of the Simulation Model-3

Table 5.3 Parameters of Simulation-3

Parameter Description	***Value***
Rotational Velocity, ω *, (degrees/sec)*	3
Translational velocity, v_t *, (m/sec)*	250
Δf , frequency-step size, MHz	1
f_0, starting frequency, GHz	3
N , The number of discrete pulses per burst	128
M , The number of bursts	128
β , The effective bandwidth of a burst, MHz	128
T_P , The pulse width, μsec	5
T_{PRI} , The pulse repetition interval (PRI), μsec	50
T, Coherent Integration Time, seconds	0.819

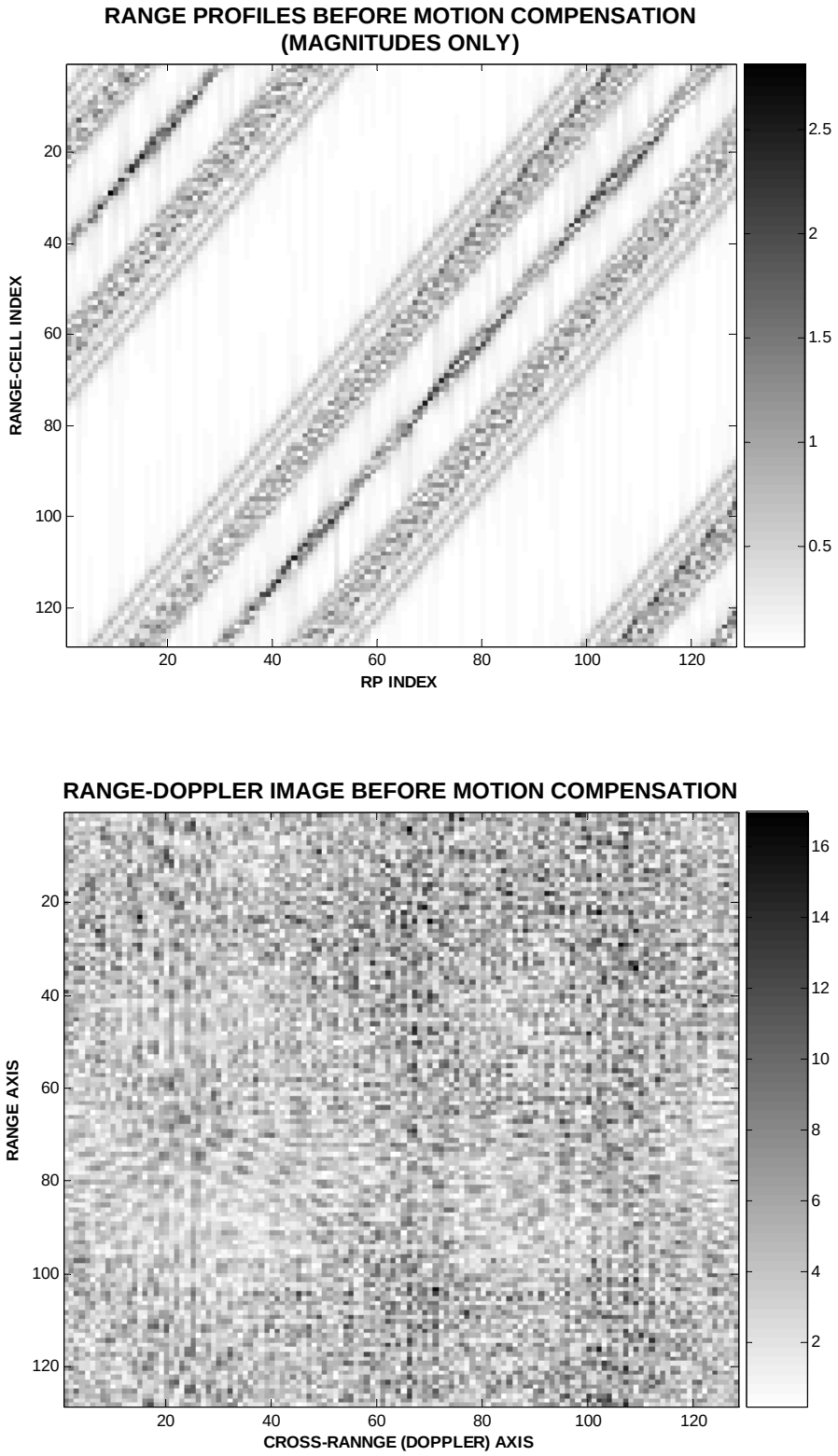

Figure 5.15 Uncompensated RPs and related ISAR Image of Simulation Model-3

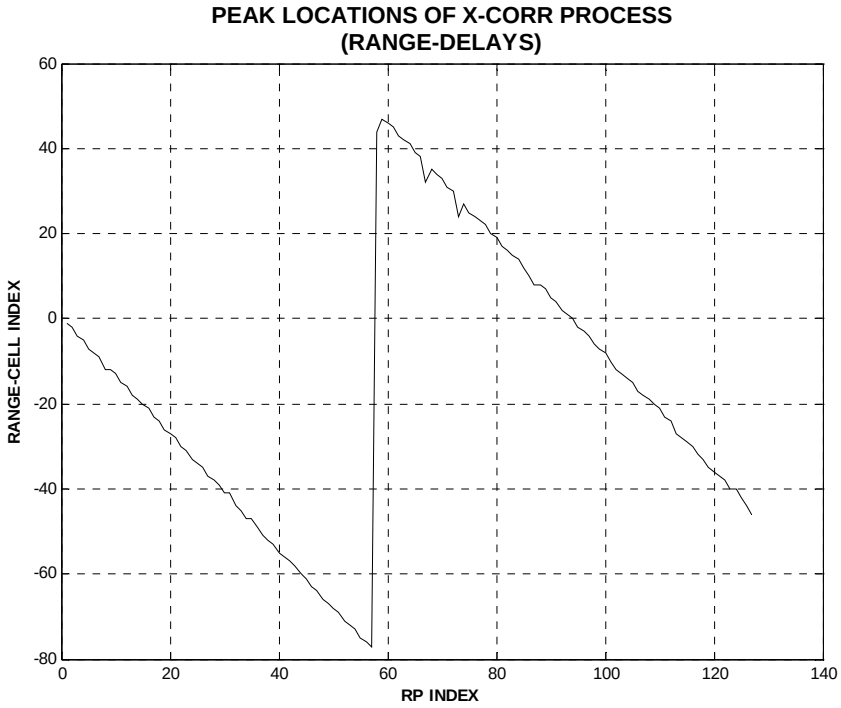

(a)

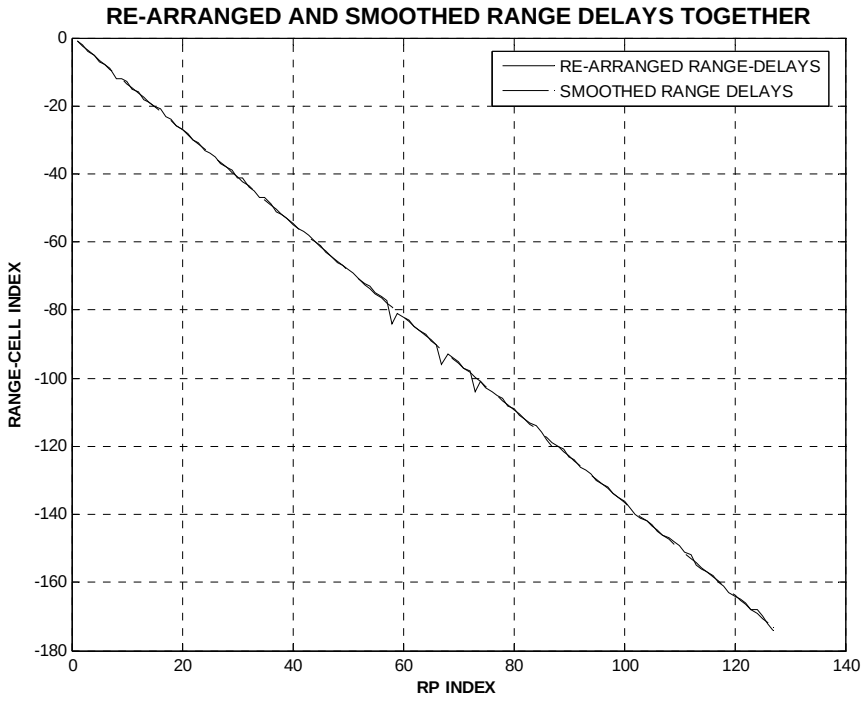

(b)

Figure 5.16 Cross-Correlation results of Simulation-3

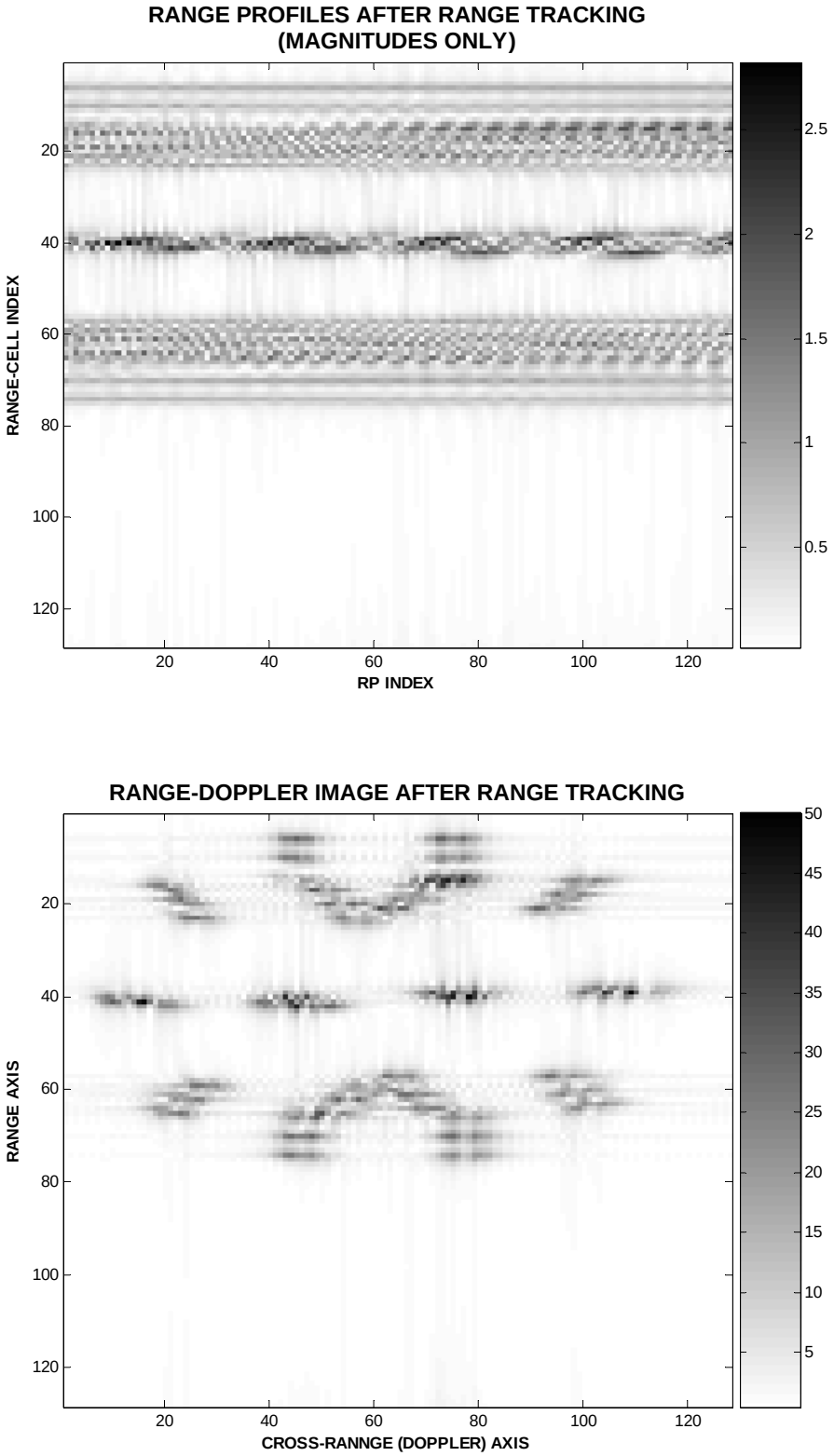

Figure 5.17 RPs and ISAR Image after Range Tracking algorithm: Simulation Model-3

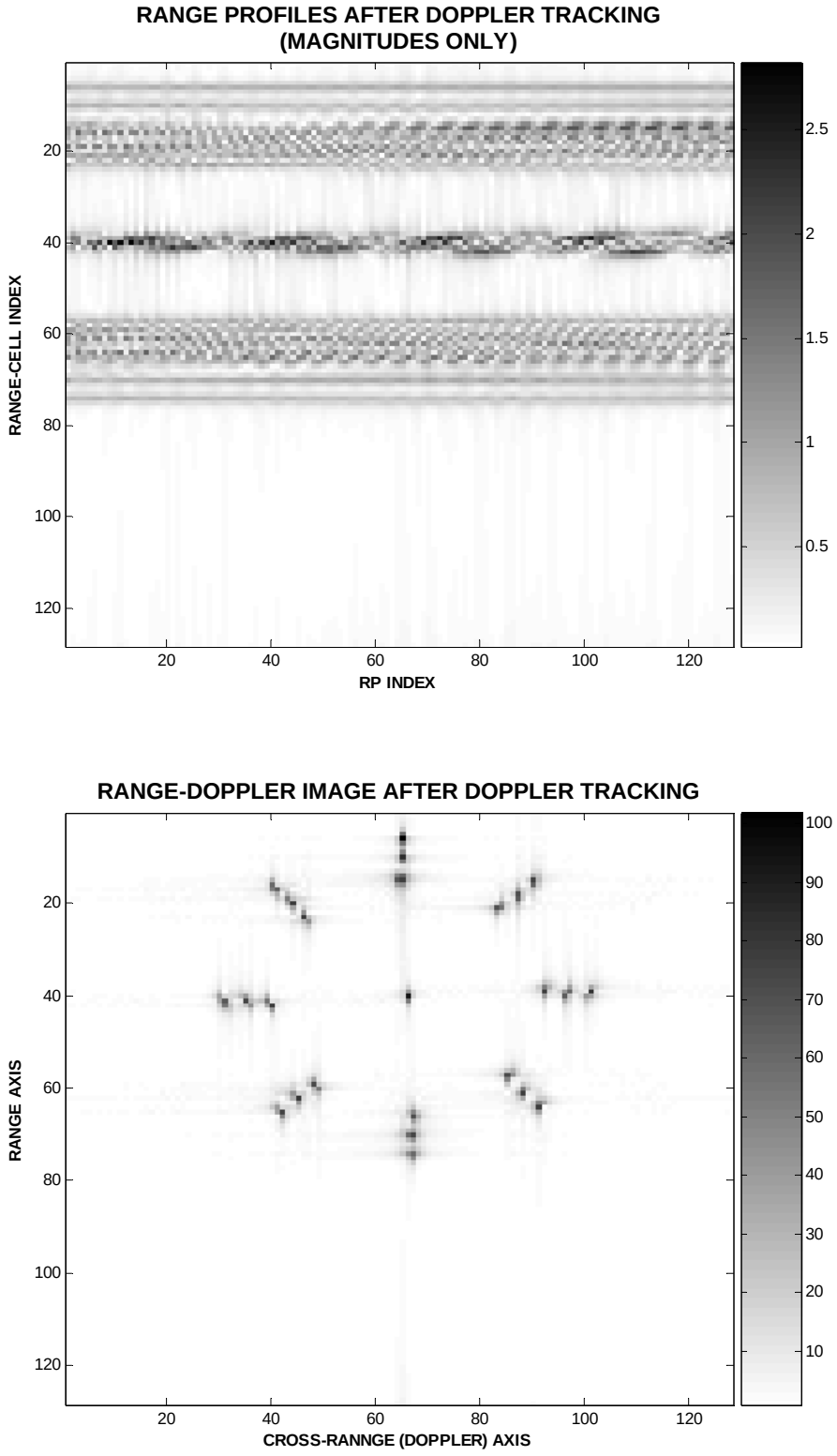

Figure 5.18 RPs and ISAR Image after Doppler Tracking algorithm: Simulation Model-3

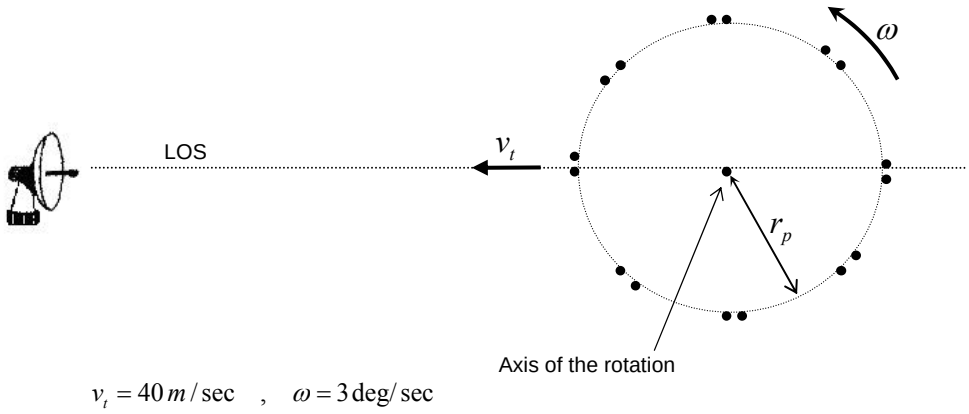

Figure 5.19 Illustration of the Simulation Model-4

Table 5.4 Parameters of Simulation-4

Parameter Description	***Value***
Rotational Velocity, ω *, (degrees/sec)*	3
Translational velocity, v_t *, (m/sec)*	40
Δf , frequency-step size, MHz	1
f_0, starting frequency, GHz	3
N , The number of discrete pulses per burst	128
M , The number of bursts	128
β , The effective bandwidth of a burst, MHz	128
T_P , The pulse width, μsec	5
T_{PRI} , The pulse repetition interval (PRI), μsec	50
T, Coherent Integration Time, seconds	0.819

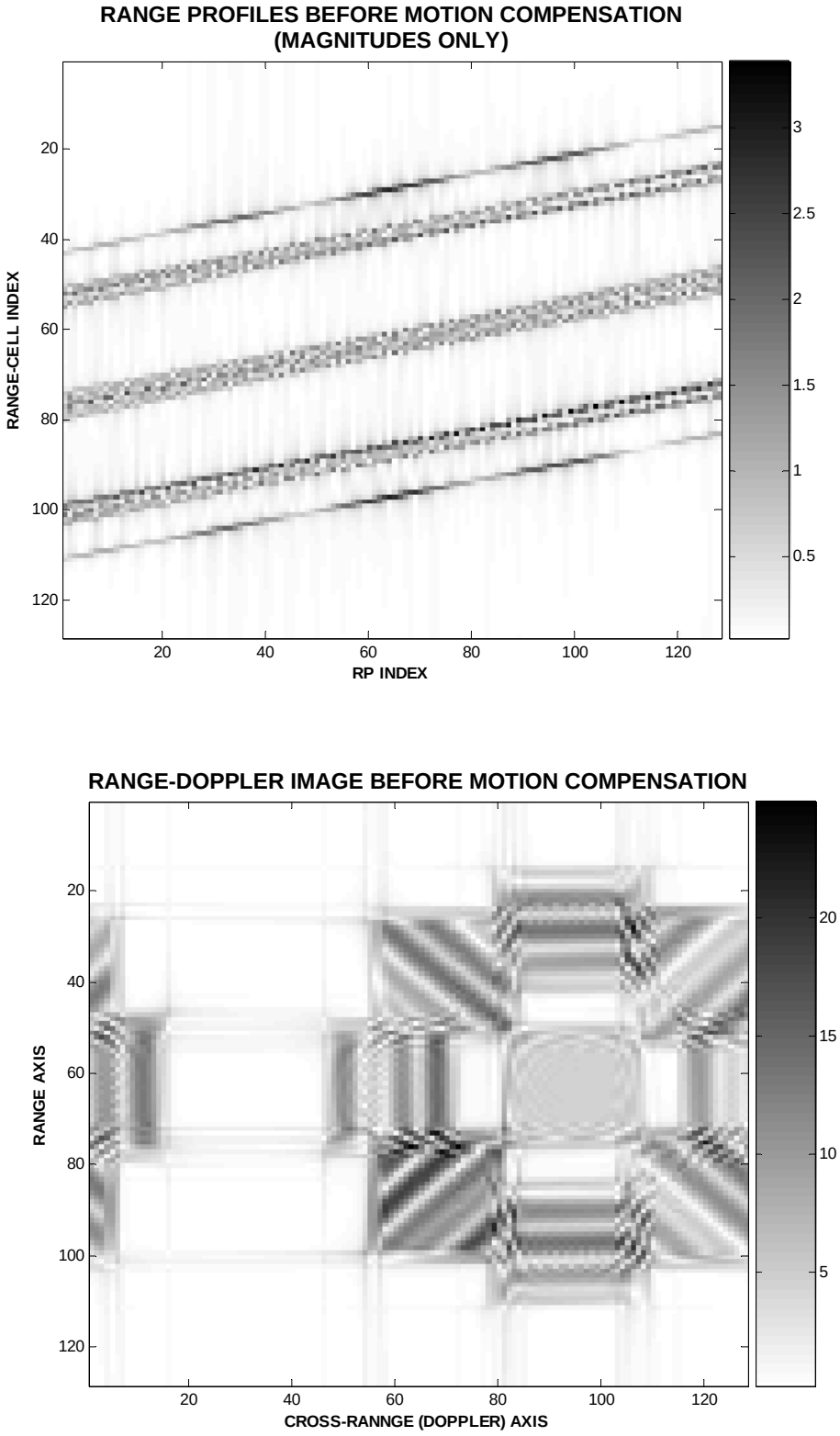

Figure 5.20 Uncompensated RPs and related ISAR Image of Simulation Model-4

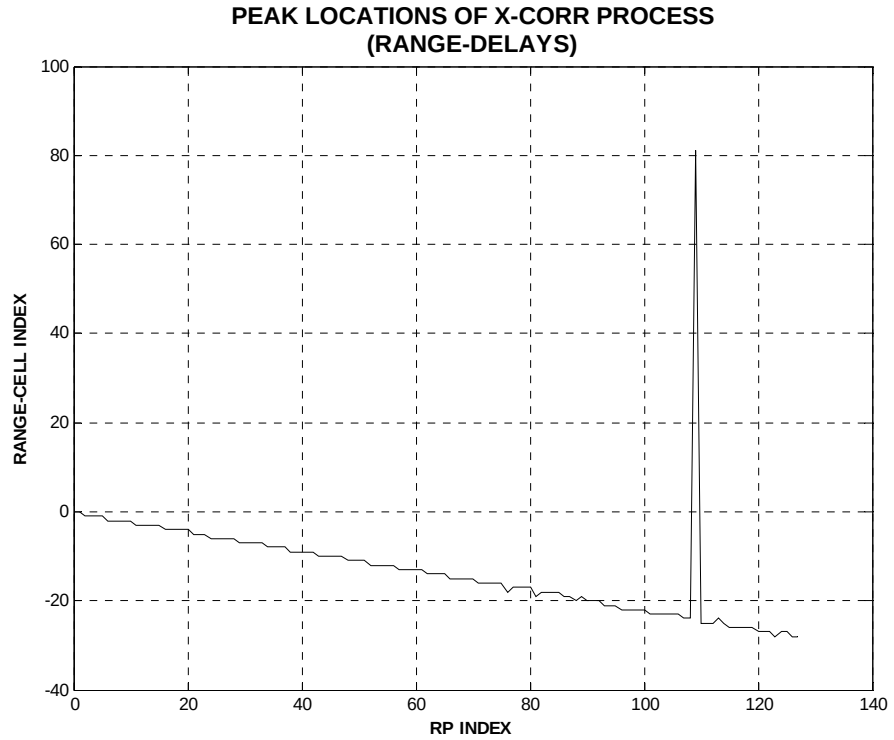

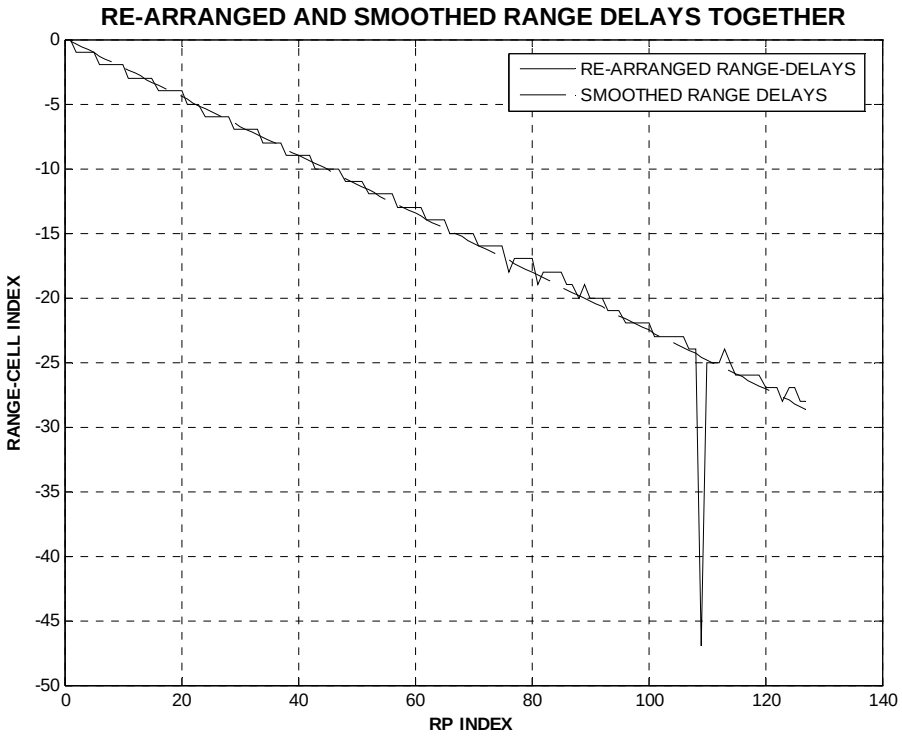

Figure 5.21 Cross-Correlation results of Simulation-4

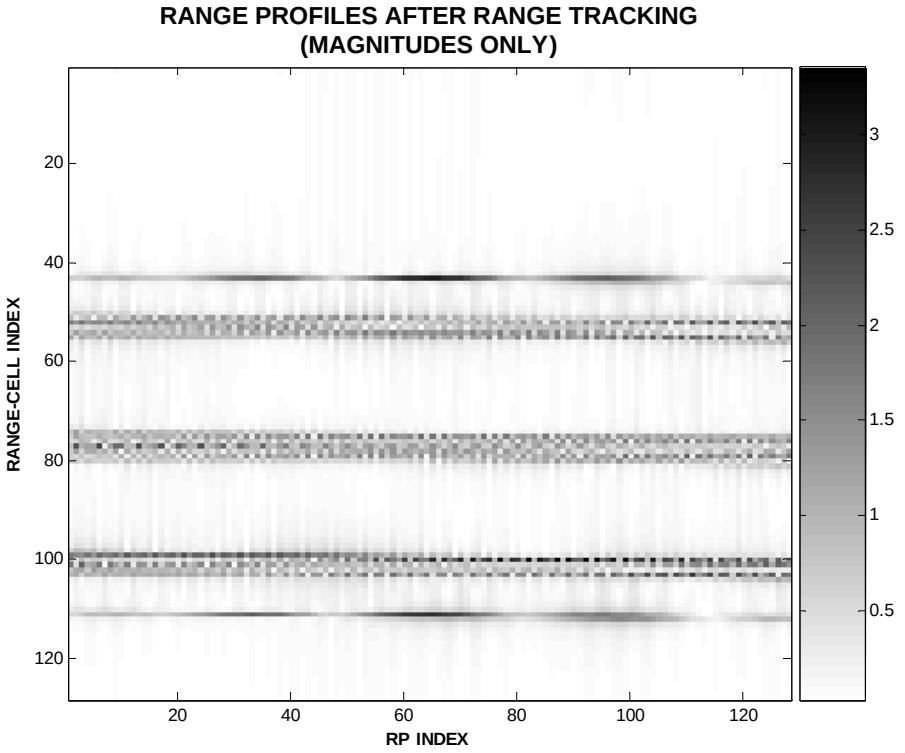

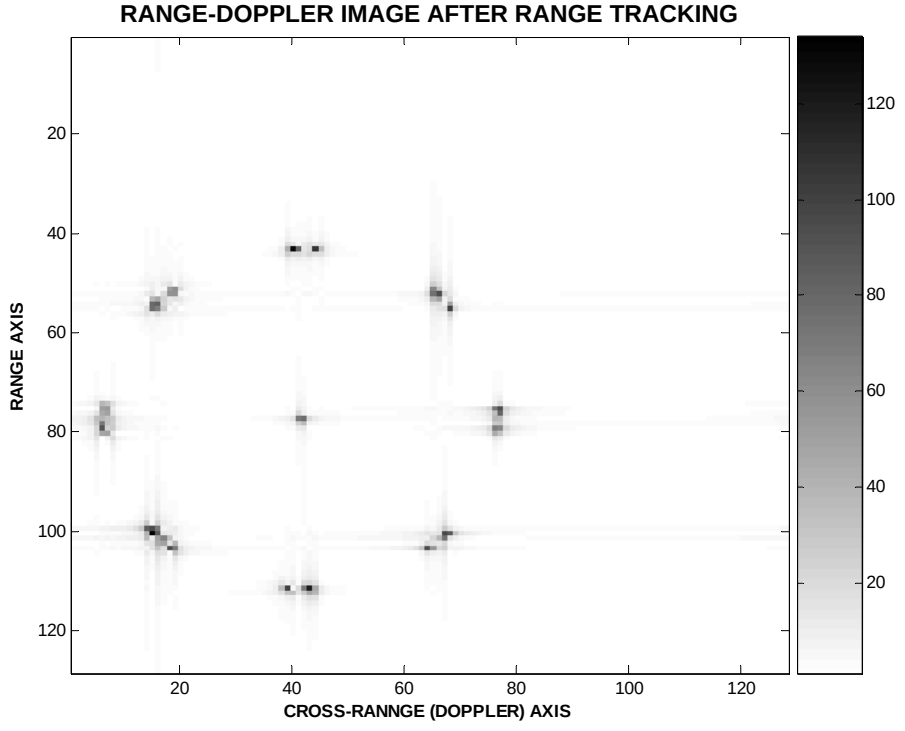

Figure 5.22 RPs and ISAR Image after Range Tracking algorithm: Simulation Model-4

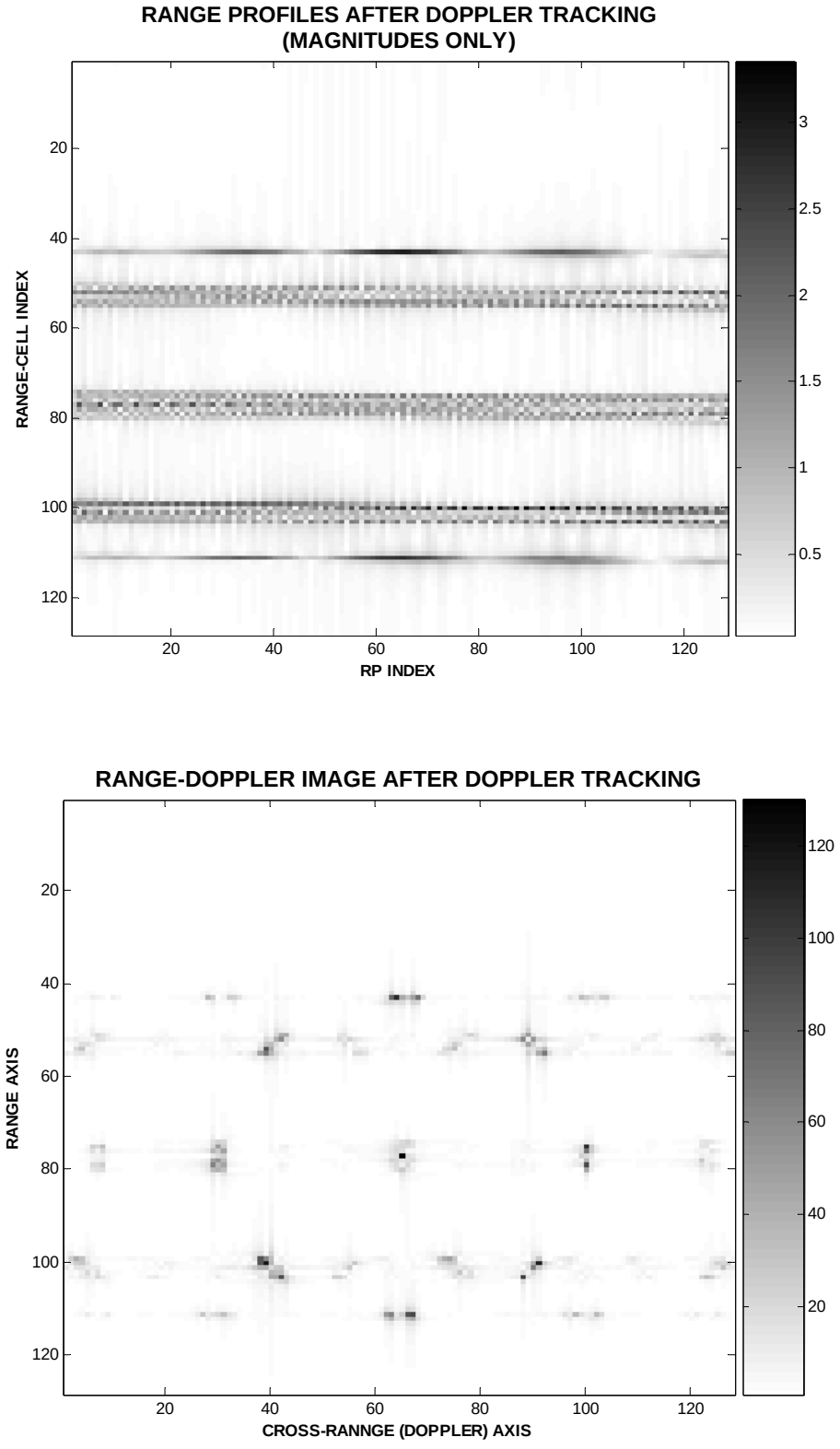

Figure 5.23 RPs and ISAR Image after Doppler Tracking algorithm: Simulation Model-4

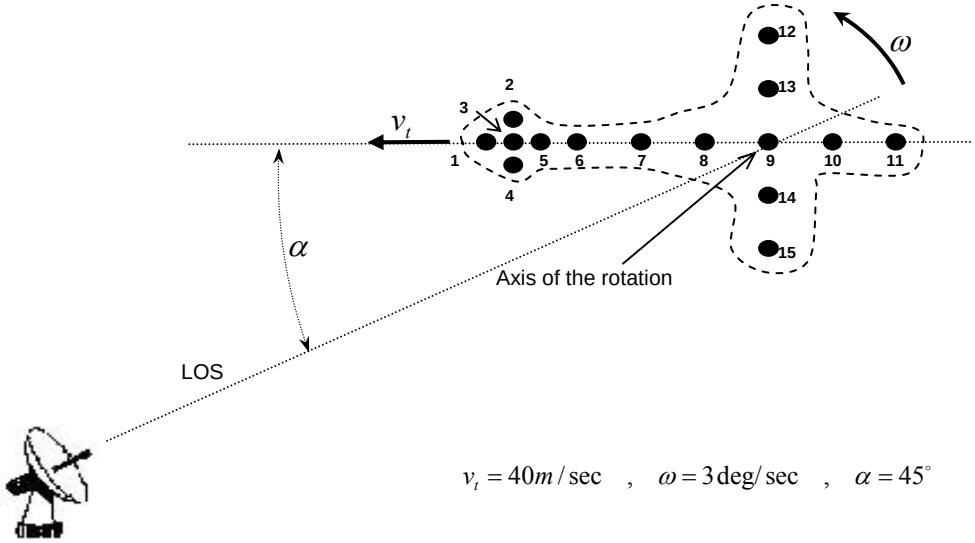

Figure 5.24 Illustration of the Simulation Model-5

Table 5.5 Parameters of Simulation-5

Parameter Description	***Value***
Rotational Velocity, ω *, (degrees/sec)*	3
Translational velocity, v_t *, (m/sec)*	40
Translational Motion Angle, α *, degrees*	45
Δf , frequency-step size, MHz	1
f_0, starting frequency, GHz	3
N , The number of discrete pulses per burst	128
M , The number of bursts	128
β , The effective bandwidth of a burst, MHz	128
T_P , The pulse width, μsec	5
T_{PRI} , The pulse repetition interval (PRI), μsec	50
T, Coherent Integration Time, seconds	0.819

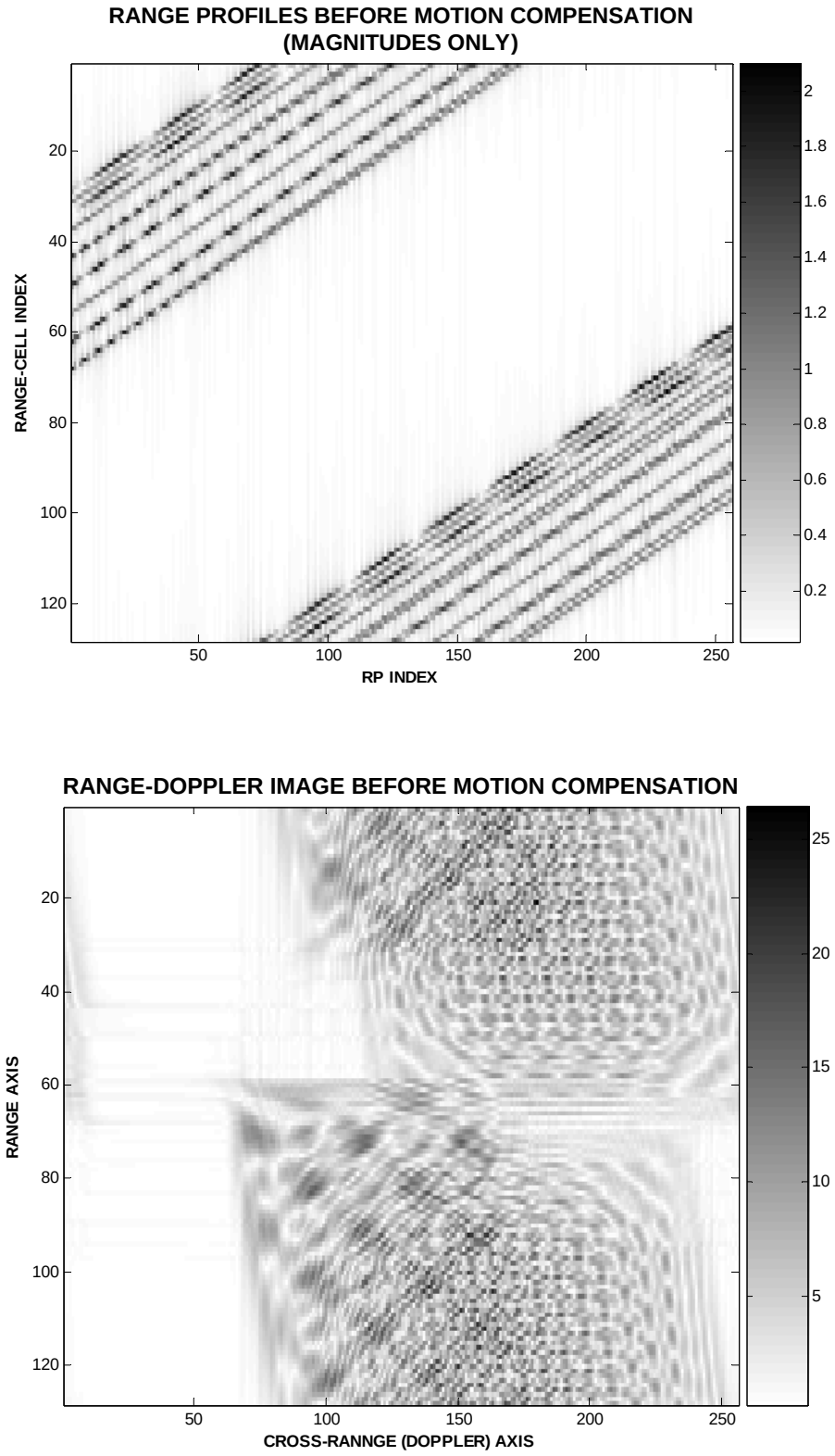

Figure 5.25 Uncompensated RPs and related ISAR Image of Simulation Model-5

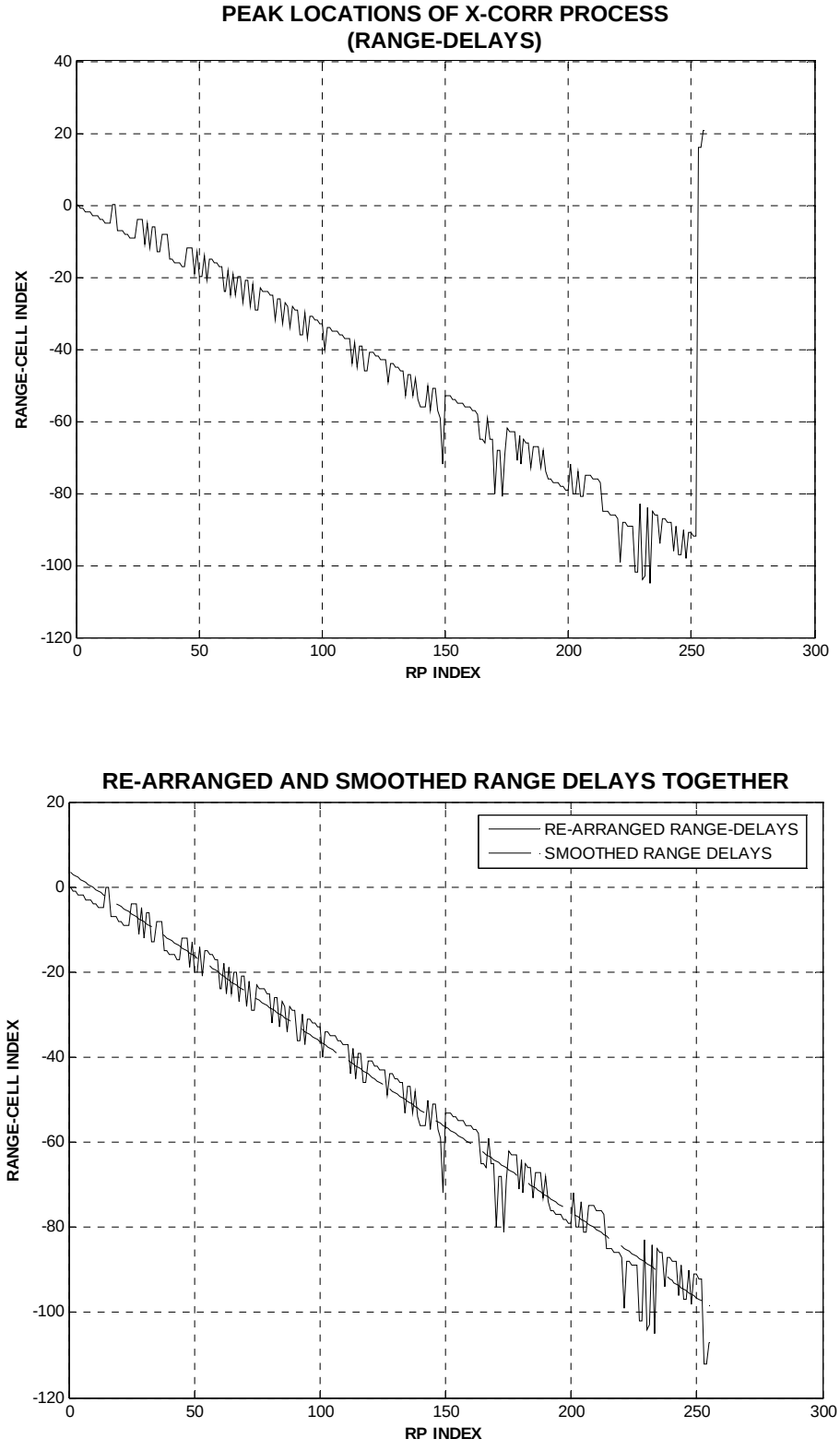

Figure 5.26 Cross-Correlation results of Simulation-5

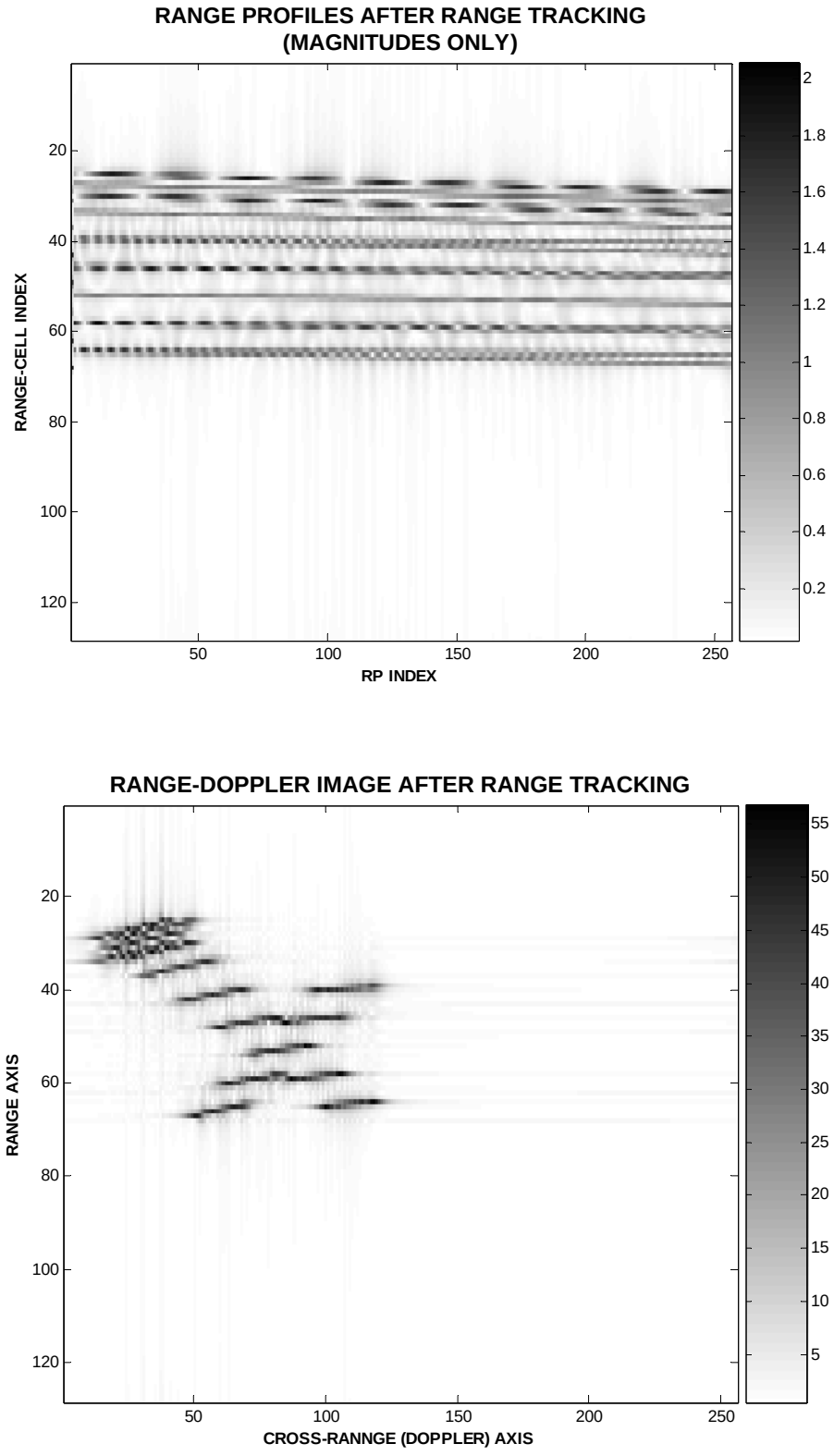

Figure 5.27 RPs and ISAR Image after Range Tracking algorithm: Simulation Model-5

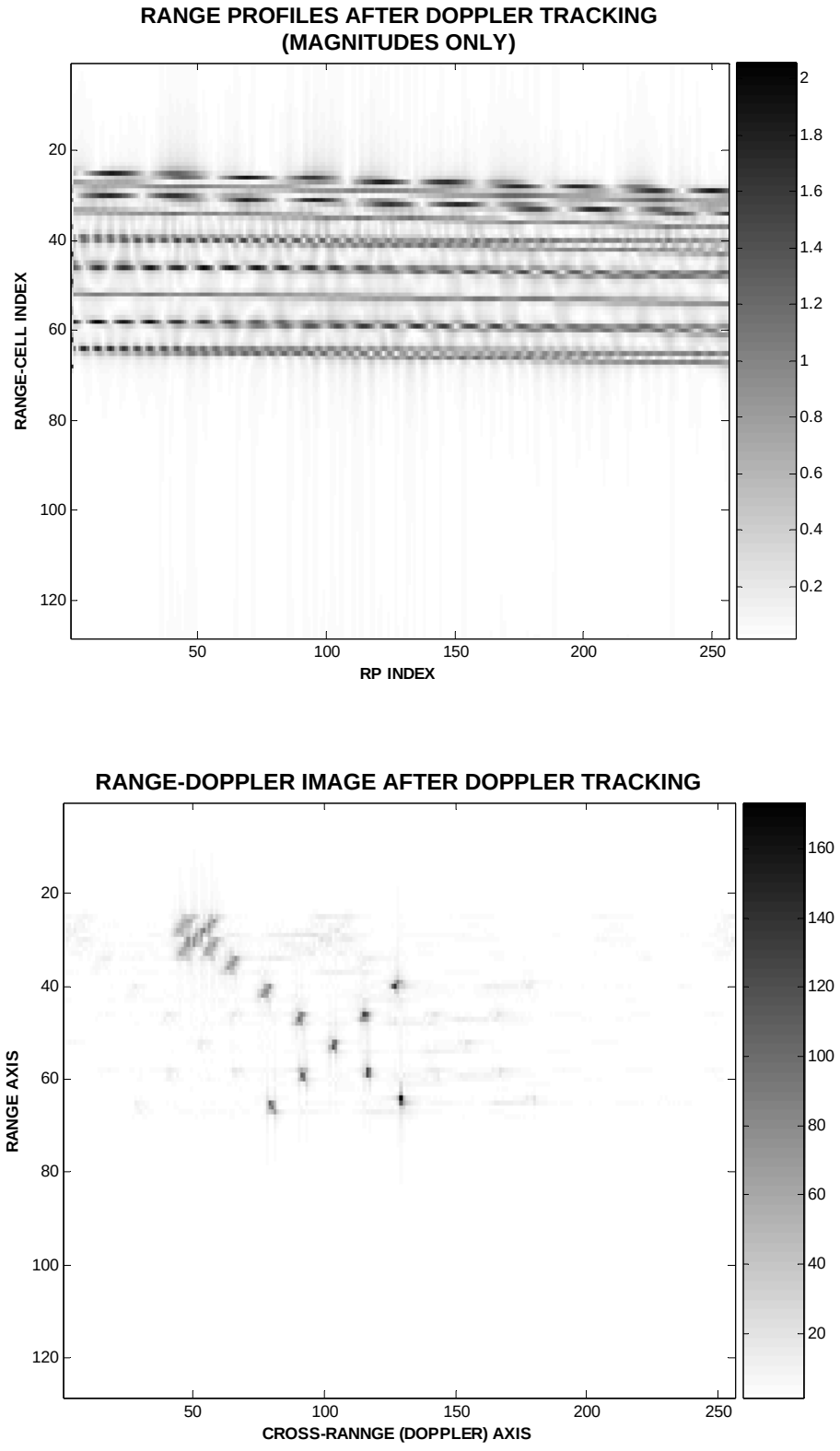

Figure 5.28 RPs and ISAR Image after Doppler Tracking algorithm: Simulation Model-5

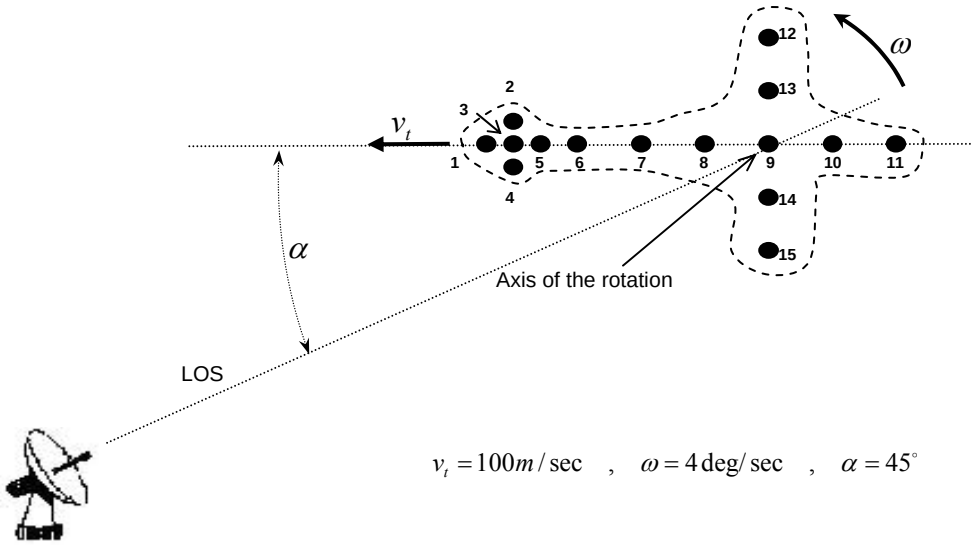

Figure 5.29 Illustration of the Simulation Model-6

Table 5.6 Parameters of Simulation-6

Parameter Description	***Value***
Rotational Velocity, ω *, (degrees/sec)*	4
Translational velocity, v_t *, (m/sec)*	100
Translational Motion Angle, α *, degrees*	45
Δf , frequency-step size, MHz	1
f_0, starting frequency, GHz	3
N , The number of discrete pulses per burst	128
M , The number of bursts	128
β , The effective bandwidth of a burst, MHz	128
T_P , The pulse width, μsec	5
T_{PRI} , The pulse repetition interval (PRI), μsec	50
T, Coherent Integration Time, seconds	0.819

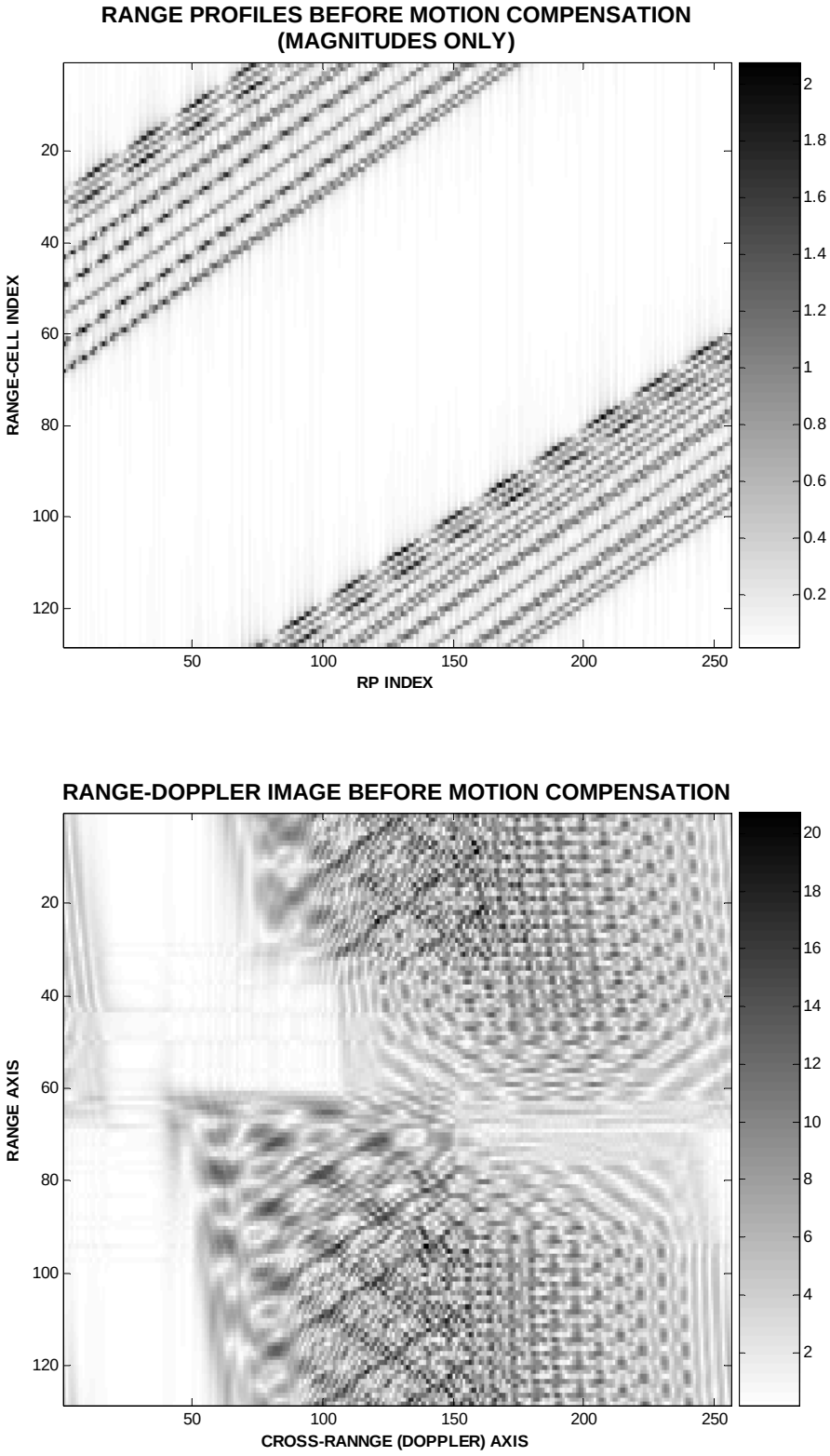

Figure 5.30 Uncompensated RPs and related ISAR Image of Simulation Model-6

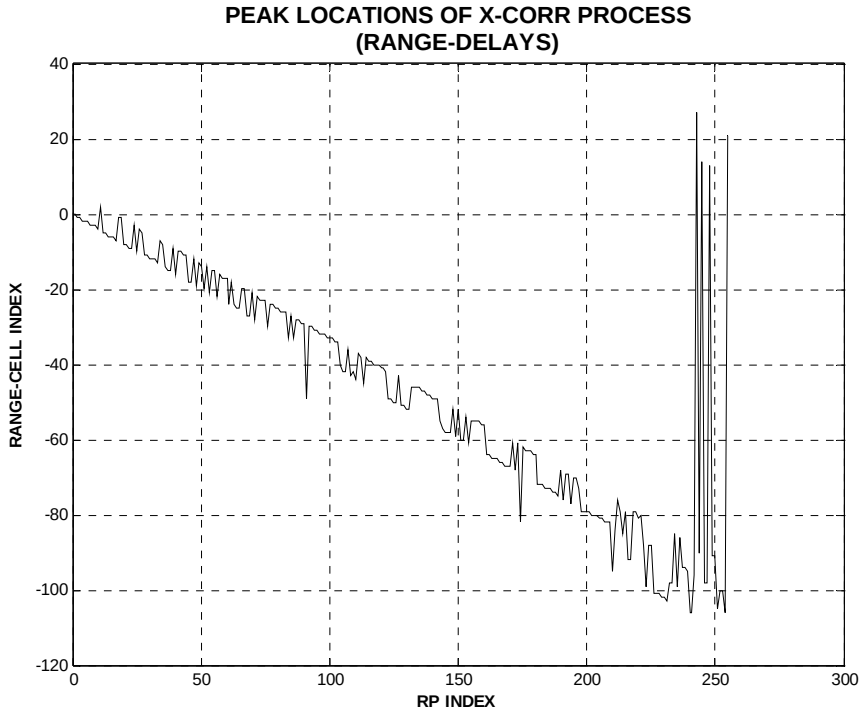

(a)

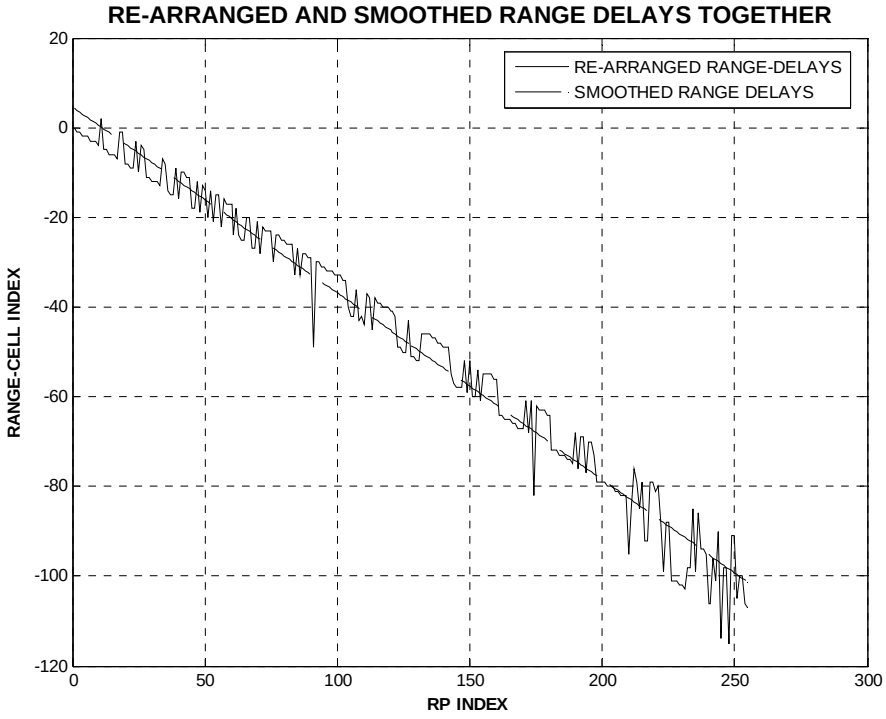

(b)

Figure 5.31 Cross-Correlation results of Simulation-6

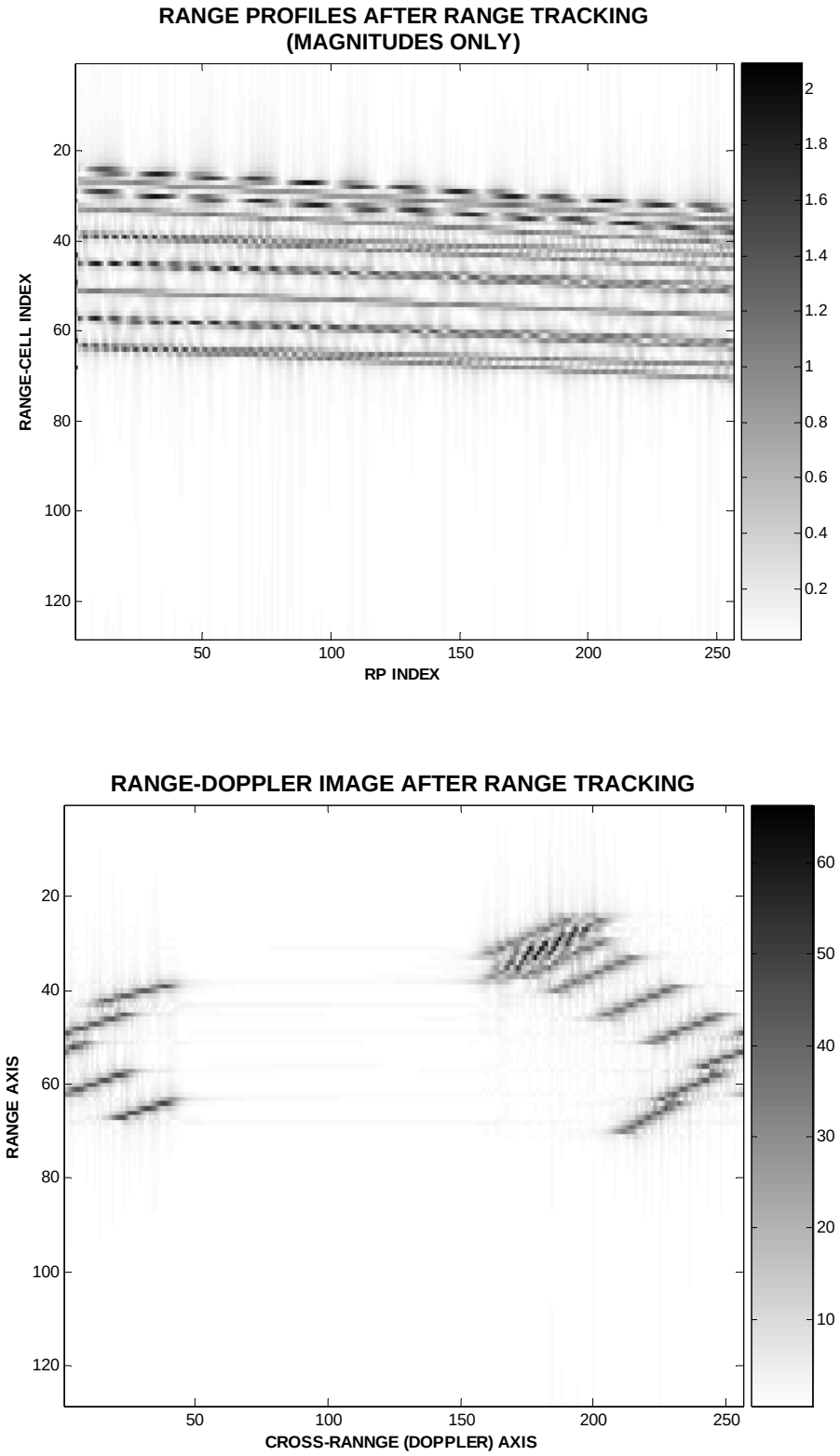

Figure 5.32 RPs and ISAR Image after Range Tracking algorithm: Simulation Model-6

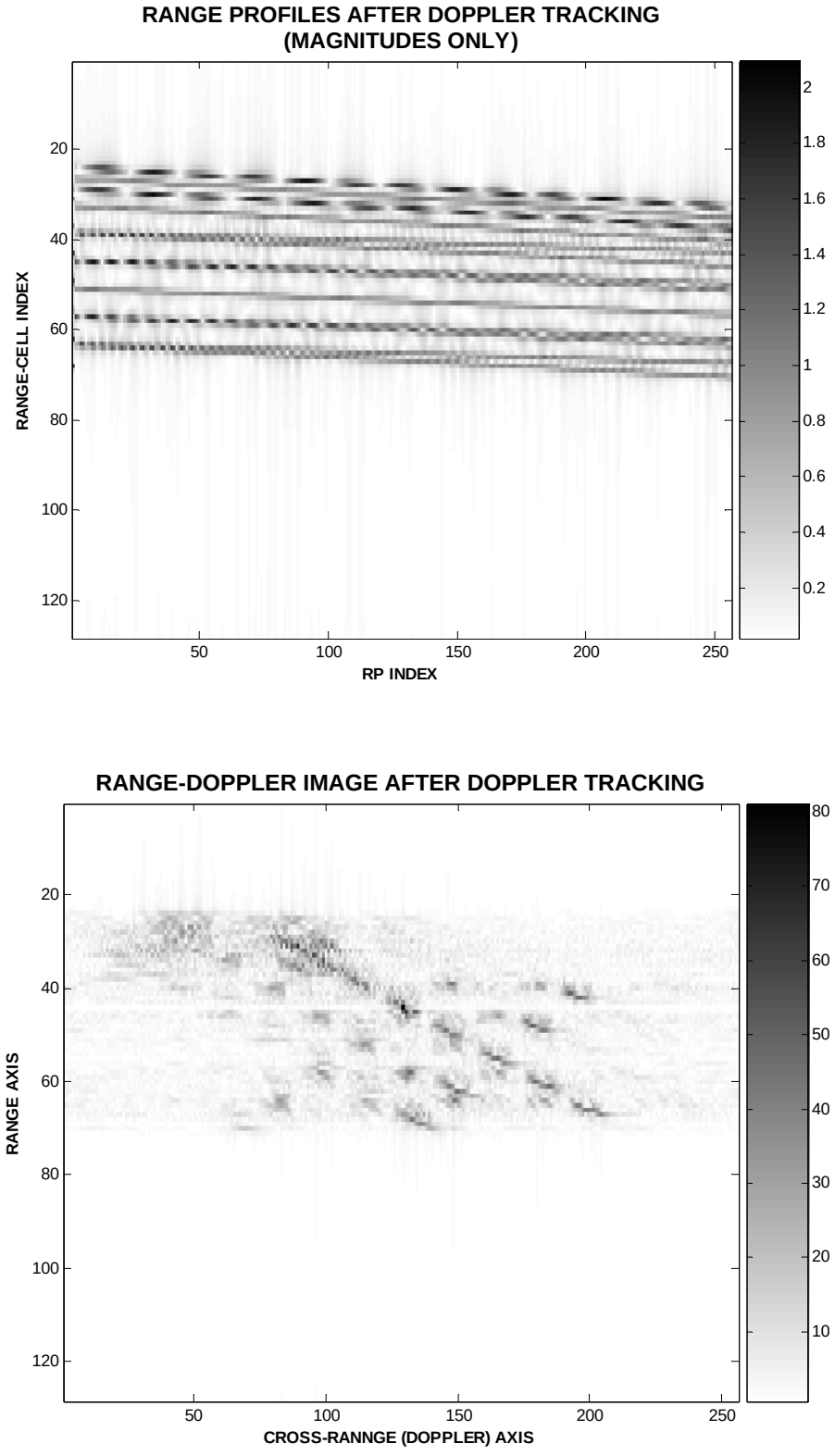

Figure 5.33 RPs and ISAR Image after Doppler Tracking algorithm: Simulation Model-6

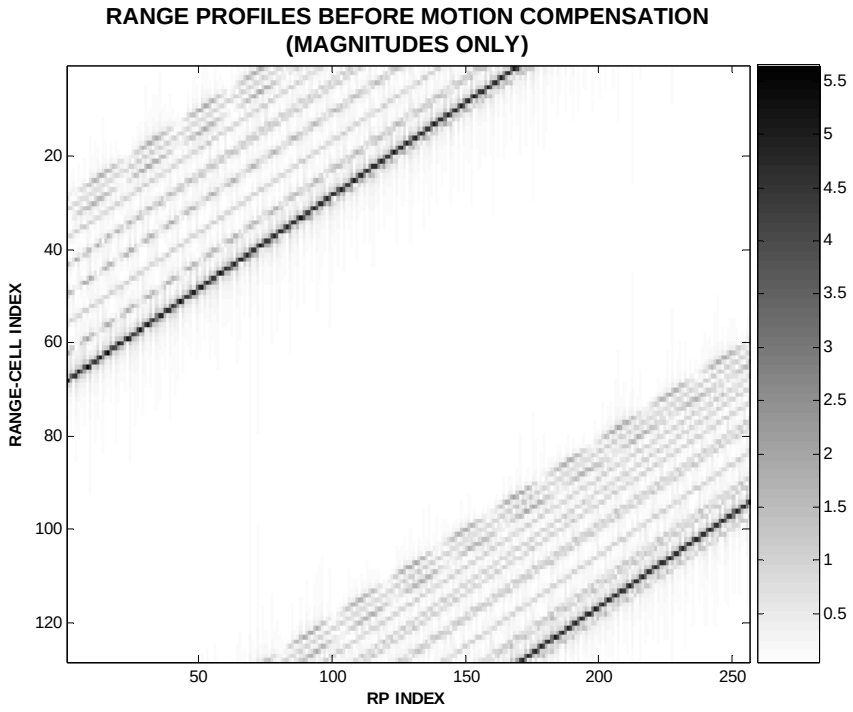

(a)

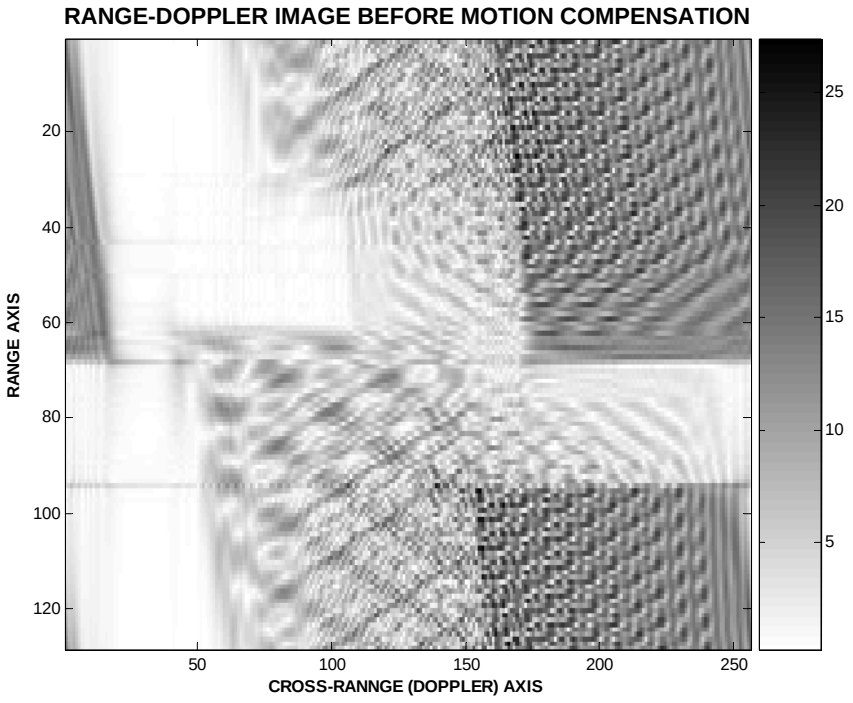

(b)

Figure 5.34 Uncompensated RPs and related ISAR Image of Simulation Model-7

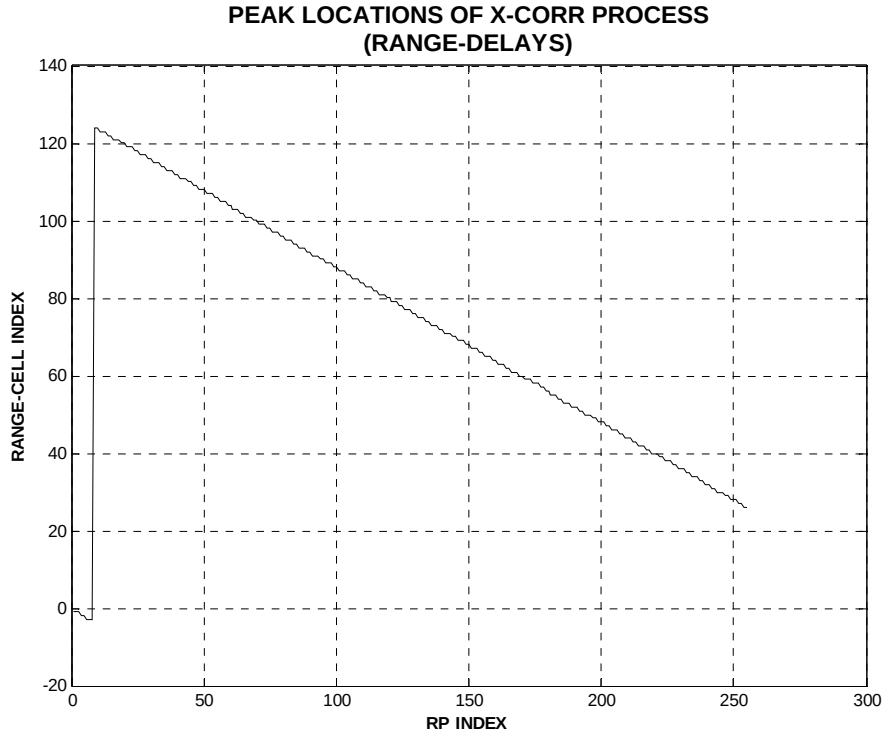

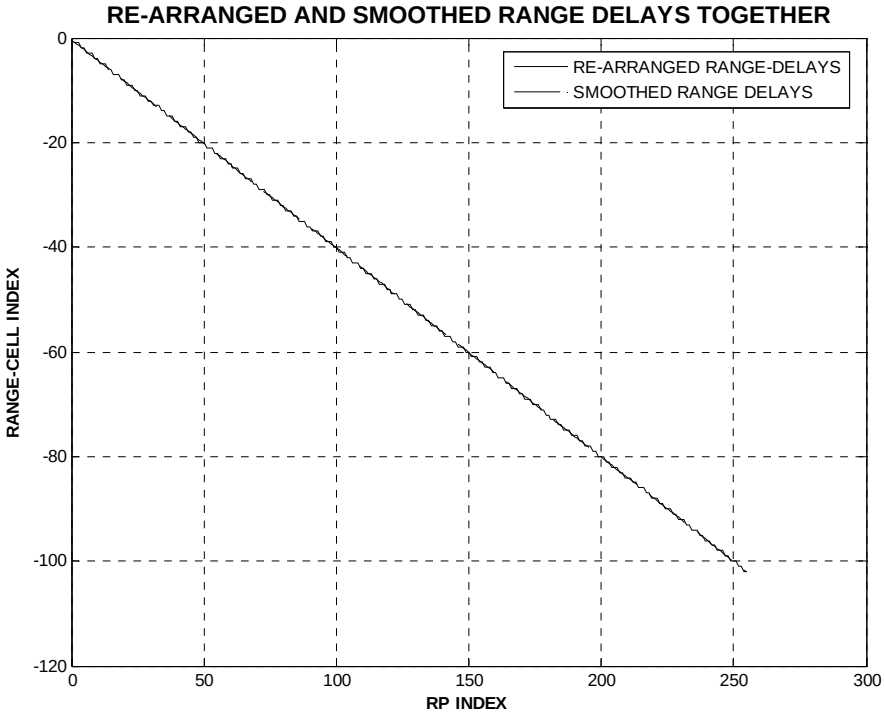

Figure 5.35 Cross-Correlation results of Simulation-7

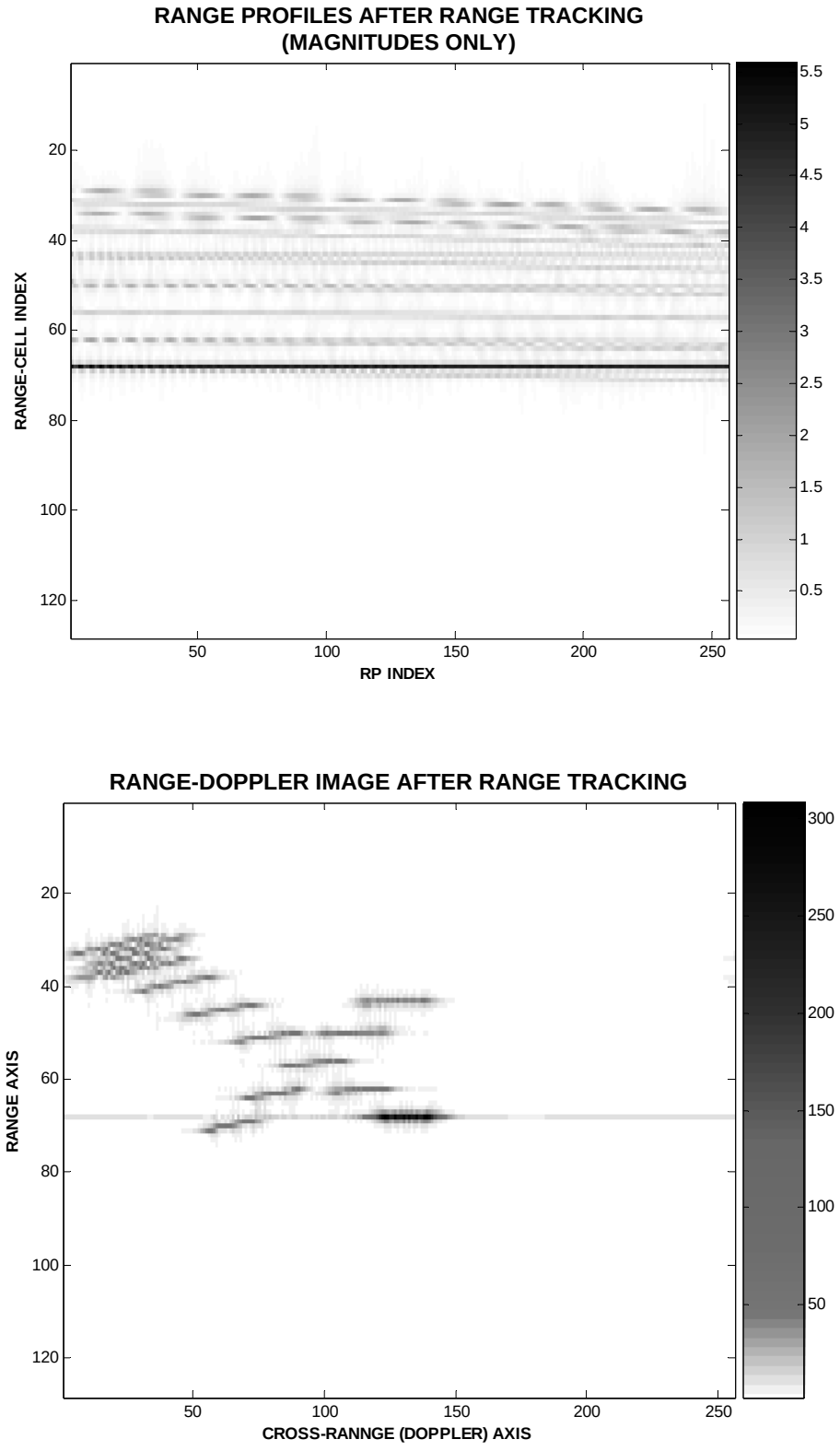

Figure 5.36 RPs and ISAR Image after Range Tracking algorithm: Simulation Model-7

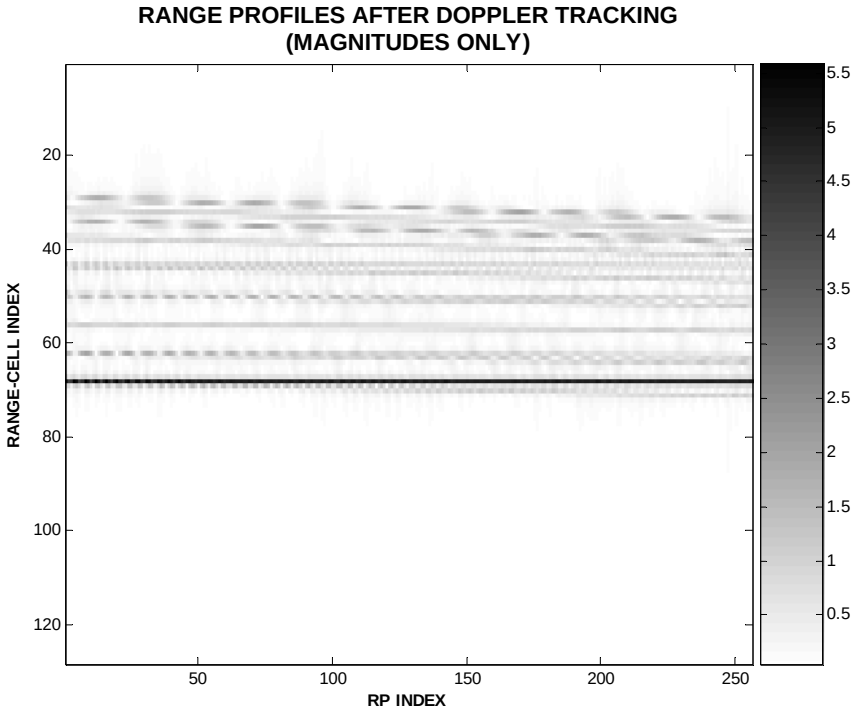

(a)

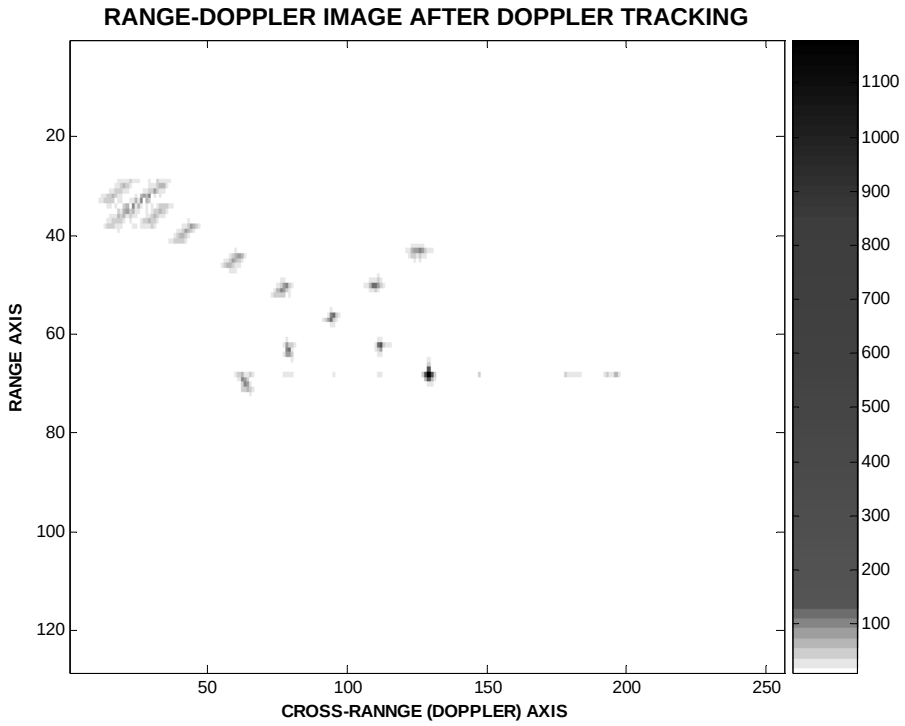

(b)

Figure 5.37 RPs and ISAR Image after Doppler Tracking algorithm: Simulation Model-7

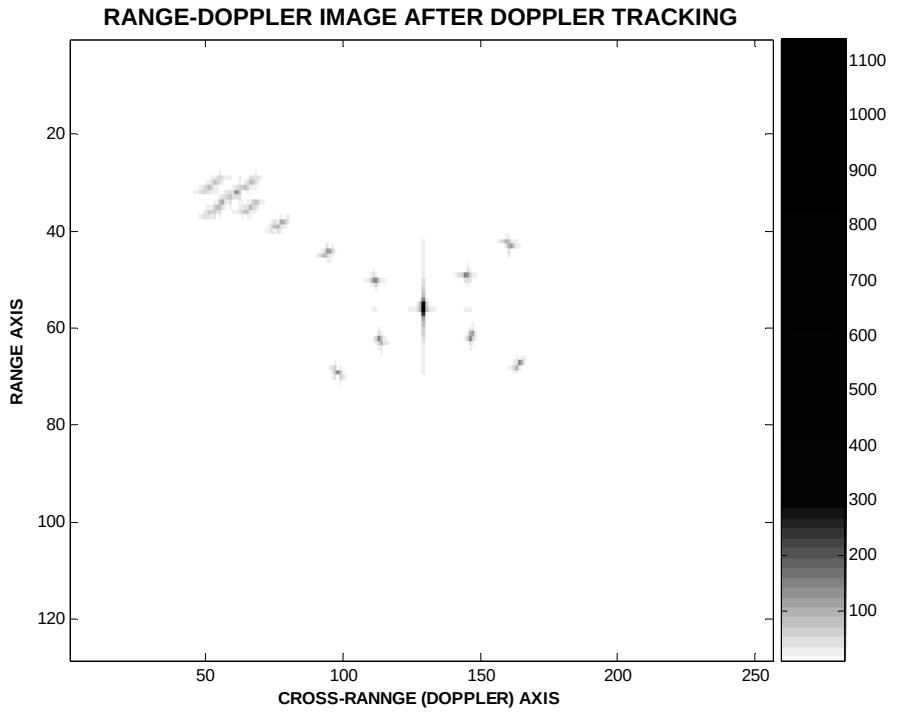

Figure 5.38 ISAR Image with Center Dominant Scatterer: Simulation Model-7

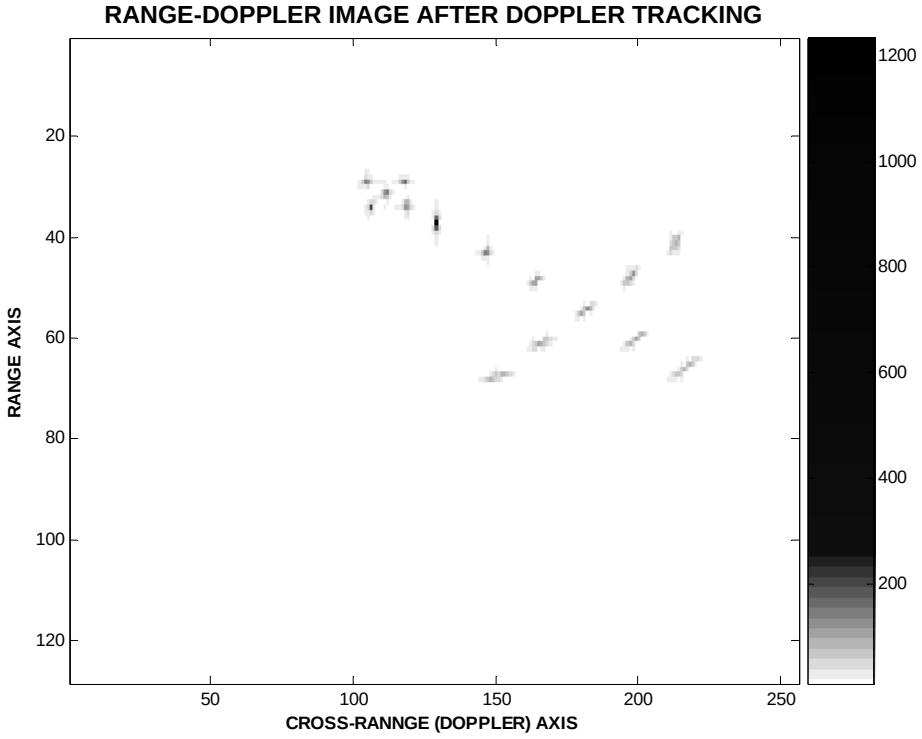

Figure 5.39 ISAR Image with Nose Dominant Center Scatterer: Simulation Model-7

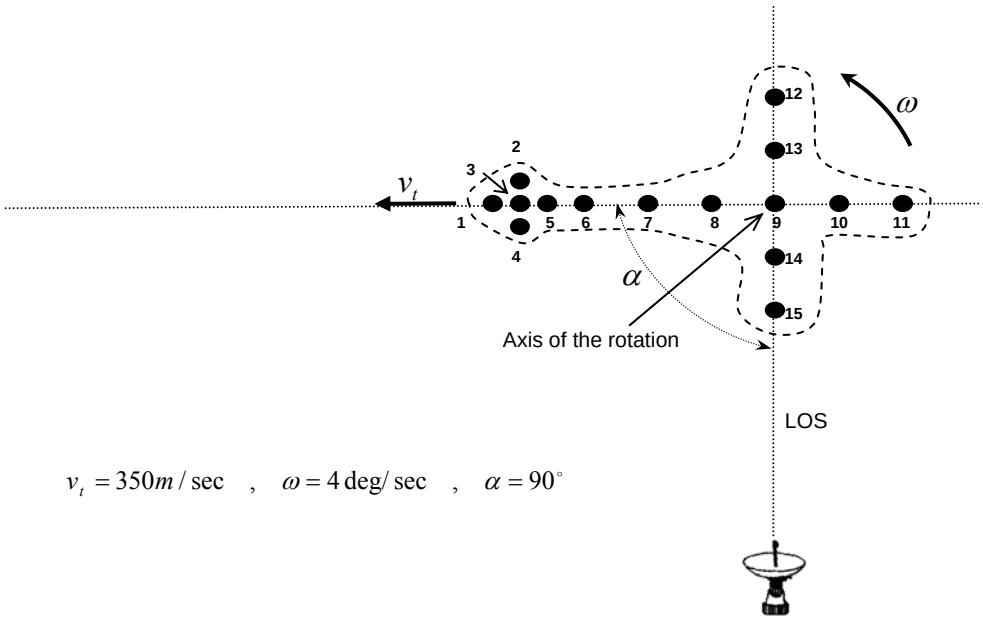

Figure 5.40 Illustration of the Simulation Model-8

Table 5.7 Parameters of Simulation-8

Parameter Description	***Value***
Rotational Velocity, ω *, (degrees/sec)*	4
Translational velocity, v_t *, (m/sec)*	350
Translational Motion Angle, α *, degrees*	**90** ***(Tangential to the RLOS)***
Δf , frequency-step size, MHz	1
f_0, starting frequency, GHz	3
N , The number of discrete pulses per burst	128
M , The number of bursts	128
β , The effective bandwidth of a burst, MHz	128
T_P , The pulse width, μsec	5
T_{PRI} , The pulse repetition interval (PRI), μsec	50
T, Coherent Integration Time, seconds	0.819

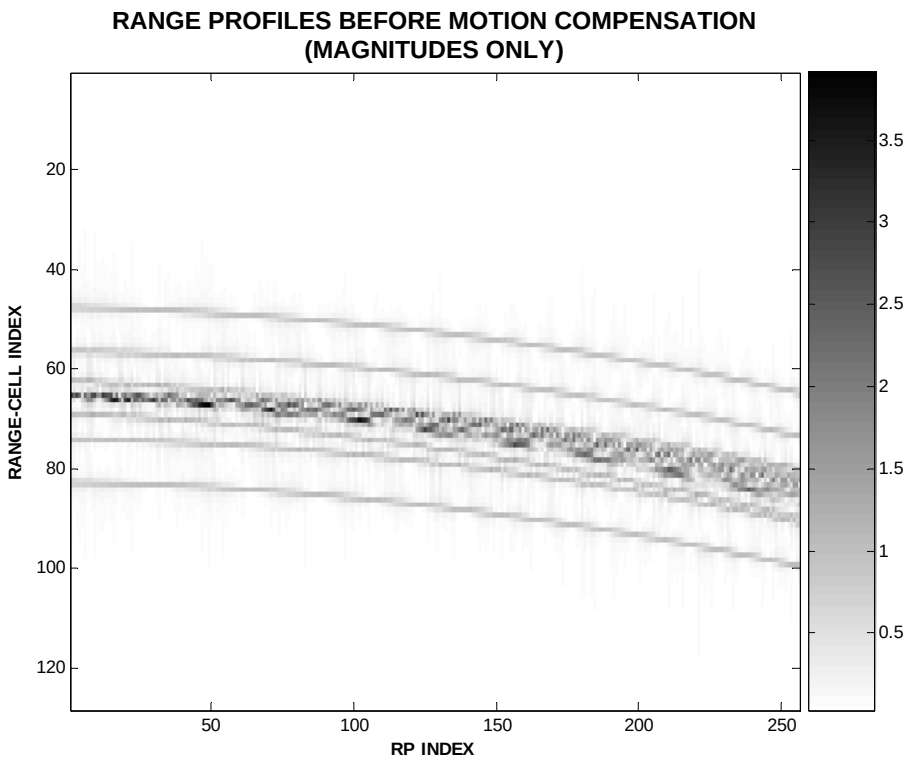

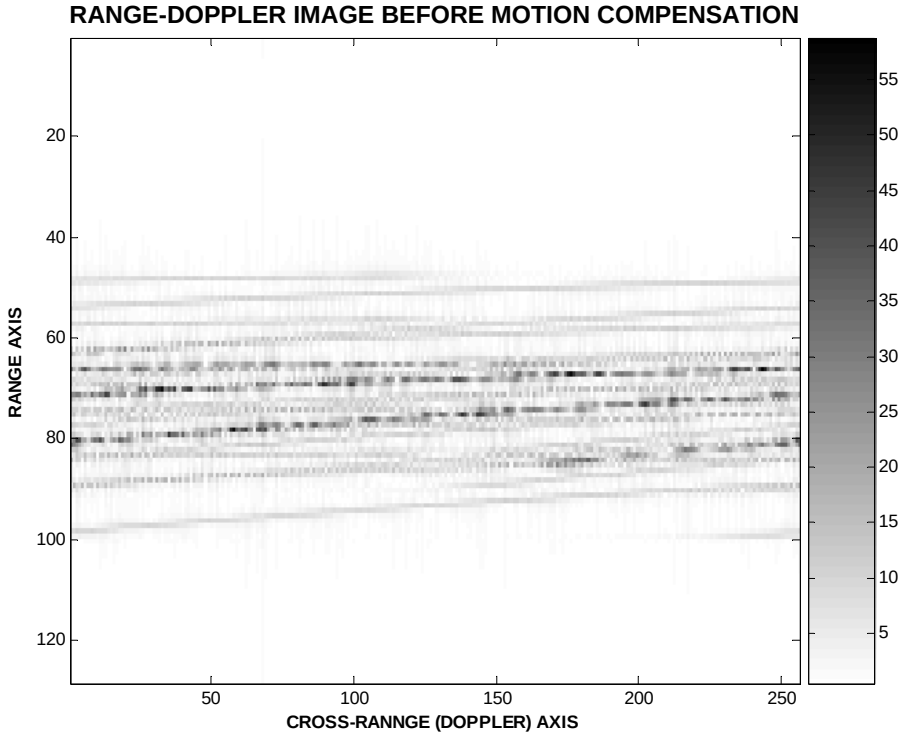

Figure 5.41 Uncompensated RPs and related ISAR Image of Simulation Model-8

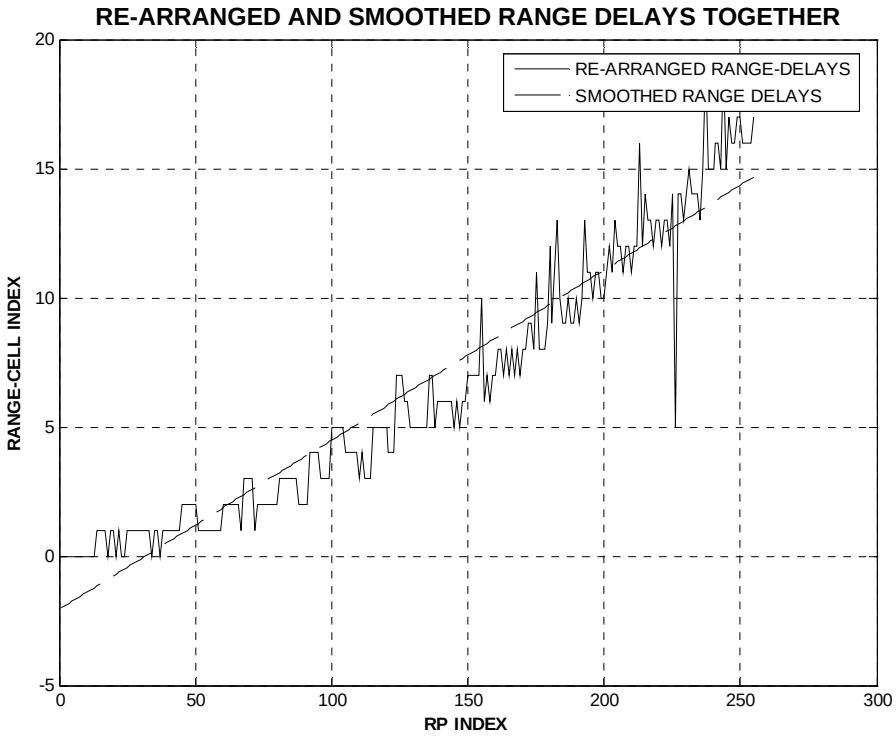

Figure 5.42 Smoothing process results for the 1st order polynomial fitting

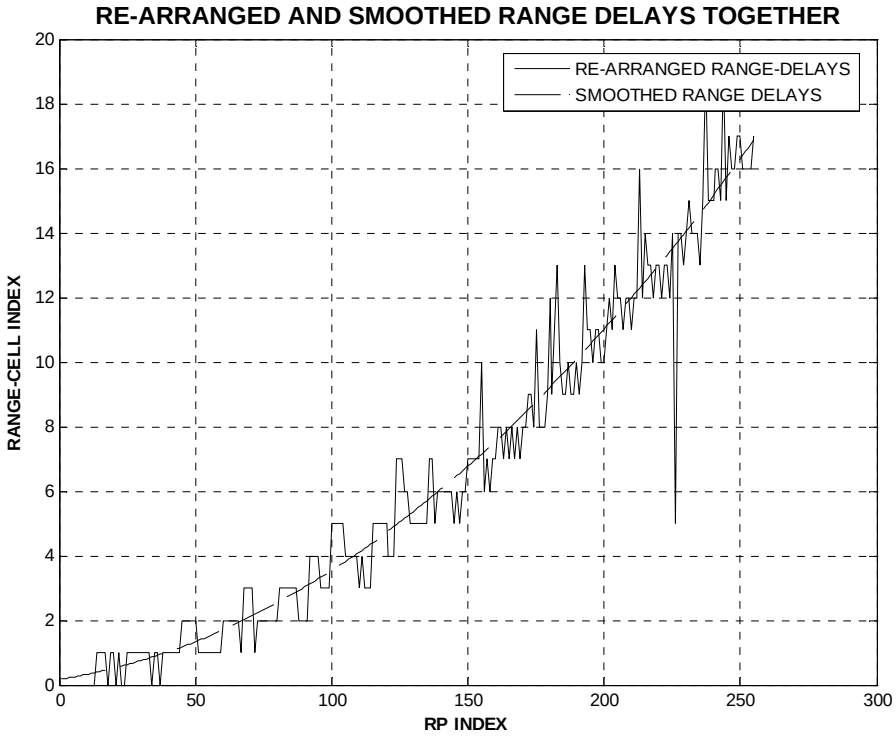

Figure 5.43 Smoothing process results for the 2nd order polynomial fitting

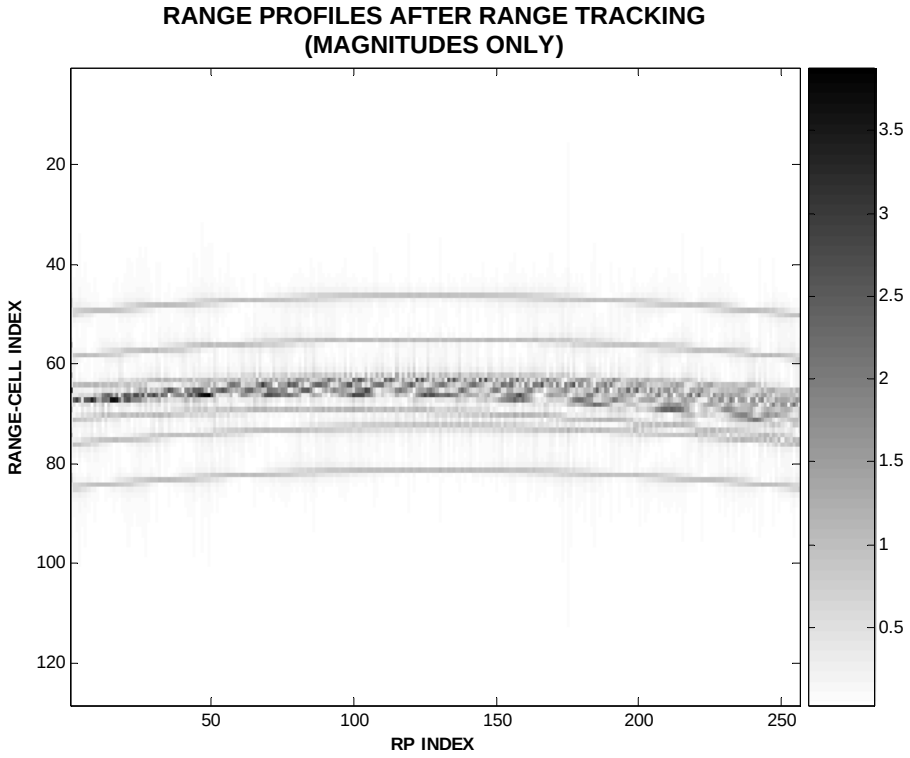

Figure 5.44 Illustration of RPs, after range tracking with 1st order polynomial fitting

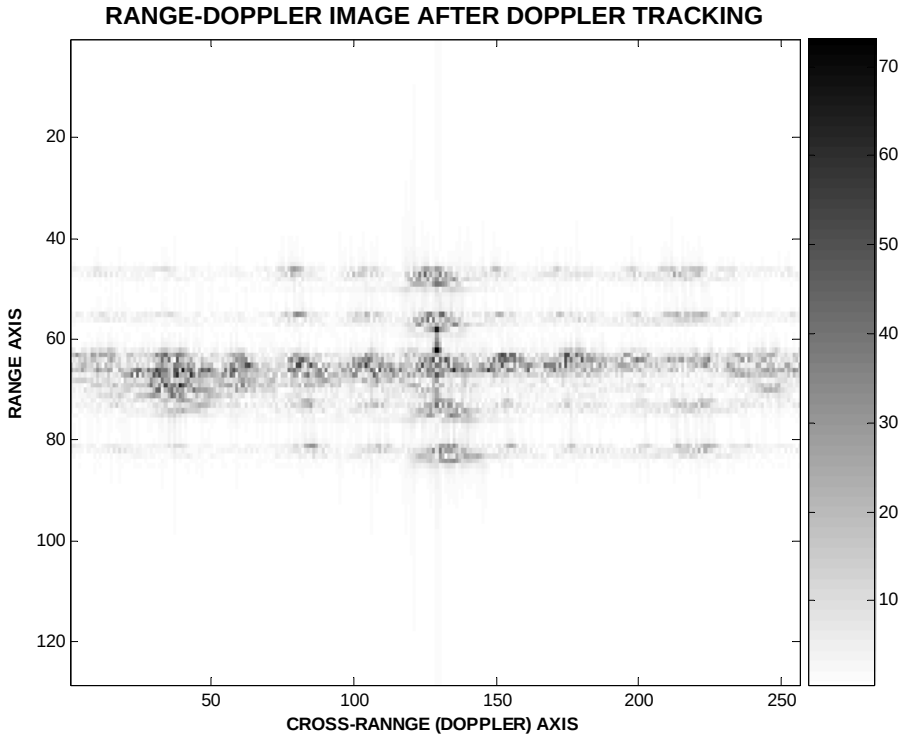

Figure 5.45 Motion compensated image, after Doppler Tracking

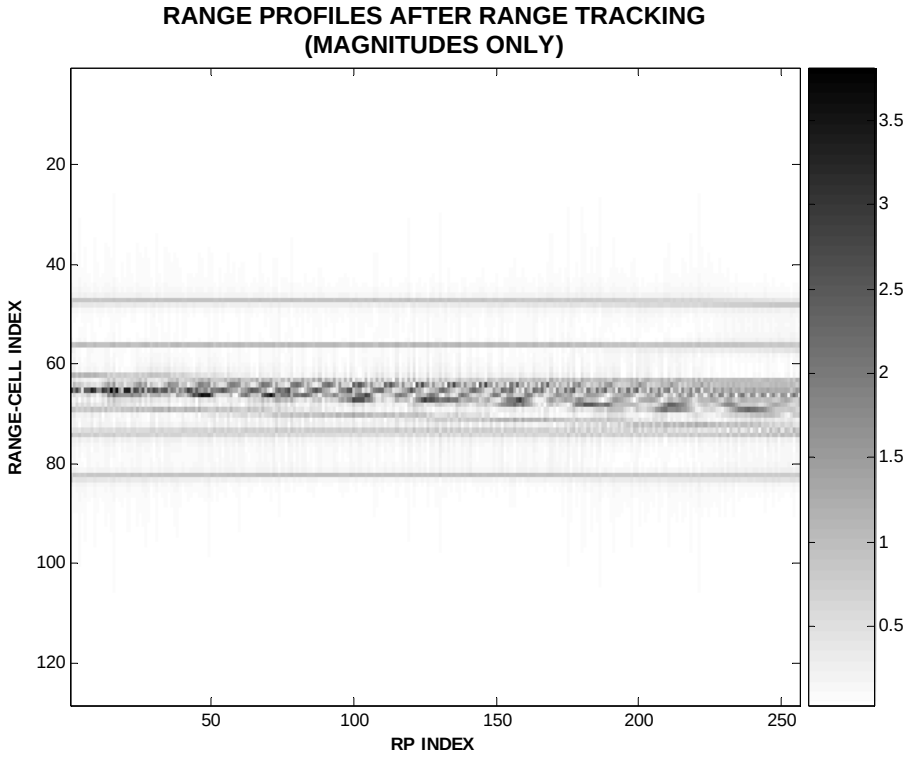

Figure 5.46 Illustration of RPs, after range tracking with 2nd order polynomial fitting

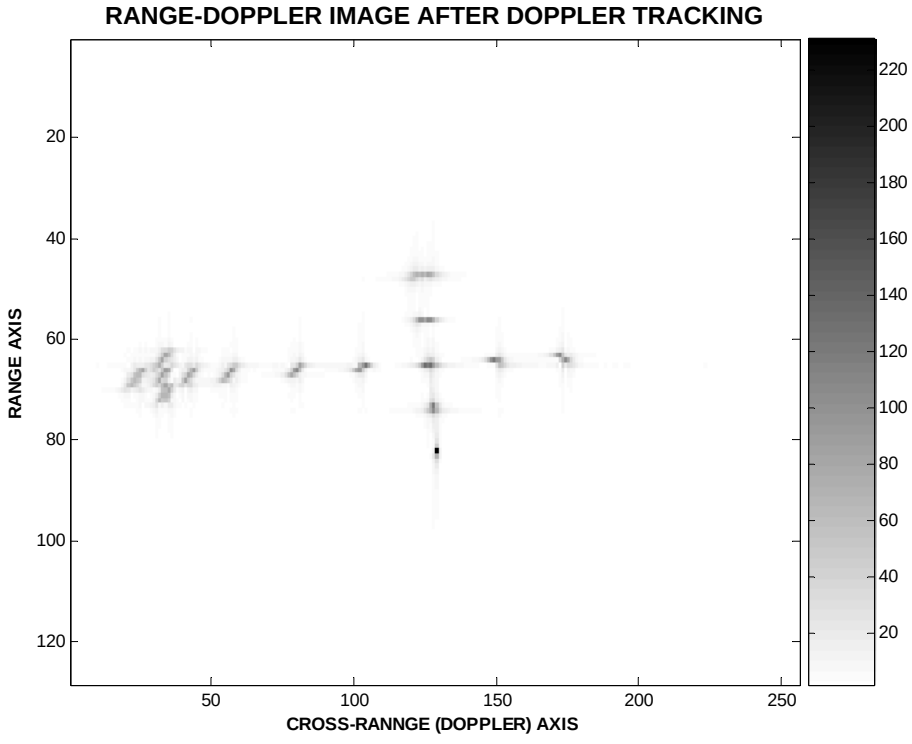

Figure 5.47 Motion compensated image, after Doppler Tracking

CHAPTER 6

APPLICATION OF THE JTFT IN ISAR MOTION COMPENSATION

6.1 Introduction

In this chapter, the use of time-frequency analysis in ISAR motion compensation is presented. As it was discussed in Chapter 4, JTFT technique is applicable to ISAR image generation. Moreover, its advantages and usage area is not restricted with only image generation. TF analysis is also applicable for Doppler tracking and non-uniform rotational motion compensation purposes and it also assists in polar reformatting operation. Hence, after a proper range tracking application, TF analysis could be used, in order to obtain further motion compensation.

TF-based motion compensation is based on the ***multiple prominent point processing*** (***multiple PPP***) technique [15,19] and the ***adaptive TF representation*** [11]. Conventional multiple PPP technique is a complicated, multi-stage motion compensation scheme and it is used in order to achieve both translational and rotational motion compensation. Some introductive information about the traditional multiple PPP is going to be given in section 6.2. Adaptive TF representation is an advanced high resolution JTFT technique and widely used for feature extraction purpose in the ISAR imaging such as JEM (jet engine modulation) [26]. Section 6.3 includes some brief information about the Adaptive TF representation based on [11] and [21]. TF-based motion compensation scheme is presented in section 6.4

according to the [11] and [21]. Simulation results and experimental notes are included in section 6.5.

6.2 A Brief Information About the Conventional Prominent Point Processing Technique

Conventional prominent point processing (PPP) technique could be divided in to two main headings according to [19] and [15] as:

1. Single Prominent Point Processing,
2. Multiple Prominent Point Processing.

Single PPP includes both of the range and the Doppler tracking stages, referring to the selected prominent point's phase and amplitude information. Hence, it could be said that the single PPP technique includes all of the standard motion compensation stages.

Multiple PPP requires two or there prominent scatterers (points) on the RP track of the target. First PP is used in the same manner as it was in the single PPP. Second prominent point is used in order to obtain some information about the rotational motion characteristics of the target. Phase information of the second PP is used in order to estimate and remove the effects of any nonuniformity in the rotation rate of the target. Hence, after second prominent point processing, target is purified from the effects of both translational motion and nonuniform rotational motion. Third prominent point is used in the estimation of the target's rotation rate, ω. This information is necessary for the application of a proper polar reformatting operation, which is a well known and widely used rotational motion compensation scheme but out of the scope of this work.

6.3 A Brief Information About the Adaptive Time-Frequency Representation

The STFT was presented in Chapter 4 as the basic method of TF representation of a signal. Adaptive TF representation is the much more complicated method of TF analysis and uses adaptive normalized Gaussian functions, in order to represent the signal. In the algorithm, the time and frequency resolutions, as well as the time-frequency centers, are adjusted to best match the signal.

The objective of this method is to expand a signal $s(t)$ in terms of normalized Gaussian functions $h_p(t)$ with an adjustable standard deviation σ_p and a time-frequency center (t_p, ω_p) as follows [11]:

$$s(t) = \sum_{p=1}^{\infty} B_p h_p(t) \tag{6.1}$$

where

$$h(t) = (\pi\sigma_p^2)^{-1/4} \exp\left\{-\frac{(t-t_p)^2}{2\sigma_p^2}\right\} \exp\{j\omega_p t\} \tag{6.2}$$

An iterative procedure is needed in order to find the coefficients, B_p. In order to do this, a multi-stage scheme could be included. At the stage $p = 1$, the parameters σ_p, t_p, and ω_p are chosen such that $h_p(t)$ is the basis with the maximum projection onto the signal [11]

$$B_p = \max_{\sigma_p, t_p, \omega_p} \int s_{p-1}(t) h_p^*(t) dt \tag{6.3}$$

where $s_0(t) = s(t)$. For $p > 1$, $s_p(t)$ is the reminder after the orthogonal projection of $s_{p-1}(t)$ onto $h_p(t)$ has been removed from the signal

$$s_p(t) = s_{p-1}(t) - B_p(t) h_p(t) \tag{6.4}$$

This procedure could be iterated in order to generate as many coefficients as needed to accurately represent the original signal.

Actually, *in TF-based motion compensation, the aim is not to parameterize the original signal as a whole but to find the strongest coefficient*. Hence iterative search for the basis functions is going to be omitted.

6.4 Time-Frequency-Based Motion Compensation

Let us assume that the range tracking is applied to the received raw data after RP generation. Then, received echo response within a particular range cell at x could be represented, referring to the Chapter 5.2 and [11], as

$$s_R(t)\big|_x = \sum_{k=1}^{N_k} A_k \exp\left\{-j\frac{4\pi f_0}{c}\left[R(t) + x\cos\theta(t) - y_k \sin\theta(t)\right]\right\} \tag{6.5}$$

where the *x-axis* is the slant-range direction, f_0 is the center frequency of the radar and t denotes the dwell time. N_k is used to state the number of the point-scatterers within the same range cell, at the slant-range position x. A_k is the magnitude of the k th point scatterer. y_k is the cross-range position of the k th point-scatterer. $R(t)$ describes the residual uncompensated translation displacement within the range-cell. $\theta(t)$ is the rotation angle as a function of dwell time. Equation (6.5) could be rewritten by using (5.4) and (5.5) as follows [11],

$$s_R(t)\big|_x = \sum_{k=1}^{N_k} A_k \exp\left\{-j\frac{4\pi f_0}{c}\left[(R_0 + x) + (V_R + \Omega y_k)t + \frac{1}{2}(a_R - \Omega^2 x + \gamma y_k)t^2 + \ldots\right]\right\} \tag{6.6}$$

The constant phase term does not contribute to the imaging process, hence it could be ignored. If $R(t) = R_0, \theta(t) = \Omega(t)$ and $(\Omega t)^2$ is negligible, which does mean no translational motion, and only a small amount of rotational motion exists, the phase function is a pure linear function of time. This is the ideal case when a simple Fourier

transform will focus the point-scatterers to their respective cross-range (y_k) positions in the cross-range dimension [11].

Phase Estimation Using TF Projection

Figure 6.1 illustrates STFT analysis of the dominant scatterer's range-cell of the Simulation Model-7 of Chapter 5.6. Black colored track belong to the dominant scatterer and means that there is only one scatterer in this range-cell: Number of the evident black lines are directly related to the number of scatterers in that range-cell. This important illustration represents the relation between the TF-based signal analysis results and the Equation (6.6). It is observed that the quadratic phase term in the Equation (6.6) behaves like a linear chirp in the time-frequency plane. It could be stated that *the displacement and the slope* of the straight line in Figure 6.1 is related to the *linear and quadratic coefficients* of its phase function in Equation (6.6), respectively.

The task at hand is to determine these coefficients or the dominant point-scatterer within the range cell. We consider here a time-frequency procedure extended from the adaptive Gaussian representation. In our present problem, the point-scatterers have already been aligned in range. We do, however, add an additional quadratic (and possibly higher-order) phase term in the basis function as follows [11]:

$$h_p(t) = \exp -\left[j2\pi (f_{D_0} t + \frac{1}{2} f_{D_1} t^2 + ...) \right] \tag{6.7}$$

The above set of bases can be thought of as a collection of unit chirps, each with a different displacement and chirp. We carry out a search procedure (as in the adaptive spectrogram) to determine the best basis by projecting the radar signal onto all possible bases of the form (6.7). We search the parameters $(f_{D_0}, f_{D_1}, ...)$ that satisfy [11]

$$< f_{D_0}, f_{D_1}, ... >= \arg\max \left| \int s_R(t)\big|_x h_p^*(t) dt \right| \tag{6.8}$$

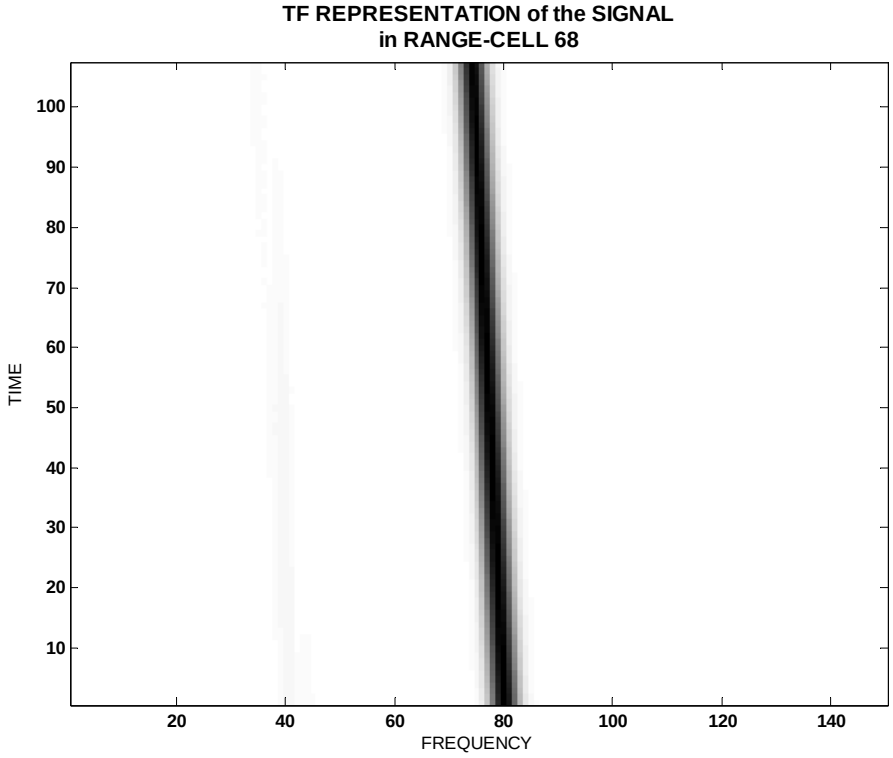

Figure 6.1 TF representation of the dominant scatterer's range-cell in Simulation-7

Equation (6.8) implies that the parameters in the phase function are estimated to give the maximum projection from the radar data onto the basis function. In the adaptive spectrogram, this procedure is iterated to try to parameterize the total signal. However, in the present application, only the strongest point-scatterer within a range cell is searched. We choose to use only the dominant scatterer in a range cell in order to avoid estimation errors for the weaker scatterers. The search for the linear coefficient f_{D_0} can be accomplished by using the fast Fourier transform. Then only a 1D search is required to find f_{D_1}, the quadratic coefficient. In terms of performance, the algorithm is equivalent to picking out the strongest line in the time-frequency plane with the full Doppler resolution offered by the total coherent processing interval. Also, this projection algorithm applies even when there is not an isolated, dominant point-scatterer in the range cell [11].

Motion Error Elimination

With the AJTF procedure for estimating the phase of individual point scatterers in hand, the next task is to eliminate those quadratic phase terms for all the scatterers. We consider here the case when $(\Omega t)^2 << 1$ so that this term can be neglected in the phase. This is usually a good approximation for high-frequency radars (X-band and above), as the angular window needed, to form an image with sufficient cross-range resolution is quite small in absolute terms (i.e., a few degrees). With the approximation, (6.5) becomes [11]

$$s_R(t)\big|_x = \sum_{k=1}^{N_k} A_k \exp\left\{-j\frac{4\pi f_0}{c}\left[(V_R + \Omega y_k)t + \frac{1}{2}(a_R + \gamma y_k)t^2\right]\right\} \tag{6.9}$$

We observe that the quadratic phase coefficient consists of two terms. The first term, $\frac{1}{2}a_R t^2$, represents the translation motion error and is independent of the cross-range y. The second cross-range-dependent term, $\frac{1}{2}\gamma y_k t^2$, represents the rotational motion error. We first carry out the translation motion compensation by extracting the phase of a prominent point-scatterer located at (x_1, y_1) using the AJTF search. The estimated phase is denoted as [11]

$$\exp\left[-j2\pi(f_{D_{01}}t + \frac{1}{2}f_{D_{11}}t^2)\right] \tag{6.10}$$

We then multiply the radar data by the conjugate of (6.10). Based on the model, the phase of an arbitrary point-scatterer at (x_i, y_i) on the target is reduced to

$$\exp\left\{-j\frac{4\pi f_0}{c}\left[(y_i - y_1)(\Omega t + \frac{1}{2}\gamma t^2)\right]\right\} \tag{6.11}$$

As can be seen from (6.11), the translation error has been removed from the data and only rotational motion error remains. The reference point (x_1, y_1) serves as the center of the rotational motion [11,21].

Next we carry out the rotational motion compensation by extracting the phase of a second prominent point-scatterer at (x_2 , y_2):

$$\exp\left[- j2\pi (f_{D_{02}} t + \frac{1}{2} f_{D_{12}} t^2) \right] \tag{6.12}$$

By comparing (6.12) to (6.11), we see that the extracted phase gives the desired relationship between the rotation angle and the dwell time (up to a proportionality constant):

$$\theta(t) = \Omega t + \frac{1}{2}\gamma t^2 \quad \propto \quad f_{D_{02}} t + \frac{1}{2} f_{D_{12}} t^2 \tag{6.13}$$

Once this relationship is found, it is possible to reformat the radar data to eliminate the quadratic phase dependence on dwell time. The original radar data is uniformly sampled in dwell time t. We interpolate the data based on (6.11) such that it becomes uniformly sampled in angle θ. After the reformatting, the phase of each point-scatterer is linearly related to the angle and the residual motion due to nonuniform rotation rate is thus removed from the data [11,21].

6.5 TF-Based Motion Compensation Applications

In this section, some examples of TF-based motion compensation are going to be presented.

First simulation is the cross-shaped target. All of the simulation parameters are chosen same as the Simulation Model-7 of Chapter 5.6. Description of the model and the related parameters are given in Figure 6.2 and Table 6.1 respectively. The tail scatterer, 11th point scatterer, is chosen as the dominant scatter, which is three times stronger than the other (uniform) scatterers. Figure 6.3 illustrates the target's range profile track and related ISAR image before motion compensation. Figure 6.4 and Figure 6.5 show the ISAR image of the target model, after the cross-correlation and DSA based range and Doppler tracking, respectively. Initial STFT analysis of the

strongest range-cell (corresponds to the first prominent point in conventional PPP algorithm) is given in Figure 6.6. Figure 6.7 and Figure 6.8 illustrate the STFT analysis of the same range-cell after phase compensation, according to the f_{D_0} and f_{D_1} parameters, which corresponds to the displacement and slope parameters of the chirp-like signal in Figure 6.6, respectively. Hence, resultant ISAR image of the TF-based Doppler tracking is illustrated in Figure 6.9. In this simulation case, it could be said that the DSA (Figure 6.5) and TF-based (Figure 6.9) Doppler tracking methods provide nearly same degree of phase compensation. Power of TF-based could be observed in Figure 6.10, which is the result of TF-based non-uniform rotational motion compensation, according to the selected second prominent point. Resolvable noise scatterers (1^{st}, 2^{nd}, 3^{rd}, 4^{th} and 5^{th} scatterers) are obtained only after TF-based non-uniform rotational motion compensation.

The second example is the simulated Boeing-727 model [12]. Figure 6.11 is the illustration of the simulation model without any motion added in. Figure 6.12 illustrates the ISAR image of the simulation model after cross-correlation based range tracking. Initial STFT analysis of the strongest range-cell (corresponds to the first prominent point in conventional PPP algorithm) is given in Figure 6.13. Figure 6.14 and Figure 6.15 illustrate the STFT analysis of the same range-cell after phase compensation, according to the f_{D_0} and f_{D_1} parameters, which corresponds to the displacement and slope parameters of the chirp-like signal in Figure 6.13, respectively. Figure 6.16 and Figure 6.17 show the resultant ISAR images after TF and DSA based Doppler tracking processes, respectively. It is concluded that the TF-based Doppler tracking results in better compensation of the tail and fuselage scatterers. Figure 6.18 illustrates the excellent result of the non-uniform rotational motion compensation according to the second prominent point. It is concluded that two prominent point focusing has made the image of the simulated B727 target well focused, by a comparison of Figure 6.11 and Figure 6.18.

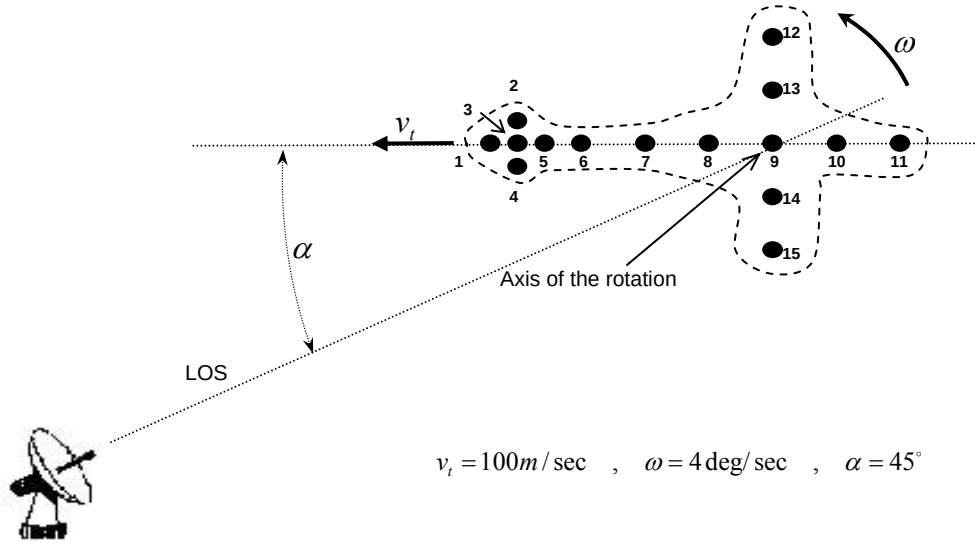

Figure 6.2 Illustration of the Simulation Model-1

Table 6.1 Parameters of Simulation-1

Parameter Description	***Value***
Rotational Velocity, ω *, (degrees/sec)*	4
Translational velocity, v_t *, (m/sec)*	100
Translational Motion Angle, α *, degrees*	45
Δf , frequency-step size, MHz	1
f_0, starting frequency, GHz	3
N , The number of discrete pulses per burst	128
M , The number of bursts	256
β , The effective bandwidth of a burst, MHz	128
T_P , The pulse width, μsec	5
T_{PRI} , The pulse repetition interval (PRI), μsec	50
T, Coherent Integration Time, seconds	0.819

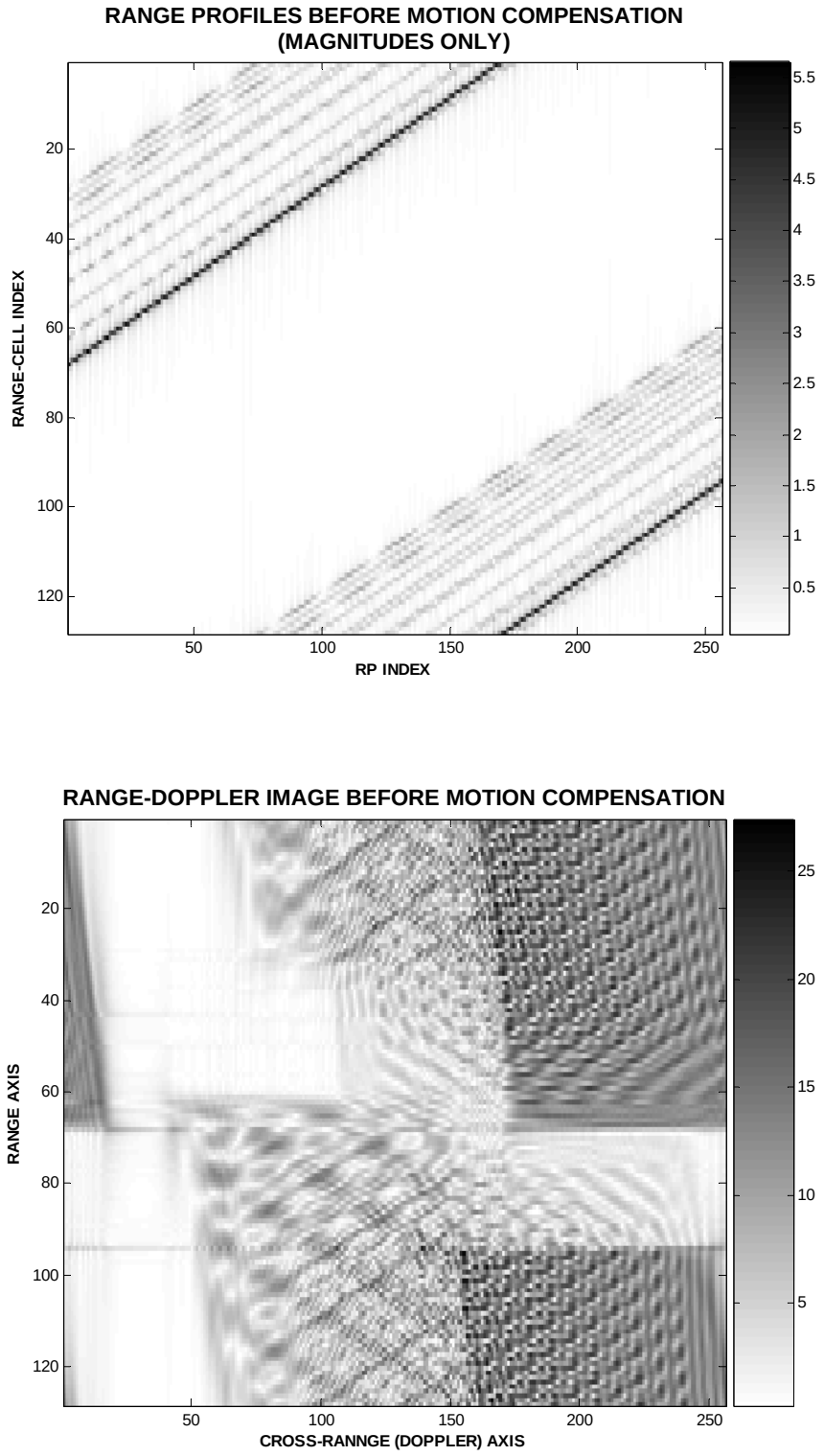

Figure 6.3 Uncompensated RPs and related ISAR Image of Simulation Model-1

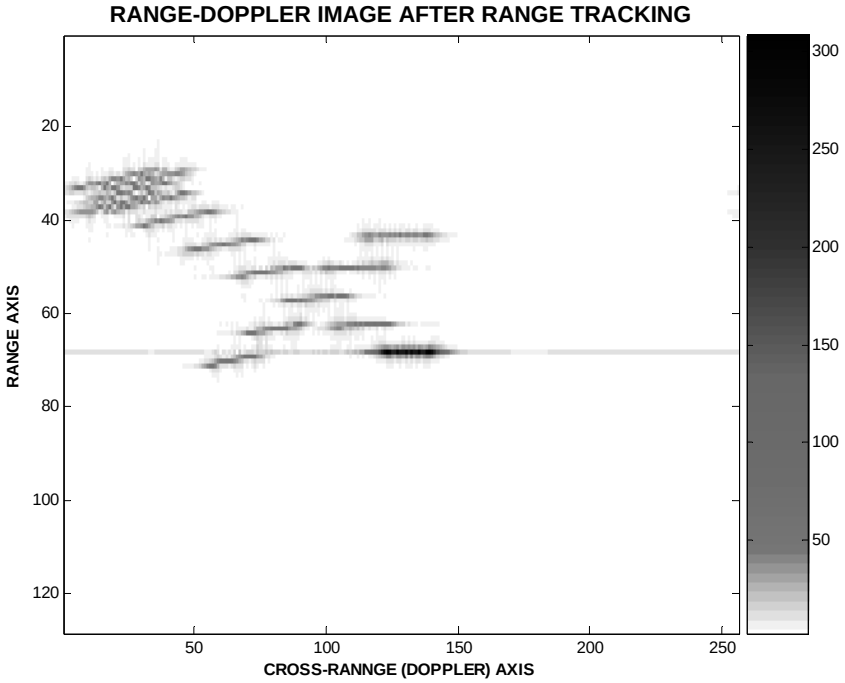

Figure 6.4 ISAR Image after Range Tracking

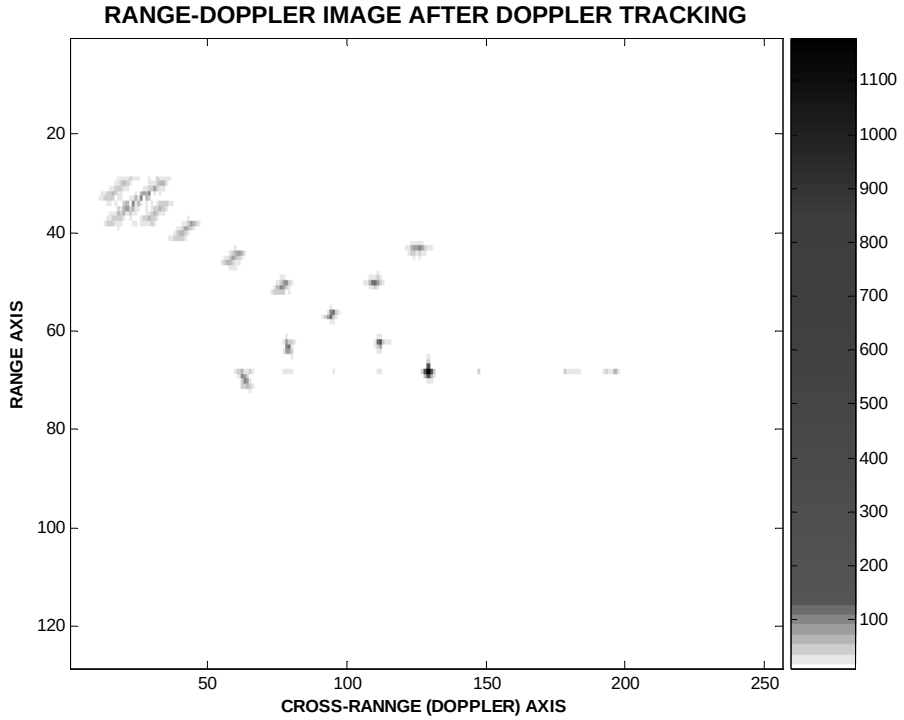

Figure 6.5 ISAR Image after DSA Doppler Tracking

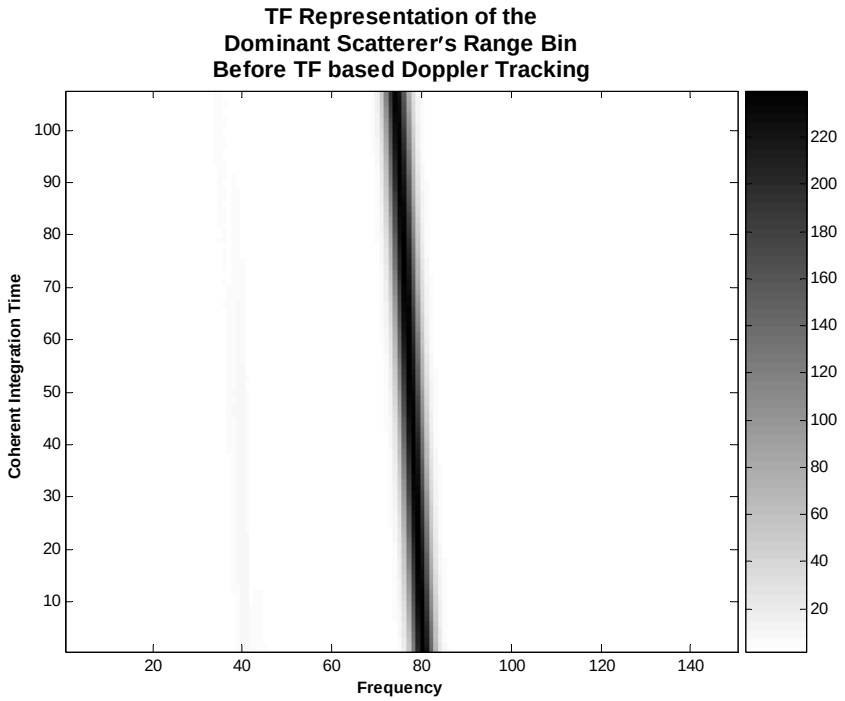

Figure 6.6 STFT analysis of the selected range-cell before TF-based Doppler Tracking

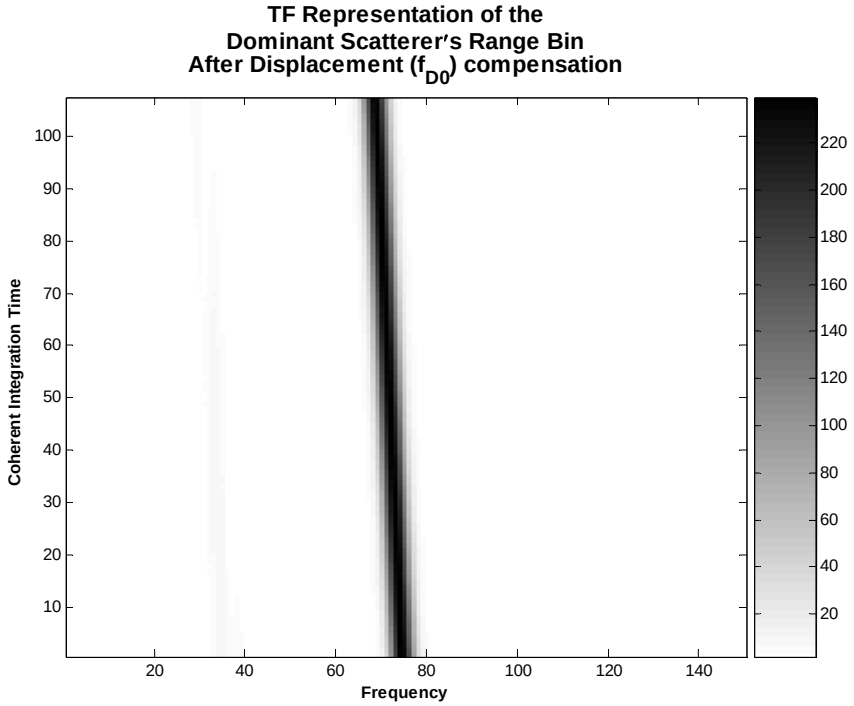

Figure 6.7 STFT analysis of the selected range-cell after displacement compensation

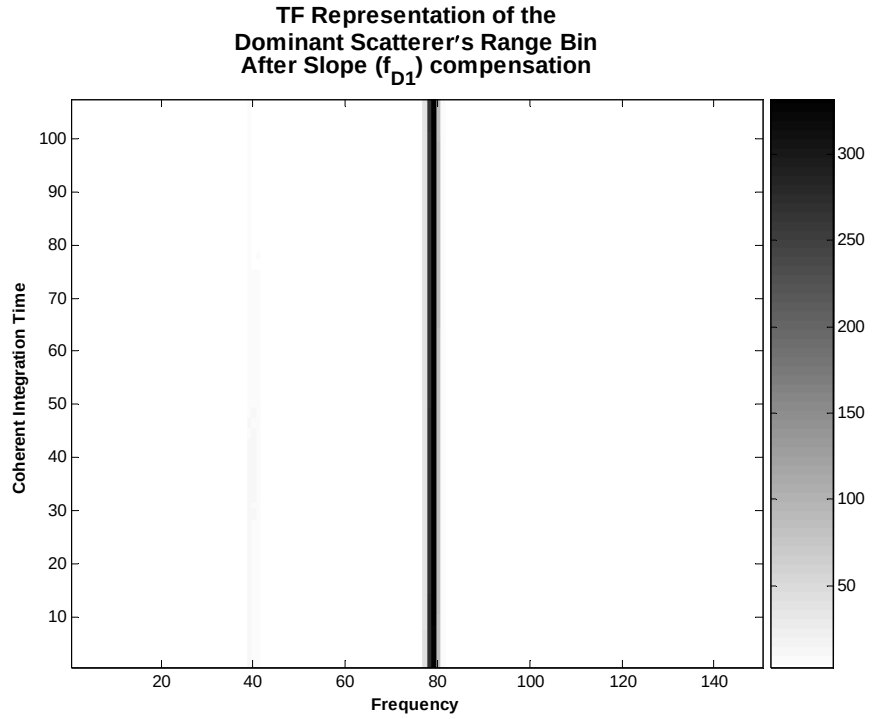

Figure 6.8 STFT analysis of the selected range-cell after slope compensation

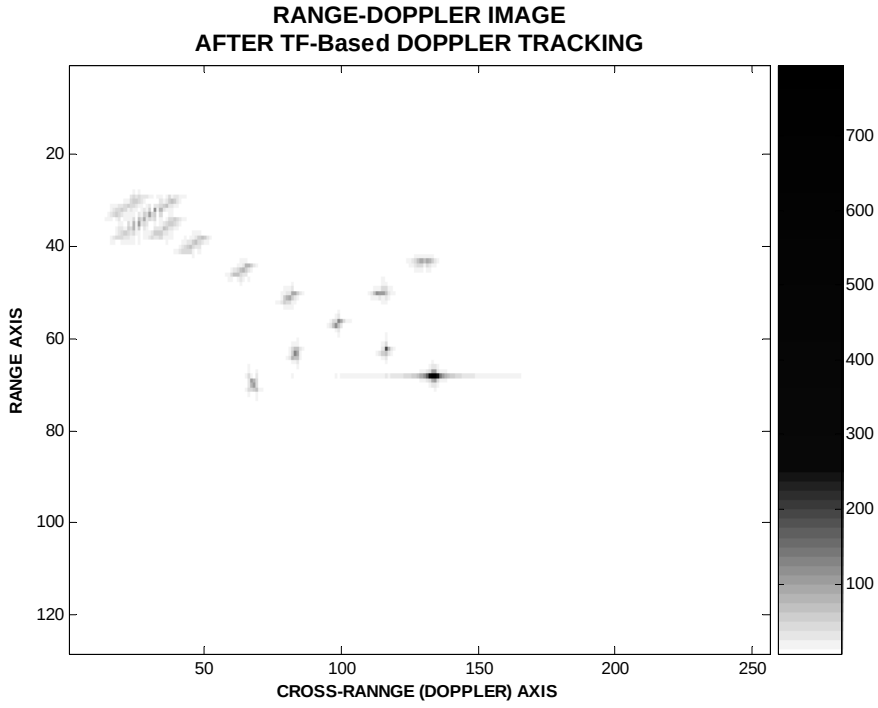

Figure 6.9 ISAR image of the target, after TF-based Doppler Tacking

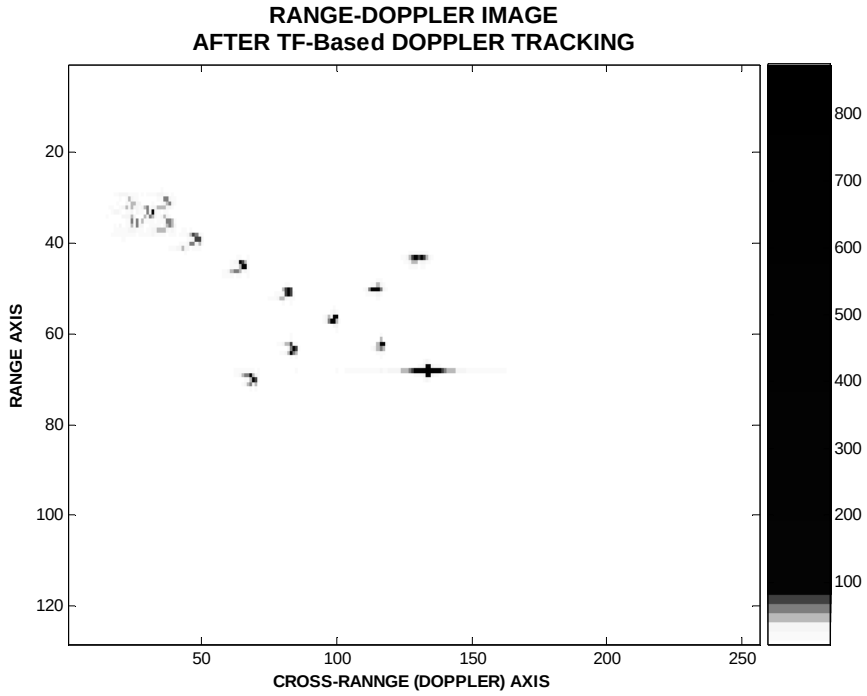

Figure 6.10 ISAR image of the target, after TF-based non-uniform rotational motion compensation

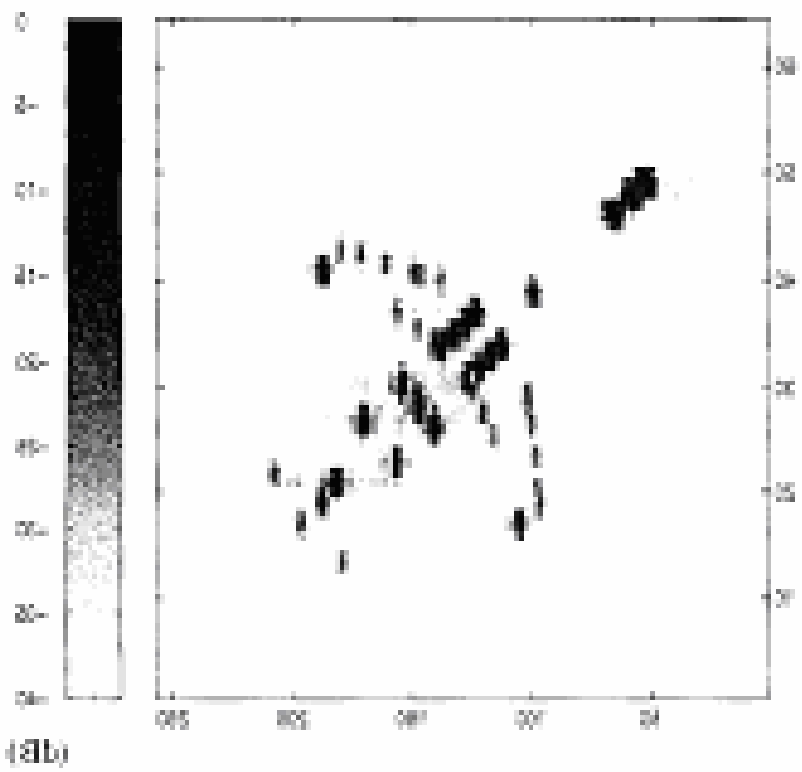

Figure 6.11 Illustration of the Simulation Model-2

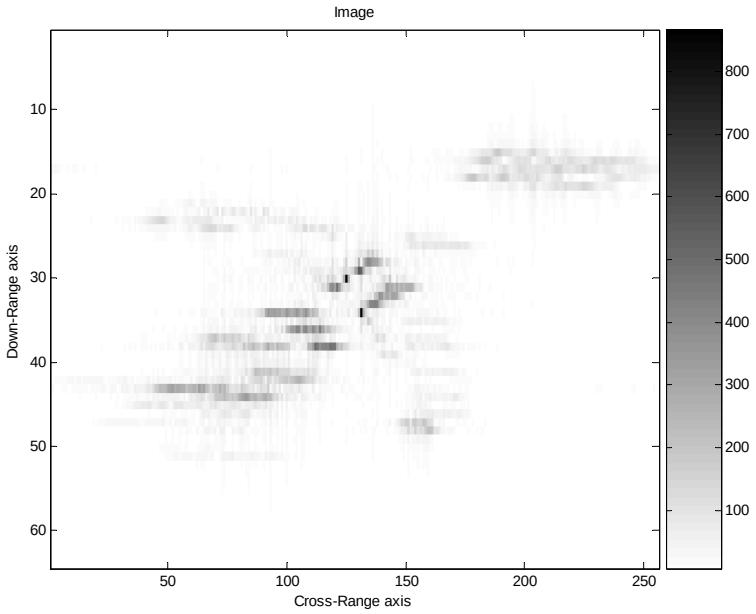

Figure 6.12 ISAR Image of the Simulation Model-2 after Range Tracking

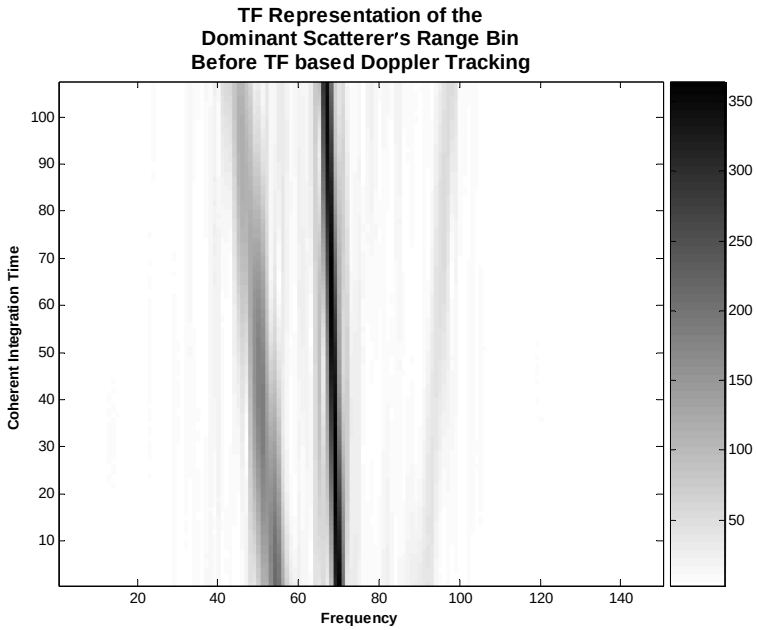

Figure 6.13 STFT analysis of the selected range-cell before TF-based Doppler Tracking

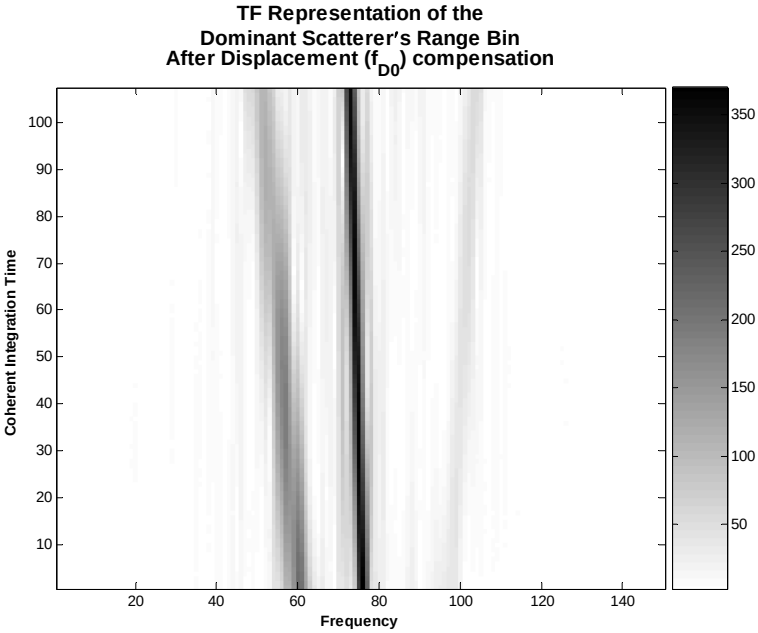

Figure 6.14 STFT analysis of the selected range-cell after displacement compensation

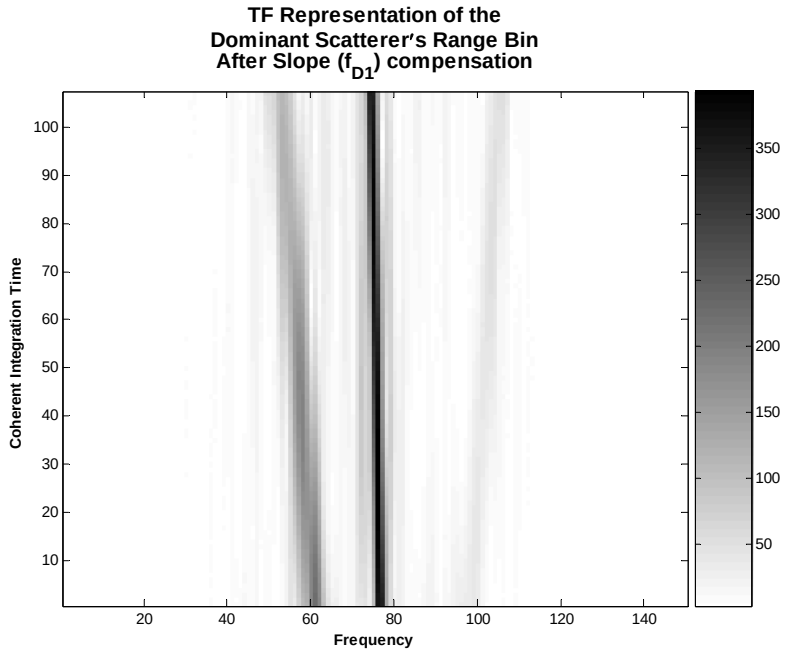

Figure 6.15 STFT analysis of the selected range-cell after slope compensation

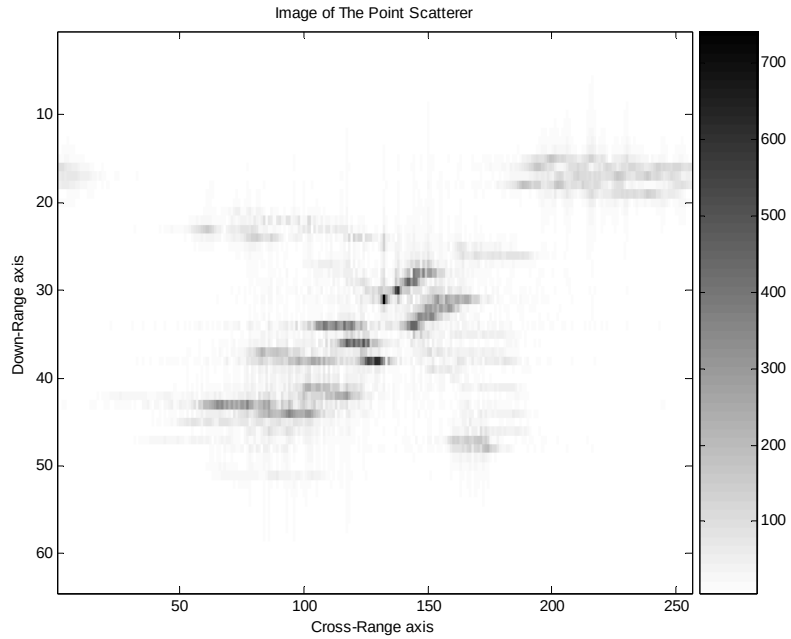

Figure 6.16 ISAR image of the target, after TF-based Doppler Tacking

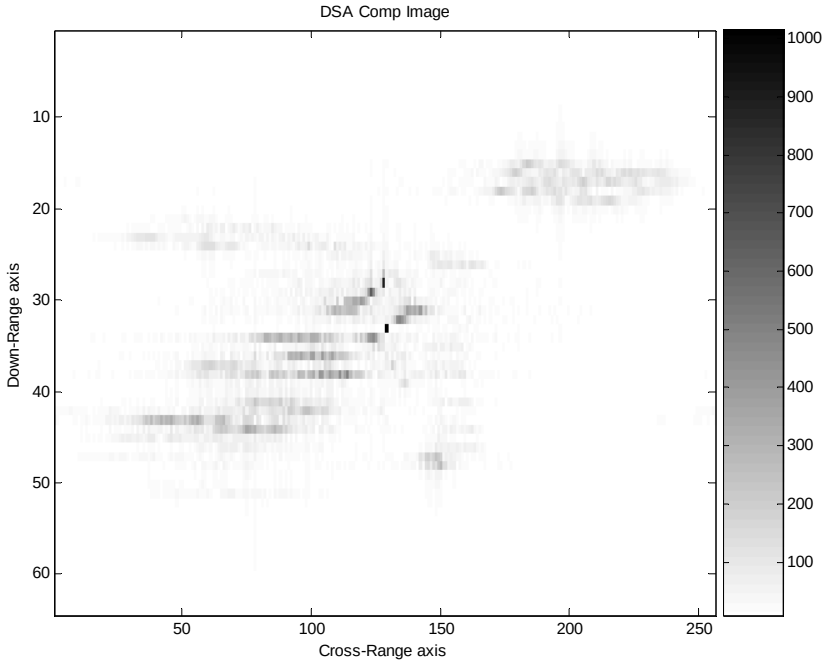

Figure 6.17 ISAR Image after DSA Doppler Tracking

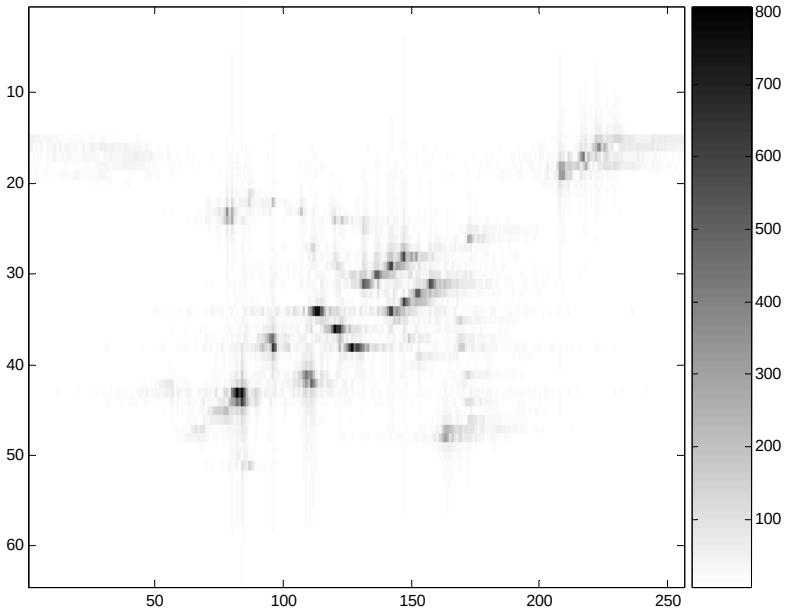

Figure 6.18 ISAR image of the target, after TF-based non-uniform rotational motion compensation

CHAPTER 7

CONCLUSIONS

ISAR systems are used to construct the two dimensional reflectivity images of the targets. Electromagnetic point of view, targets could be thought as the collection of scatterers. ISAR target imaging systems try to locate these scatterers onto the Range-Doppler plane. As a result, a scaled version of the shape of the target could be constructed on the Range-Doppler plane.

High resolution in range could be obtained by using high resolution radar waveforms. In all of the simulations in this thesis, step frequency type of radar waveforms and related echo responses were used.

First step of the ISAR image generation is the generation of range profiles (RPs). There are two methods to generate the RPs; real and synthetic RP generation. Real generation of RPs requires time domain sampling of the received target echo responses. Synthetic generation of RPs is a little bit complicated process. The main idea of the synthetic RP generation is producing the target's frequency domain responses and then using a basic IFFT process to generate RPs. Synthetic RP generation requires much more time then the real RP generation: In real RP generation process, a single pulse is enough to generate a single RP. But N discrete pulses are required in order to generate a Synthetic RP. As a result of this, synthetic RPs are much more sensitive to the motion of the targets. It means that, if the observed target exhibits some motion inside the RP generation time; this motion effects and spoils the quality of the synthetic RP N times more than it was in real RP.

Second step is the generation of the cross-range information. This is also called Synthetic Aperture Generation. Basic logic of the synthetic aperture generation is to extract the induced Doppler shifts from the complex RPs. Synthetic cross-range generation process requires some kind of signal processing along the range-cells.

First method, Conventional Range-Doppler Imaging uses basic Fourier Transformation process for this purpose. It is a fast process and does not require too much time.

The second method of ISAR imaging is the TF-based ISAR image generation. This method produces TF analysis of each range-cell, which results with a time-range-Doppler cube. Hence, ISAR images could be produced as the 2-D time slices of this cube. Since the Frequency content of the range-bin is examined and analyzed depending to the time; TF-based imaging seems like a natural way of motion compensation. Simulations prove that the TF-based image generation is could compensate limited degree of range-drifts of the target and cross-range smearing, which occurs when the target exhibits fast rotation about a fixed rotational axis. But the simulation examples are also proving that it impossible to use TF-based ISAR imaging for the translational motion compensation.

One of the most known methods of the TF transformation is STFT. STFT uses a sliding window on the time axis, in order to analysis the signal. This windowing procedure is the main disadvantage of it, since the cross-range resolution becomes limited and reduces with the length of the used time window. But there are some kinds of other high resolution JTFT method, which give full resolution in both time and frequency.

It is observed from the simulations that the motion of the target is the main reason of the image smearing in both range and cross range directions and has to be compensated.

The motion compensation concept is examined in details and some of the methods are explained and implemented by the way of simulations. Motion compensation could be divided in to two main parts;

1. Translational motion compensation,
2. Rotational motion compensation.

Translational motion compensation could be divided in to two parts;

1. Range Tracking
2. Doppler Tracking

In this thesis, range tracking part of the motion compensation is investigated with the cross-correlation method. Cross correlation method produces perfect results especially for the targets which include some dominant scatterers. In the absence of dominant scatterers, which is needed to dominate the cross-correlation process, it is observed that the cross-correlation process was failed not all, but some cases. But generally, it is observed that the cross-correlation method is sufficient to produce high degree of translational motion compensation even for the high degree of translational motions, like 350 m/sec.

It is also observed that the Range Tracking in translational motion compensation improves the scatterers' peak energy, by the way of collecting the scatterers' dispersed energy in to the specific pixels of the ISAR image. Actually, noise analyses are discarded in this thesis but it could be said that this kind of improvement also increases SNR.

Basically, cross-correlation of range profiles produces the information about profile-to-profile range shift information. Results of the cross-correlation process are used in the range-alignment after a smoothing process. This smoothing operation is done by the way of a low order polynomial fitting process. It is observed that, in the absence of the dominant scatterers, cross-correlation of RP's produces some ripples in the resultant range-delay information and this ripples let the smoothing process fail. There is no chance to avoid this effect. The only thing to do is expecting to catch a dominant scatterer in the target echo pulses.

The degree of the polynomial fitting process is another important criterion. First order polynomials give perfect results for constant translational velocities. But if the

targets effective translational velocity has some accelerating characteristics, as it was in the case of target's tangential motion to the LOS, it results with some curvatures on the RP trajectories. Hence, only second degree of polynomial fitting gives correct result and produces good range-alignment.

Second part of the translational motion compensation is Doppler Tracking. DSA (Dominant Scatterer Algorithm) method is used for the Doppler Tracking purpose. It is observed that the Doppler Tracking process could be successful only if the previous range tracking produces good range alignment. Any mistake in the range alignment process decreases the quality of the Doppler Tracking.

DSA algorithm, or more generally Doppler Tracking process, collects the scatterers' dispersed energy in the cross-range direction, hence produces SNR improvement.

DSA algorithm gives good results if the targets RP signature contains at least one range-cell, which is dominated by a strong scatterer. This domination is a relative definition. A separate but weak scatterer could be a dominant scatterer, or a strong but unstable source could not be.

It is observed that if a range cell is dominated by multiple scatterers and if that range cell is chosen as the phase synchronization source, there appears some spurious targets on the ISAR image.

It is observed that the TF-based Doppler tracking is also an applicable method of Doppler tracking. It is concluded that the main advantage of the TF-based Doppler tracking is that, the method works in the absence of a dominant scatterer in a particular range cell.

It is concluded that the second prominent point processing with the TF-based motion compensation is an effective way of non-uniform rotational motion compensation. It is also concluded that the 2^{nd} prominent point processing provides sufficient improvement on the ISAR images, only if the wide-angle imaging error (which occurs in the case of high rotation rates) is not serious.

TF-based ISAR imaging is suggested as the natural way of rotational motion compensation. But it has to be mentioned that there are some other special and dedicated methods such as Polar Reformatting for the rotational motion compensation.

The suggested future works are as follows:

Because of the nature of synthetic RP, some instantaneous jumps could be occurred on the RP track of the target, which are in the size of total range-cells. A special successful algorithm is used in this thesis, in order to compensate these kinds of jumps. But some other type of probable solutions, such as Kalman filtering, could also be investigated [23,24,25].

DSA and TF-based Doppler tracking algorithms are investigated in this thesis, for the Doppler tracking purpose. But there are some other kinds of techniques, such as RMSA (Recursive Multiple Scatterer Algorithm) [23], sub-aperture approach [8, 22] and PGA (Phase Gradient Autofocus) [18]. Those techniques could be examined in order to obtain some comparative results about the efficiency and the power of the algorithms.

REFERENCES

[1] S.A.Hovanessian, Introduction to Synthetic Array and Imaging Radars. Artech House, 1980.

[2] J.L.Walker, "Range-Doppler Imaging of Rotating Objects", IEEE Transactions on Aerospace and Electronic Systems, Vol. AES-16, No.1, January 1980.

[3] W.M.Brown, R.J.Fredricks, "Range-Doppler Imaging with Motion Through Resolution Cells", IEEE Transactions on Aerospace and Electronic Systems, vol. AES-5, No.1, January 1969

[4] D.R.Wehner, High-Resolution Radar. Artech House, 1995.

[5] E.L. Atılgan, Target Identification Using ISAR Imaging Techniques, MSc. Thesis, December 2005.

[6] A.Zyweck, Preprocessing Issues in High Resolution Radar Range Profiles, Ph.D. Thesis, March 1995.

[7] M.I.Skolnik, Introduction to radar systems, McGraw Hill, 1980.

[8] D.A.Ausherman, A. Kozma, J.L.Walker, "Developments in Radar Imaging", IEEE Transactions on Aerospace and Electronic Systems, Vol. AES-20, No.4, July 1984, pp. 363-400.

[9] C.C.Chen, H.C.Andrews, "Target-Motion-Induced Radar Imaging", IEEE Transactions on Aerospace and Electronic Systems, Vol. AES-16, No.1, January 1980, pp. 2-14.

[10] G.S.Gill, "Step Frequency Waveform Design and Processing for Detection of Moving Targets in Clutter", IEEE International Radar Conference, 8-11 May 1995, pp. 573-578.

[11] V.C.Chen, H.Ling, Time-Frequency Transforms For Radar Imaging And Signal Analysis, Artech House, 2002.

[12] V.C.Chen, http://airborne.nrl.navy.mil/~vchen/data/

[13] M.J.Prickett, C.C.Chen, "Principles of Inverse Synthetic Aperture Radar (ISAR) Imaging", IEEE EASCON '80 Record, 1980, pp. 340-344.

[14] B.Haywood, R.J.Evans, "Motion compensation for ISAR imaging", Proceedings of Australian Symposium on Signal Processing and Applications, 1989, pp. 112-117.

[15] W.G.Carrara, R.S.Goodman, R.M.Majevski, Spotlight Synthetic Aperture Radar: Signal Processing Algorithms, Artech House, 1995.

[16] H.J.Li, V.Chiou, "Aerospace target identification - comparison between the matching score approach and the neural network approach", Journal of Electromagnetic Waves and Applications, vol 7, no 6, pp 873-893, 1993.

[17] T. Itoh, H.Sueda, Y.Watanabe, "Motion Compensation for ISAR via Centroid Tracking", IEEE Transactions on Aerospace and Electronic Systems, Vol. AES-32, July 1996, pp 1191-1197.

[18] D.E.Wahl, "Phase Gradient Autofocus – A Robust for High Resolution SAR Phase Correction", IEEE Transactions on Aerospace and Electronic Systems, Vol. AES-30, July 1994, pp 827-835.

[19] S.Werness, W.Carrara, L.Joyce, D.Franczak "Moving Target Imaging Algorithm for SAR Data", IEEE Transactions on Aerospace and Electronic Systems, Vol. AES-26, January 1990, pp 57-67

[20] B.D. Steinberg, "Microwave Imaging of Aircraft", Proceedings of the IEEE, vol. 76, no. 12, December 1988

[21] Y.Wang, H.Ling, V.C.Chen, "ISAR Motion Compensation via Adaptive Joint Time-Frequency Technique", IEEE Transactions on Aerospace and Electronic Systems, Vol. AES-34, No. 2, April 1998

[22] T.M. Calloway, et al. “Subaperture Autofocus for Synthetic Aperture Radar”, IEEE Trans. Aerospace Electronic Systems, Vol. AES-30, April 1994, pp. 617-621.

[23] H.Wu, D.Grenier, G.Y.Delisle, D.G. Fang, “Translational Motion Compensation in ISAR Image Processing”, IEEE Transactions on Image Processing, Vol. 4, No. 11, November 1995, pp. 1561-1571.

[24] R.A. Singer, “Estimating optimal tracking filter performance for manned maneuvering targets”, IEEE Trans. Aerospace Electron. Syst., Vol. AES-6, July 1970, pp. 473-483.

[25] R.J.Fitzgerald, “Simple Tracking filters: steady-state filtering and smoothing performance”, IEEE Trans. Aerospace Electron. Syst., Vol. AES-16, No. 6, November 1980.

[26] S.Qian, D.Chen, Joint-Time Frequency Analysis: Methods and Applications, Prentice Hall PTR, 1996.